UNIVERSIDAD COMPLUTENSE DE MADRID

FACULTAD DE CIENCIAS FÍSICAS
Departamento de Física Aplicada III
(Electricidad y Electrónica)

TESIS DOCTORAL

Biophysical mechanisms and sources of extracellular potentials in the hippocampus
Mecanismos biofísicos y fuentes de los potenciales extracelulares en el hipocampo

MEMORIA PARA OPTAR AL GRADO DE DOCTOR

PRESENTADA POR

Antonio Fernández Ruiz

Directores

Miguel Sancho Ruiz
Sagrario Muñoz San Martín

Madrid, 2016

UNIVERSIDAD COMPLUTENSE DE MADRID

FACULTAD DE CIENCIAS FÍSICAS

DEPARTAMENTO DE FÍSICA APLICADA III

Biophysical mechanisms and sources of extracellular potentials in the hippocampus

Mecanismos biofísicos y fuentes de los potenciales extracelulares en el hipocampo

Memoria para optar al grado de Doctor presentada por:

Antonio Fernández Ruiz

Directores:

Miguel Sancho Ruiz

Sagrario Muñoz San Martín

Madrid, 2015

A ti que te fuiste antes de tiempo

pero nos dejaste lo mejor que tenemos:

tu recuerdo, tu fuerza y tu alegría.

Tu hijo.

Contents

Acknowledgements

Since I was an undergrad student in Sevilla starting to discover what Science was really about and specially after finishing my studies and initiating the research career, many people help me to arrive where I am now.

Starting from those early times in the School of Biology in the University of Sevilla and later in the Complutense of Madrid I have to remember a few of my professors who had the patient and energy to show me their research, let me be around and answer my thousand questions: Josefina Cano, Ángel Pastor, Sara Morcuende, Esperanza Rodriguez, Carmen Rúa and many others. Even if I was convinced of trying to become a scientist I was not yet sure that I will choose the Neurosciences. I learned to enjoy many different fields of Biology: Evolution, Genetics, Zoology thanks especially to amazing readings of great scientists (SJ Gould, Jacob and Monod, Darwin and so many others) and some enthusiastic professors. Sadly not all my professors or class mates were equally enthusiastic about science and research; however with some of them who truly were I shared many interesting and stimulating talks. Among those I remember specially some: Alvarito, Gonzalo, Miguel, Curro, Alberto, David.

After finishing my Biology studies my interest towards the physical sciences had grown more and more, plus I felt the necessity of complement my formation with some basic formal knowledge about Physics and Maths. I would probably never develop such interest if it were not because the inspiring readings of some of the brightest minds of the past century: Heisenberg, Schrodinger, Einstein, etc. I really enjoyed those readings as well as learning about Quantum Mechanics, Particle Physics and Logic. However, I realized that was not the field where I could work my best, so despite those temptations I finally found my place in the Neuroscience field.

During my Physics Master I met great and helpful professors (Miguel Sancho, Sagrario Muñoz, Tatiana Alieva, Fernando Sols and others) and mates from the Schools of Physics and Mathematics (Pilar, Pablo, Ricardo, David, Jaime, Jesus). And I also met a very special person.

Although I had some previous research experience I really started doing science in the Cajal Institute. The years I spent there constitute in general a good experience. In the laboratory

of Óscar I learned many things: to love the Electrophysiology, to perform experiments, to plan and carry out my own research project, etc. I was more than lucky with some of my lab mates, Azahara and Gonzalo, with whom I shared the enthusiasm of discovery and the long hours that it usually takes. The time I share with them both inside and outside the lab was the best part of all what I spent in Madrid. I was also very lucky with some of the other students of the Institute for so many good moments and conversations, specially Maria, Jorge and Edu; and some of the researchers, Liset, Gonzalo. However, during those years I also got to know the worst face of academic life and the conflicts that arise when people are more driven for other motivations than the pursue of knowledge and the enjoyment of Science both as a career and as a lifestyle.

After my stage in the Cajal I went to the laboratory of Gyuri Buzsáki in the NYU. That was the best of the lucks and a step forward into the real international academic world, beyond the idiosyncratic borders of Spanish scientific community. I am very grateful to the generosity, energy and enthusiasm of Gyuri, who embraced me and showed me how far I could go once I found the proper path. I am also grateful to many people who generously shared their data or codes with me and others that help me with my experiments: Erik, Tony, Kenji, Dion, Yuta, Gabrielle and others. I have to give special thanks to Tony Berényi for sharing his great data and advices and help me to do crazy silicon probe implantations both in the NYU and after that in his laboratory in the University of Szeged. Also to my hungarian mates Misi, Ancsa and Gábor.

Finally I came back to accomplish my PhD at the Complutense. I have the biggest of the gratitude to Miguel and Sagrario who despite the complicate situation I brought to them had no hesitation to embrace me and help with all the possible things; personal, scientific and administrative. Without that it would have not been possible the present thesis.

Although the funding climate and support for research was far from ideal in Spain in the last years, I was lucky of having during my university and research stages the economic support of different institutions: Universidad de Sevilla, the Xlab and Georg-August Universität of Gőttingen, Universidad Complutense de Madrid, Ministerios de Educación y de Ciencia, CSIC y JAE, European Molecular Biology Organization (EMBO), Fundación La Caixa, Sociedad Española de Neurociencia (SENC), Federation of European Neuroscience (FENS) .

The PhD work is many times rewarding and enjoyable, but not always. In that times I found one my greatest shelters and sources of renew energy in the books. The words on some people with very similar concerns, worries or hopes than mines often help me during this time: Borges, Hesse, Dostoyevski, Wittgenstein, Cernuda, Machado, Asimov and many many others.

Por último, a llegar hasta aquí me han ayudado mucho otras personas de fuera del ámbito académico, especialmente mi familia. A Azahara le tengo que agradecer doblemente. En lo personal, por estar siempre a mi lado de una punta a otra del mundo con su constante amor, comprensión y, algo nada fácil, paciencia. Y en lo profesional por ayudarme con los experimentos y análisis sin importar que fueran vacaciones o de madrugada. A mi hermano por no perder la confianza en mí ni desesperarse a pesar de mi difícil carácter olvidadizo y ensimismado, y por su constante apoyo. A mi padre por su inagotable interés acerca de todo lo que yo hago y por enseñarme el valor del esfuerzo, la constancia y la superación personal, desde niño hasta ahora. Y a mi madre por su infinito amor, alegría y optimismo. Por enseñarme a enfrentar del mejor modo cualquier adversidad, a no perder la fe en mí mismo ni desanimarme nunca y a que el futuro está siempre lleno de oportunidades para quien quiere buscarlas. Si no fuera por ellos tampoco estaría hoy aquí.

Abstract

In last decades the study of the Nervous System function has moved gradually from the cellular and molecular levels to a more systemic perspective. Due to the recent developments in technologies to record and manipulate large populations of cells in behaving animals, the available volume of data has rapidly increased. Although this boost in the amount of data regarding the function of neural circuits in action opens new and exciting roads to understanding information processing in the brain, it also poses new challenges to their analysis and interpretation. One variable that can capture the activity of multiple neural populations in different brain areas with high spatial and temporal resolution is the local field potential (LFP). Despite the potential usefulness of LFPs to read out the computations performed by brain circuits during behavior, its study has been hampered by the difficulties in extracting meaningful information from it. In the present thesis, we aim to study the biophysical basis of the LFP as a way to reach a deeper understanding of it in terms of its underlying physiological mechanisms.

We focused on the rodent hippocampus due to the important role that it plays in many cognitive functions (such as memory, learning or spatial navigation) and the advantages of its simplified layered structure for the study of LFPs. Taking advantage of high-density silicone probe recordings in behaving rats, we were able to map the spatiotemporal distribution of LFPs along the dorsoventral and transversal axes of the hippocampus. We implemented a novel method consisting in the combination of Independent Component Analysis (ICA) and Current Source Density (CSD) analysis to separate and identify the synaptic sources of hippocampal LFPs. In addition we built a tridimensional model of the rat dorsal hippocampus where the spatiotemporal characteristics of those sources were implemented and LFPs were simulated by means of Finite Elements Method. Those simulations reproduced the common hippocampal LFP patterns and laminar characteristics, thus enabling us to reach a better understanding of the generation of LFPs in the hippocampus and verifying the accuracy of the ICA+CSD decomposition of experimental data. The simulations also allowed us to test the influence of structural and dynamical factors such as tissue geometry, synaptic arrangement and input synchrony in the shape and propagation of LFPs.

To prove the relevance of the knowledge gained about the biophysical basis of LFPs in the hippocampus we addressed the issue of theta and gamma dynamics in the hippocampal-entorhinal circuit during different behavioral states. We found three sources of gamma oscillations in the CA1 region with different laminar distribution, spectral characteristics and theta-phase preference. Slow gamma (30-60 Hz), elicited by the CA3 input to the CA1 pyramidal cells, peak on the descending theta phase; while mid-frequency gamma (60-120 Hz), brought about by entorhinal layer 3 input to CA1, dominate on the peak of the theta cycle. A third source of very fast oscillations (100-180 Hz) peaked on the theta through and was of local origin. Those theta-coupled gamma oscillations were present in both exploration and REM sleep albeit with different strength. We showed that during different behavioral states and stages of a memory task, CA3 and entorhinal gamma inputs could compete or cooperate to modulate CA1 output and interregional communication.

The results presented in this thesis constitute an advance in our understanding and interpretation of LFPs and brain oscillations. They highlight the importance of the employment of adequate experimental and analytical methods to interrogate the activity of brain circuits and point to the LFP as a useful although complex variable in this purpose.

Resumen

En las últimas décadas el estudio de la función del Sistema Nervioso ha ido evolucionando gradualmente desde los niveles celular y molecular hacia una perspectiva más sistémica. Debido a los recientes desarrollos en técnicas para registrar y manipular la actividad de grandes poblaciones neuronales en animales durante el comportamiento, el volumen de data disponible se ha incrementado rápidamente. Aunque este incremento en la cantidad de datos funcionales sobre la actividad de los circuitos neuronales abre nuevas y excitantes posibilidades para entender el procesamiento de información en el cerebro, también plantea nuevos desafíos para su análisis e interpretación. Una variable que permite capturar la actividad de múltiples poblaciones neuronales en diferentes aéreas cerebrales con gran resolución tanto espacial como temporal es el potencial de campo local (o LFP por sus siglas en inglés). A pesar de la potencial utilidad del LFP para desentrañar las computaciones realizadas por los circuitos neuronales durante el comportamiento, su empleo se ha visto limitado por las dificultades que se plantean al intentar interpretarlos. En esta tesis estudiamos las bases biofísicas de los LFPs como un camino para alcanzar un mejor entendimiento de esta señal en términos de sus mecanismos fisiológicos subyacentes.

En este trabajo nos centramos en el hipocampo de los roedores debido a su importante papel en numerosas funciones cognitivas (como la memoria, el aprendizaje o la navegación espacial) y las ventajas que supone su estructura laminar simplificada para el estudio de los LFPs. Aprovechando la ventaja de los registros de gran densidad con multielectrodos de silicio en ratas durante el comportamiento hemos mapeado la distribución espaciotemporal de los LFPs a lo largo de los ejes dorsoventral y transversal en el hipocampo. Hemos implementado un novedoso método que combina el empleo del Análisis de Componentes Independientes (ICA por sus siglas en inglés) y el análisis de fuentes de corriente (CSD) para separar e identificar las fuentes sinápticas de los LFPs en el hipocampo. Así mismo hemos construidos un modelo tridimensional del hipocampo dorsal de la rata, implementando en él la distribución espaciotemporal de dichas fuentes y simulado los LFPs del hipocampo empleando el Método de Elementos Finitos (FEM). Mediante estas simulaciones reproducimos los patrones

electrofisiológicos más comunes observados en el hipocampo así como sus características laminares. Ello nos ha permitido alcanzar un mejor entendimiento de la generación de potenciales extracelulares en el hipocampo así como verificar la validez de la descomposición de los LFPs registrados experimentalmente, llevada a cabo mediante la combinación de ICA y CSD análisis. Las simulaciones llevadas a cabo con el modelo también nos han permitido estudiar la influencia de factores tales como la geometría del tejido, la distribución de los contactos sinápticos o la sincronización de los inputs en la generación y propagación de los LFPs.

Para probar la relevancia de los conocimientos adquirido a cerca de las bases biofísicas de los LFPs en el hipocampo, los hemos aplicado al estudio de las oscilaciones theta y gamma en el circuito hipocampo- corteza entorhinal durante distintos estados conductuales. Hemos encontrado tres fuentes de oscilaciones gamma en la región de CA1, cada una con diferente distribución laminar, características espectrales y preferencia por una determinada fase del ritmo theta. El gamma lento (30-60 Hz), producido por el input de CA3 a CA1, alcanza su máximo en la fase descendente del ciclo theta, mientras que el gamma de media frecuencia (60-120 Hz), producido por el input de las células de la capa 3 de la corteza entorhinal a CA1, es dominante en el pico del ciclo theta. Una tercera fuente de oscilaciones de alta frecuencia (100-180 Hz) alcanza su máxima potencia en el valle del ciclo theta y es producida por la actividad de los circuitos locales de CA1. Estas oscilaciones gamma moduladas por el ritmo theta estuvieron presentes tanto durante la exploración como durante el sueño REM, aunque con diferente potencia. Mostramos que durante diferentes estados conductuales y etapas de una tarea de memoria los inputs de CA3 y la corteza entorhinal pueden competir o cooperar para modular la salida de CA1 y su comunicación con otras regiones.

Los resultados presentados en esta tesis constituyen un avance en nuestro entendimiento e interpretación de los LFPs y oscilaciones neuronales. Subrayan la importancia del empleo de métodos adecuados tanto experimentales como de análisis para el estudio de la actividad de los circuitos neuronales. Así mismo demuestran la utilidad de los LFPs para extraer información relevante a este respecto a pesar de su gran complejidad.

1. Introduction

1.1. Genesis and study of the macroscopic electrical activity in the brain

The brain is a complex system, probably the most complex of all. Despite that it is formed by relatively simple (only in comparison) elements: neurons and other cell types. Its complexity mainly arises from the myriad of intricate ways those elements are interconnected forming networks or neural circuits. The dominant paradigm in Systems Neuroscience in last decades has been that is the distributed activity of brain circuits the physiological mechanism underlying cognitive functions (Bullmore and Sporns, 2009; Tononi et al., 1998; Varela et al., 2001; Buzsaki and Mizuseki, 2014). There is also a large degree of functional modularity in the brain, that is discrete brain regions dedicate to particular functions, in particular in early sensory systems. However, most cognitive functions relay on the activity of "higher" cortical associative areas that integrate information from different sensory modalities together with emotional and motivational content. In addition to the integration of external inputs to conform unified percepts, another complementary function of these associative brain areas is to support the interaction of external inputs with self-generated internal ones and stored memory engrams (Lisman and Idiart, 1995; Buzsáki and Moser, 2014).

To perform those functions, brain circuits need to be able to integrate distributed local processes or computations into globally organized states and, in turn, route the flow of highly processed information to downstream structures both in the brain and effector organs (muscles, etc.). For this wide integration and segregation of information brain oscillations, or "rhythms", are thought to perform an essential role (Varela et al., 2001; Buzsáki, 2006; Buzsáki et al 2013; Lisman and Jensen, 2013).

Brain oscillations are present across all animal phyla, from invertebrates to birds, reptiles and mammals (Mader and Bucher, 2007; Buzsáki et al., 2013). Although their mechanisms vary largely, a common feature is the requirement of synchronized activity in specific circuits of interconnected excitatory and inhibitory neurons that generate rhythmic postsynaptic potentials (PSPs). Those PSPs synchronized over large populations of cells are the main source of

macroscopic oscillations. These rhythmic synaptic inputs produce in the target neural population alternate windows of enhanced and reduced excitability. This mechanism plays a double function, on one hand favors the integration of incoming inputs and their plasticity in discrete time frames; on the other, it segregates the output of the neurons (the generation of synchronized action potentials) into short burst and sequences (Wilson and McNaugthon, 1994; Buzsáki, 2010).

Neural oscillations span several orders of magnitude in frequency, from the very slow (< 1Hz) to the very fast (200-500 Hz; Figure 1.1A). Among the most studied of them are the slow-wave-sleep delta waves (0.5-1.5 Hz), the hippocampal theta rhythm (5-10 Hz), the cortical gamma rhythms (40-90 Hz) and hippocampal ripples (140-220 Hz). Slow oscillations are coherent across wide regions even spanning different structures, generating synchronized membrane fluctuations in widespread neuronal networks. On the other hand, faster oscillations are usually associated with local computations performed by small numbers of cells and thus are only synchronous in a highly restricted volume.

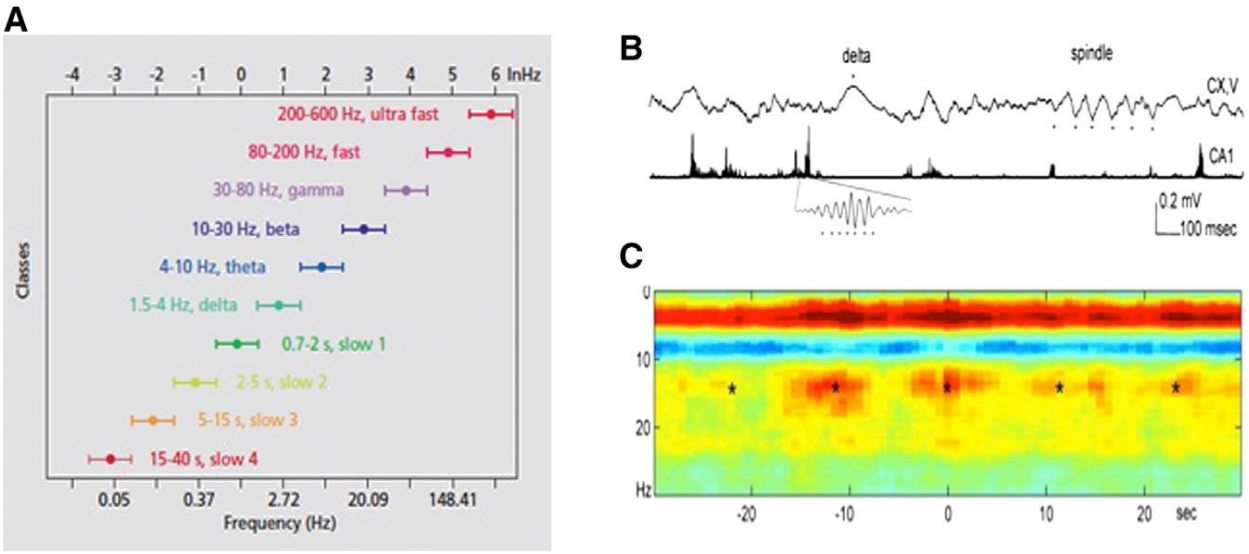

Figure 1.1: **A:** Main classes of brain oscillations spanning several orders of magnitude. **B:** LFP trace from rat cortical layer 5 during sleep showing different characteristic oscillations: delta waves and spindles. Below, filtered and rectified LFP from hippocampus CA1 pyramidal layer displaying ripples as large amplitude bursts. **C:** Ripple-triggered power spectrogram of cortical LFP showing modulation by spindles (revealed by power increase around 15 Hz). Both events are also modulated by the slow oscillation (0-3 Hz). From Buzsáki et al., 2013.

Oscillations of different frequency very often interact with each other both locally and across structures. This interaction follows typically a hierarchical fashion, thus the phase of the slower oscillations modulates the amplitude and occurrence of the faster ones (Bragin et al., 1995; Chrobak and Buzsaki, 1998; Schroeder and Lakatos, 2009; Canolty et al., 2006; Fell and Axmacher, 2011. Figure 1.1B,C). Cross-frequency coupling has been shown to correlate with memory performance in both humans and animals (Canolty et al., 2006; Tort et al., 2009; Axmacher et al 2010; Schomburg, Fernández-Ruiz et al., 2014). Cross-frequency coupling in cortical circuits has been proposed as a mechanism to integrate local computations across modules in a broader time scale, thus allowing the efficient integration of different streams of information necessary for most cognitive processes (Lisman and Jensen, 2013).

The interest in studying brain oscillations arises also from the fact that particular rhythms are altered during different pathological states, including but not limited to epilepsy, Alzheimer's disease, schizophrenia and depression (Ulhaas and Singer, 2006; Pittman-Polletta et al., 2015). Thus its study may lead to a better understanding of the mechanisms of those diseases or even provide early markers to their detection.

To understand the neurophysiological basis of cognitive processes there are many different approximations. The most traditional approach has been the recording of individual neurons activity to correlate its firing dynamics with specific behaviors. With modern recording techniques it is possible to simultaneously record extracellularly a few hundreds of neurons or intracellularly identified single cells in behaving animals. In the other extreme of the scale we find functional imaging techniques (fMRI, MEG, PET, etc.) that can monitor whole brain activity and identify regions that are activated during a particular task. These techniques have also the advantage that are non invasive so can be used in humans. Despite the advances in recent decades in both extremes, subcellular and global scales, there is still an important gap in the middle, that is how individual cells coordinate in neural circuits to orchestrate different cognitive functions. This has prevented us to reach a comprehensive explanation of behavior and cognitions in terms of its underlying physiological mechanisms. The study of neuronal circuit dynamics tries to bridge this gap.

One technique that allows the recording of neural activity of intermingled neural populations in different brain areas with high spatial and temporal resolution is the recording of

the intracranial electroencephalogram (EEG). The EEG is produced by the superposition in the extracellular medium of transmembrane currents in adjacent neurons. These currents are mainly elicited by the plethora of synaptic inputs generating PSPs, but there are also other non-synaptic sources of the EEG (see Buzsáki et al, 2012). The transmembrane currents elicit an electric potential that varies dynamically in time and space, giving rise to the recorded EEG (Figure 1.2). Thus, the EEG contains all the summed activity of the multiple synaptic inputs and local activity in the region where the extracellular electrode is located. For historical reasons and despite the physical inaccuracy of the term, the intracranially recorded EEG is always referred in the literature as local field potential (LFP).

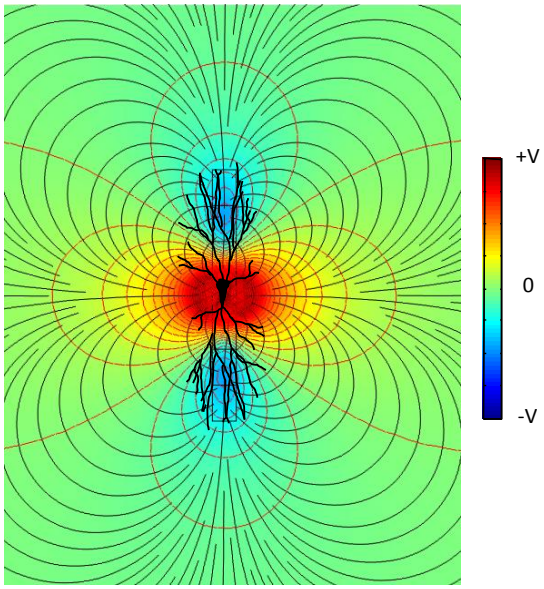

Figure 1.2: A simplified simulation of a single neuron receiving an inhibitory somatic input. Active outward currents in the soma are compensated by return inward current in the apical and basal dendrites resulting in a negative-positive-negative extracellular potential profile. Colors indicate extracellular voltage, red lines isopotential surfaces and black current lines.

Biophysical principles underlying LFP generation are long known (Lorente de Nó 1947; Buzsáki et al., 2012; Einevoll et al., 2013). However, there are still many theoretical and technical problems that limit the usefulness of LFPs to understand brain function. A long standing biophysical problem that has maintained the field at sluggish pace for decades is the difficulty to identify the synaptic sources of LFPs so to correlate activity of known neuronal populations to ongoing behavior. As the LFP in any point in the brain is produced by the activity

of intermingled cellular populations with overlapped synaptic territories, to identify the cellular origin of particular LFP patterns, the so called *inverse problem*, is a complex task. This problem can be also reformulated as follows; once given an experimental macroscopic signal the amplitude of which varies at different sites (i.e. the LFP), how can the location and extension of the generating source be determined? Multiple combinations of independent sources (transmembrane currents in discrete dendritic domains of a population of synchronously active neurons) may give rise to a recorded signal with the same spatial pattern. There is no unique solution and in most cases, it is difficult or impossible to confirm the potential solutions experimentally.

A common feature of electric fields in the brain is that they vary spatially in a complex manner, on account of the shifting activation of neuron generators with irregular morphology and distribution. Neurons with dominant axial geometry act as strong current dipoles (Lorente de Nó 1947; Buzsáki et al., 2012; Einevoll et al., 2013) and as such are the main contributors to field potentials. A common afferent input to one or another subcellular domain of the neuron population will give rise to different extracellular potential distributions. This fact underlies the characteristic laminar profile of LFPs in layered structures. The problem arises when several inputs are co-activated, as is usually the case. In such circumstances, the electric currents mix unevenly at different sites, and field potential distributions become complex and variable. Thus, only high-density recordings simultaneously performed at several positions can correctly map for spatial variations of LFPs. Multisite linear recordings are well-suited to a method that has been employed to find the current generators underlying field potentials, known as current source density (CSD) analysis (Freeman and Nicholson, 1975). This approach has been very useful to determine the contributing cells and the location of synaptic membranes activated by afferent stimuli in laminar structures, such as the hippocampus or neocortex (Leung, 1991; Schroeder et al., 1998; Bragin et al., 1995). However, while interpreting CSD maps is simple for voltage profiles elicited by stimulating only one afferent pathway, their application to ongoing LFPs renders complex spatial maps of intermingled inward and outward currents, and in general it is not feasible to identify the multiple synaptic generators from them (Figure 1.3).

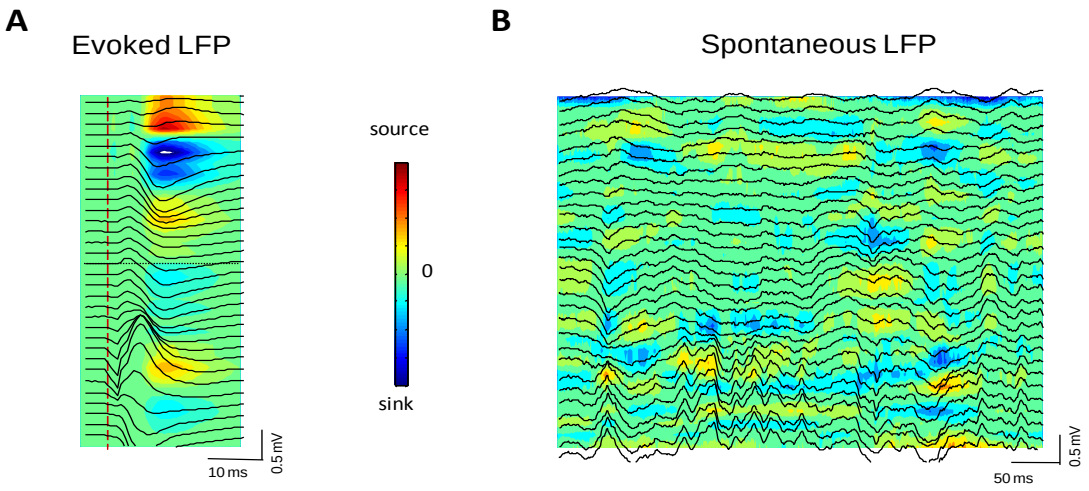

Figure 1.3: **A:** LFP profile and CSD map of an evoked potential in the hippocampus resulting from the stimulation of the CA3.In the upper part (CA1) a strong sink (in blue) results from the depolarization of CA1 pyramidal cell dendrites and is compensated by two sources elicited by passive return currents. The recurrent collaterals of CA3 axons also produce a local current dipole. **B:** During spontaneous activity in the hippocampus of an awake rat, multiple synaptic inputs arrive simultaneously to the CA1 and CA3 regions making it very complex to interpret CSD distributions.

An important additional source of complexity and confounding factors when analyzing or modeling LFPs or other macroscopic variables of neuronal activity are the electric properties of brain tissue. For the sake of simplicity it is commonly assumed that the brain tissue is homogeneous, isotropic and has ohmic (linear) properties. The contribution to the recorded LFP from a particular neuronal membrane domain (either in a single cell or in a population of synchronously active neurons) is usually estimated as follows

$$\phi(r_e,t) = \frac{1}{4\pi\sigma}\sum_{n=1}^{N}\frac{I_n(t)}{|r_e - r_n|} \qquad (1.1)$$

The above equation denotes that the contribution of the transmembrane current I_n in a membrane domain n to the LFP recorded at $\boldsymbol{r}_e$ is inversely proportional to the distance between the electrode and the source and to the extracellular conductivity of the tissue σ. The LFP thus would be the result of the linear summation of all the transmembrane currents weighted by their distance to the recording electrode (Figure 1.4). Here, we are assuming a quasistatic approximation of Maxwell equations in which the electric and magnetic fields are decoupled and there are not inductive

effects. This seems reasonable giving the characteristic low frequency of brain activity and in particular of that contributing to the generation of LFPs (mostly below 300 Hz; Plonsey and Heppner, 1967; Nunez and Srinivasan, 2006). The above equation also implies that the medium where neuronal currents propagate is an infinite, homogeneous and isotropic conducting volume. Although in many cases those assumptions may be reasonable, they are fundamentally inadequate. On a large scale, the brain is obviously not homogeneous, for example, the presence of the liquid filled ventricles may greatly distort the propagation of electric fields. At a microscopic level, the tissue can be considered mainly homogeneous, but even so it has been showed that is not completely isotropic due to the presence of dense cellular layers or myelinated axonal bundles (Nunez and Srinivasan, 2006). A third assumption made in the above equation is that the conductivity is purely ohmic, that is it is no frequency-dependent or has capacitive effects. About this last point, there has been a lot of debate in the last years and there is not yet a definite answer (Bedard and Destexhe, 2011; Logothetis et al., 2007; Einevoll et al., 2013). It can be said that there are probably some frequency dependent properties of brain tissue but those are not very influential in most cases and applications.

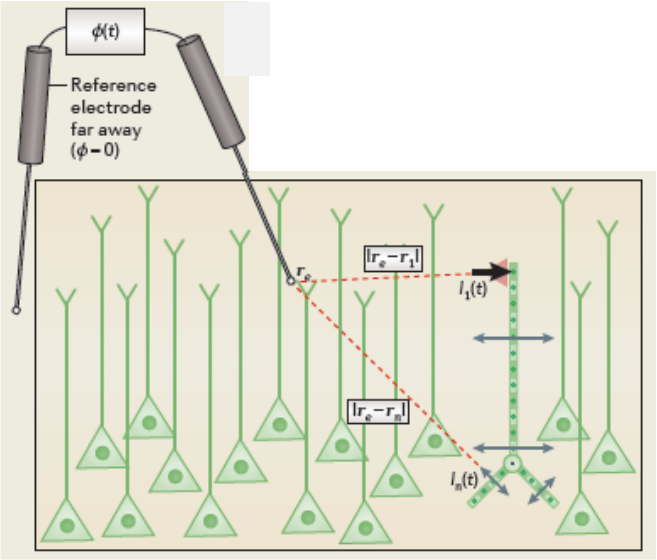

Figure 1.4: Simplified schematic showing the calculation of the LFP produced by a single pyramidal neuron receiving an apical input. Synaptic input elicit inward transmembrane currents locally ($I_1(t)$, black arrow) that are followed by return outward currents all along the membrane of the cell ($I_n(t)$, grey arrows). Transmembrane currents in each of the cell compartments elicit an electric potential at the tip of the recording electrode (r_e) respect to a distant reference. The summation of all the transmembrane currents in each compartment n weighted by their distance to the electrode $|\boldsymbol{r}_e - \boldsymbol{r}_n|$ and the conductivity of the tissue is the LFP produced by that neuron.

1.2 Anatomy and physiology of the hippocampal formation

1.2.1 Anatomical and functional organization of the hippocampal formation

Over decades, the mammalian hippocampal formation (HF) (Figure 1.5A) has attracted the attention of neuroscience researchers because its easily recognizable anatomical features (Cajal, 1911; Lorente de Nó, 1934), its prominent electrophysiological activity patterns (Whishaw and Vanderwolf, 1973; Buzsáki et al., 1983) and its functional implication in learning and memory processes. For a comprehensive reading of hippocampal formation anatomy and function there are many excellent reviews (Witter, 1993; Bland and Oddie, 2001; Vinogradova, 2001; Eichenbaum, 2004) and books (Buzsáki, 2006; Andersen et al., 2007). Here we provide a brief summary of the most relevant aspects for the present thesis.

The term hippocampal formation (HP) is used to designate several brain structures derived from the medial palium and strongly anatomically and functionally related: the hippocampus proper or *cornus ammonis*, the Dentate Gyrus (DG) and the subiculum (Burwell et al., 1995).

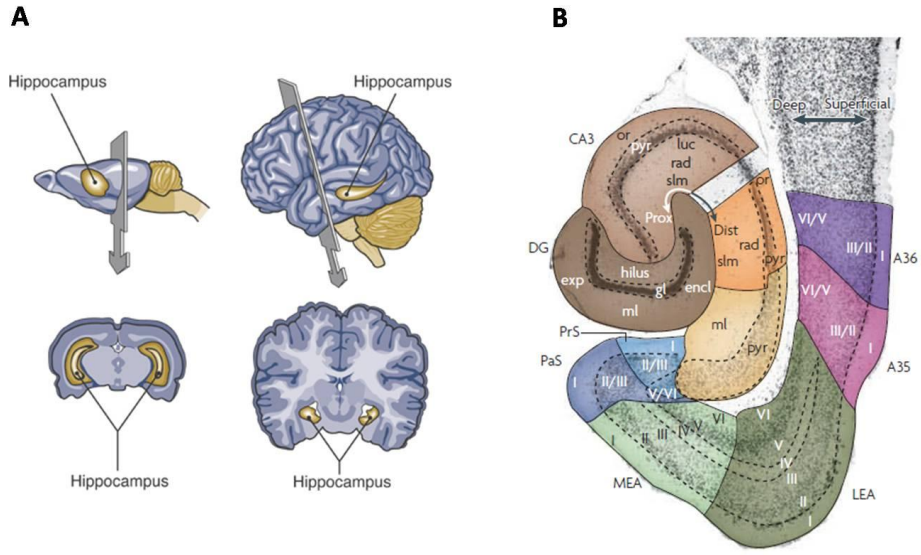

Figure 1.5: **A:** Comparison of rat and human hippocampi. Note the much larger size in comparison with the rest of the brain rodent hippocampus. B: Subregions of the rat hippocampal formation in a horizontal section. From Hiller-Sturmhőfel and Swartzwelder and Van Strien et al., 2009.

In the hippocampus, cellular bodies are densely packed forming one layer. Pyramidal cells form the *cornus ammonis*, divided by Lorente de Nó in 4 sub-regions CA1-4. In the DG, granular cells form the U-shaped granular layer (Cajal, 1911; Lorente de Nó, 1934). The subiculum has several cellular layers and is divided in three main regions: presubiculum, parasubiculum and postsubiculum. The HF is strongly interconnected with the adjacent entorhinal cortex (EC), which constitutes the principal source of afferences to it. It possesses a more complex cytoarchitectonic structure than the hippocampus with six layers. It is divided in two functionally and anatomically distinct regions, the medial (MEC) and the lateral portions (LEC; Figure 1.5B).

Classically the hippocampal formation has been described as a feedforward circuit of excitatory synapses (Figure 1.6A). According to this model, neurons in the layer II (L2) of the EC project to the DG through the perforant pathway. L2 axons also innervate CA3 pyramidal cells. DG granular cells send their axons (the so called mossy fibers) to CA3. CA3 pyramidal cells axons divide to make recurrent connections within CA3 and also innervate a large extent of the CA1 region (the Schaffer pathway). CA1 pyramidal cells also receive direct connections from EC L3 cells through the temporo-ammonic pathway and in turn project to the subiculum and the deep layers of the entorhinal cortex (Figure 1.6B).

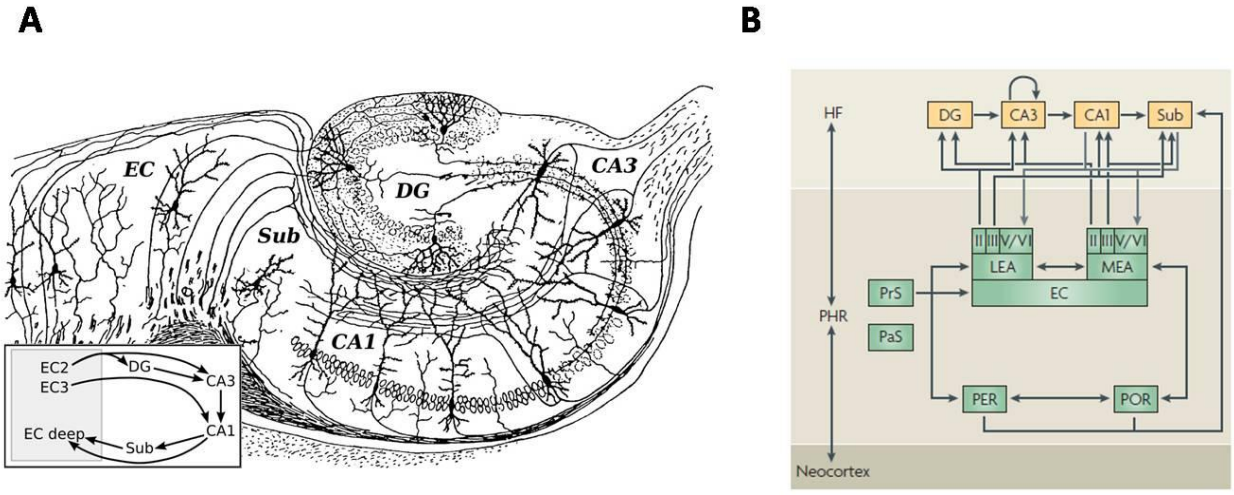

Figure 1.6: **A:** Modified from an original drawing of Cajal, showing the hippocampal subdivisions with its main cellular types and axonal pathways. **B**: Diagram of the classical schema of information flow in the hippocampal formation. Modified from Cajal, 2011 and Van Strien et al, 2009.

In addition to these excitatory connections, the activity in every node of the network is modulated by inhibitory synapses made by the large existing number and types of interneurons. In the HP, as well as in most of the other regions of the brain, together with the excitatory principal cells there are multiple classes of those inhibitory cells (Figure 1.7). The different types of interneurons have very different intrinsic properties, firing patterns and targets. Thus different roles and involvement in network activity have been proposed for them (Freund and Buzsáki, 1996, Klausberger and Somogy, 2008).

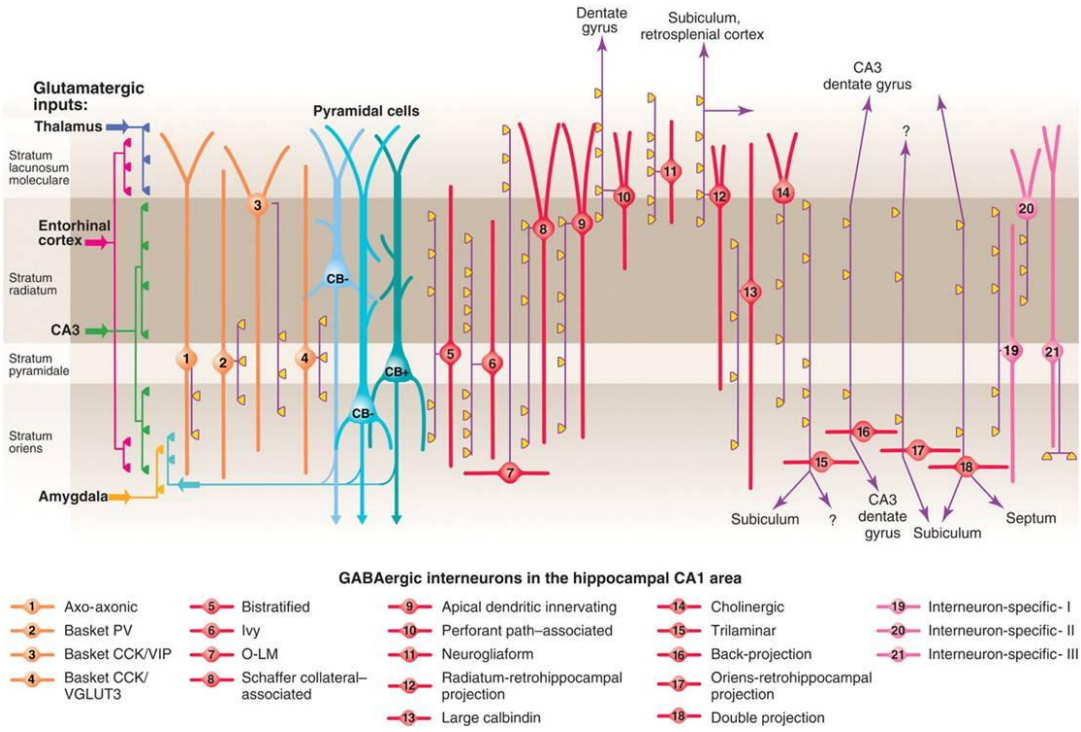

Figure 1.7: Subtypes of interneurons in the CA1 region. More than 20 types of interneurons have been defined in the hippocampus. Note the variability in synaptic domains of different interneurons onto CA1 pyramidal cells. Reproduced from Klausberger and Somogy, 2005.

One important characteristic of the HP and a big advantage to the study of their LFPs, as we will see below, is the stratification of their inputs. Different afferences to all hippocampal subregions have well defined dendritic domains. As it will be the focus of subsequent work, we will cover the case of DG and CA1. In the DG, MEC L2 axons establish synapses in the middle portion of the dendritic arbor of the granular cells while LEC L2 axons arrive in its outer part (Figure 1.8A). The inner portion of the dendritic arbor is innervated by commissural and

associational fibers. CA1 pyramidal cells have both basal and apical dendrites. The basal dendrites form the stratum oriens and the much larger apical ones extend into two sublayers: stratum radiatum and stratum lacunosum-moleculare. CA3 axons innervate the stratum radiatum and stratum oriens while entorhinal fibers arrive at the stratum lacunosum-moleculare and in lesser extent also at the stratum oriens (Figure 1.8B). Thalamic axons are also circumscribed to the stratum lacunosum-moleculare. It is worth to mention that both excitatory inputs also innervate several interneuron types, which in turn make synapses onto the principal cells and other interneurons.

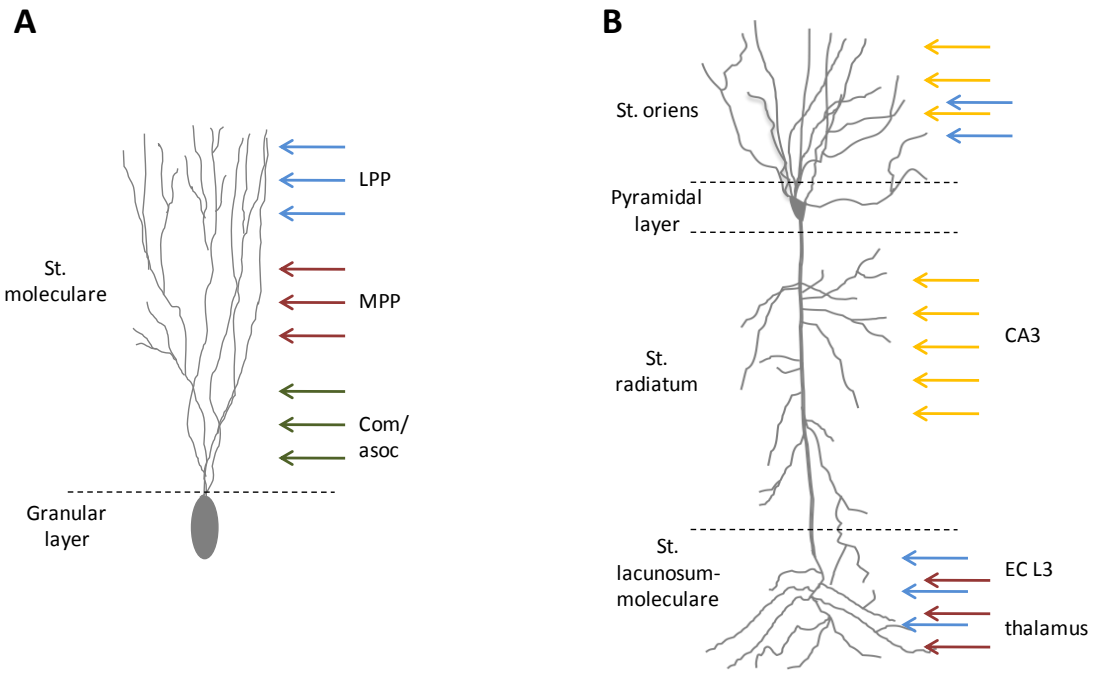

Figure 1.8: Diagram depicting the different sub-layers of the DG (**A**) and CA1 (**B**) regions of the hippocampus and their main afferences.

1.2.2 **Hippocampal LFP patterns**

The hippocampus displays very prominent LFPs that are strongly correlated with the behavior of the animal, thus were early used to study hippocampal function (Wishaw and Vanderwolf, 1973). During active locomotion and exploration and also during rapid-eye movement (REM), sleep hippocampal LFPs are dominated by a strong quasi-sinusoidal oscillation with a narrow power spectrum peaking around 7 to 9 Hz, known as theta oscillations

(Buzsáki et al., 1983; Figure 1.9A). Theta oscillations are coordinated in all hippocampal subregions and along the whole extent of the hippocampus (Buzsáki et al 1986; Patel et al 2012). They are also present at the same time and with high coherence in many other regions of the brain, mainly in the limbic system: entorhinal cortex, subiculum, piriform cortex, septum, etc. (Alonso and García-Austt, 1987). Over the last decades, there has been intense research to elucidate the generating mechanism of theta oscillations but the debate is still open (see Buzsáki 2002 for a comprehensive review). There is a consensus that the main theta rhythm generator is in the medial septum-diagonal band of Broca, which imposes its rhythm to the other regions. However some of these regions in isolation, even in vitro, can generate their own theta oscillations (Goutagny et al., 2009). When it comes to the generator of theta LFPs in the hippocampus and other regions, the picture is even more complex. Almost every hippocampal sublayer has its own theta current generator, that is current dipoles that contribute to the overall theta LFP (Leung 1984; Buzsáki et al., 2002). During different behaviors those theta dipoles are coordinated in a variable manner (Montogomery et al., 2009) modulating accordingly the spiking of hippocampal neurons. Pharmacological manipulations have been proved useful to dissociate and characterize the different synaptic generators of the theta rhythm in the hippocampus and other areas (Vanderwolf, 1988; Soltesz and Deschénes, 1993; Benito, Fernández-Ruiz et al., 2013; Newman et al., 2013) but we are still far from a comprehensive understanding of its mechanisms.

A rather opposite electrographic state to the one described above is present during immobility, consummatory behaviors and slow-wave sleep (SWS) and is characterized by more asynchronous activity and the presence of sharp-wave ripples (SWR) complexes. SWR are LFP patterns are composed by a large negative “sharp wave” in the stratum radiatum of CA1 accompanied by very fast (120-180 Hz) oscillations or “ripples” in the CA1 pyramidal layer (Bragin et al., 1995. Figure 1.9B). The CA1 sharp-wave is produced by a large depolarizing conductance in the apical dendrites of the pyramidal cells elicited by a highly synchronous firing of a large population of CA3 pyramidals. It has been proposed that its generation is controlled by the CA3 recurrent network and perisomatic-targeting interneurons (Hájos and Paulsen, 2009). The generation of CA1 ripples is less understood and several mechanisms ranging from inhibitory fast post-synaptic potentials (IPSPs), action potentials or a combination have been proposed (Ylinen et al., 1995; Schomburg et al., 2013; Ibarz et al., 2010). What is clear is that a

large population of both CA1 pyramidal cells and interneurons are firing synchronously during SWR (Csicvari et al., 2000), thus the output of the hippocampus to its target regions is enhanced. Much of the interest about SWR comes from the fact that they are strongly related to learning and memory consolidation (see Buzsáki, 2015 for a comprehensive review).

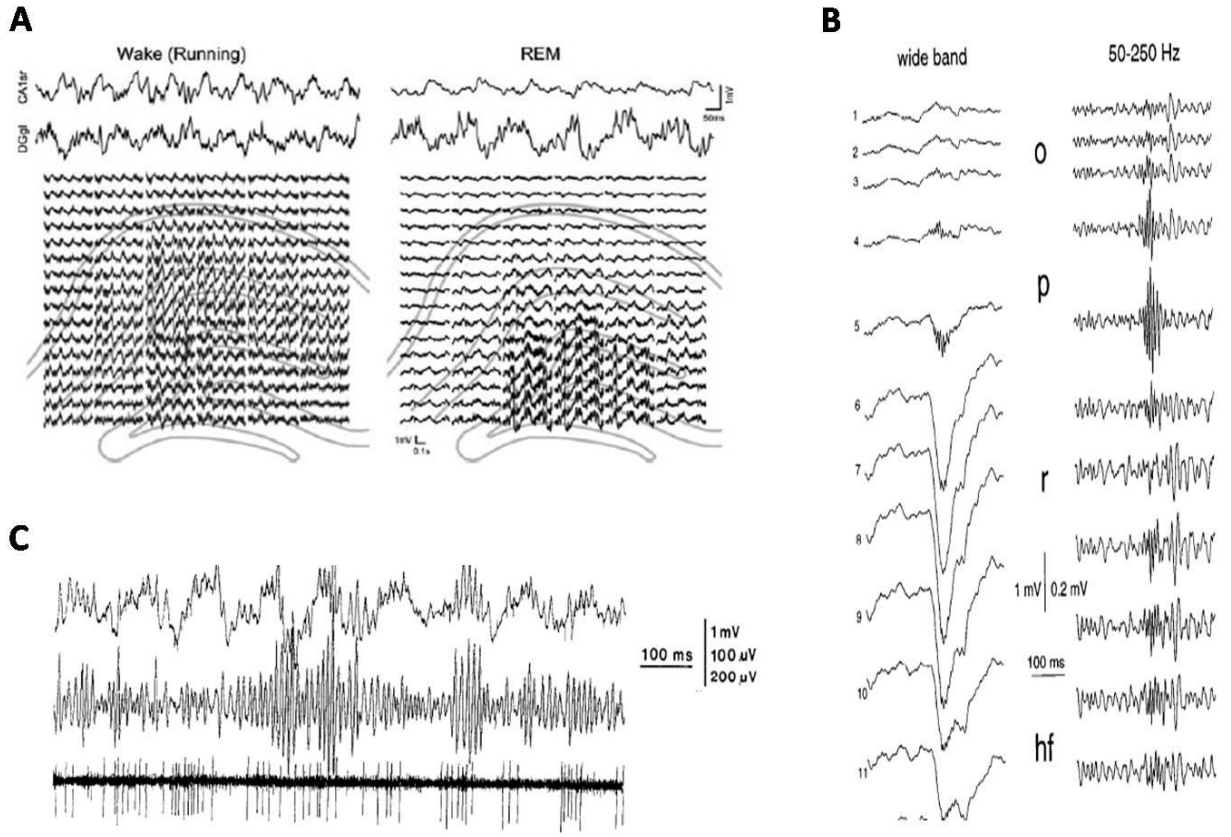

Figure 1.9: **A:** Theta oscillations in the hippocampus during active running and REM sleep appear across every subregion. Note the different power and frequency of oscillations in both behavioral states. **B:** SWR complexes are characterized by a strong negative deflection in the stratum radiatum(r) and simultaneous fast oscillation in the CA1 pyramidal layer (p). **C:** Gamma oscillations appear in the hippocampus in every layer, are modulated by the concomitant theta rhythm and entrain the firing of numerous local neurons. Modified from Montgomery et al., 2008; Ylinen et al., 1995; Bragin et al., 1995a.

Another ubiquitous LFP pattern not only in the hippocampus but in almost every brain region, mainly in the cortex, is that of gamma oscillations. Gamma oscillations (30-90 Hz) were originally studied in the neocortex and are related to different cognitive functions such as attention, sensory integration and learning (Signer and Gray 1996; Fries et al., 2007; Lisman and

Jensen, 2013). Several mechanisms have been proposed to explain its emergence and coordination (Buzsáki and Wang, 2012; Hájos and Paulsen, 2009; Csicvari et al., 2003). Most of them imply the interplay between excitation and inhibition in local networks. Of particular importance is the role of fast-spiking perisomatic-targeting interneurons that are thought to synchronize principal cells spiking in the gamma time scale to form cell-assemblies (Hájos et al., 2004; Klausberger and Somogy, 2008).

In the hippocampus gamma oscillations are present concomitantly with other oscillations mainly theta, which phase modulates gamma amplitude (Bragin et al., 1995; Chrobak and Buzsáki 1998. Figure 1.9C). Although initially gamma oscillations were considered a unitary phenomenon, evidence suggests that there is an enormous diversity of mechanisms and functions implying different gamma patterns. In every hippocampal subregion, gamma oscillations of different frequency, ranging from the slow gamma spectrum (30-50 Hz) to the very fast (100-200 Hz), can be observed and have different laminar distributions, synaptic mechanisms and behavioral correlates (Cscivari et al., 2003; Belluscio et al., 2012; Schomburg, Fernández-Ruiz et al., 2014; Zemankovics et al., 2013).

On the core of the neural computations performed by the hippocampus is the synchronous activation of neuronal assemblies whose temporal dynamics may govern the processing and flow of information in brain circuits. According to the "cell assembly" hypothesis (Hebb, 1949; Harris, 2005), information in the brain is represented by groups of synchronously firing neurons, whose membership reflects an interaction between sensory input and internally gen0erated patterns. A prominent role in forming these assemblies is ascribed to gamma oscillations. For example, place cells representing the same spatial position, fire together in the time window of gamma cycles and are often phase-locked to the same gamma frequency (Harris et al., 2003). Neuronal assemblies organize in specific temporal sequences, which have been shown to encode past (recall) and future (planning) aspects of the behavior of the animal (Dragoi and Buzsáki, 2006). A postulated mechanism for generating assembly sequences is the interaction among the multitude of brain oscillations organized by cross-frequency coupling (Buzsáki and Draguhn, 2004). In the hippocampus and entorhinal cortex the phase of theta rhythm has been shown to modulate the power of gamma oscillations according to behavioral demands, as well as the firing

of both principal cells and interneurons. Thus, the function of theta rhythm may be to organize in a broader scale the gamma time-scale cell assemblies (Lisman and Jensen, 2013).

1.3 Goals of the Thesis

The general aim of the present thesis is to perform an experimental and computational study of the biophysical and physiological basis of macroscopic brain signals. For this purpose, we will focus on the rodent hippocampal LFPs.

The first goal of the thesis will be a methodological one. We will implement a novel approach to analyze and interpret the large amount of information contained in large-scale recordings of LFPs in behaving rodents. In particular, we will tackle the problem of separate and identify the contributing synaptic sources of the LFPs (the "inverse problem"). On a first stage, this goal will be addressed by the application of advanced mathematical tools such as the Independent Component Analysis (ICA) and the Current Source Density (CSD) analysis. For an adequate use of those methods it would be necessary a detailed spatial mapping of LFPs along different axis of the structure of interest, the hippocampus. On a second stage, we will build a tridimensional model of the rat dorsal hippocampus. In such model the spatiotemporal characteristics of hippocampal LFP sources will be implemented and the corresponding electric potential distributions solved for the whole structure by means of Finite Elements Method (FEM; the "forward problem"). The comparison of the results from the experiments and simulations will allow us to reach a better understanding of the generation of LFPs in the hippocampus and the accuracy of the solutions found for their inverse problem.

The second goal will be to study how different structural (neuron morphology, tissue geometry, synaptic arrangement) and dynamical (synaptic synchrony, spatial input correlation) factors shape the generation and propagation of LFPs. For this purpose, we will focus on the Dentate Gyrus and perform simulations in which those factors are systematically changed and comparing the obtained results with those observed in the experimental data.

The third goal will be to characterize the oscillatory dynamics of hippocampal LFP sources during different behavioral states. We will perform a time-frequency decomposition of

the different LFP sources with a special emphasis on the generation of gamma oscillations and their coordination by the theta rhythm. This analysis will be performed during sleep, exploration and learning to study if theta-gamma dynamics in the hippocampus can shed light on the mechanisms of information processing by hippocampal circuits during behavior.

We expect that the successful consecution of the aforementioned goals will contribute towards a deeper understanding of the generation of macroscopic brain signals and will lead us to reach a better interpretation of neural oscillations in terms of their underlying physiological mechanisms.

2. Methods

2.1. Experimental procedures

Chronic recordings were performed in the Langone Medical Center of the New York University and the Department of Physiology of the School of Medicine of the University of Szeged. All experiments were performed in accordance with European Union guidelines (2003/65/CE) and the National Institutes of Health Guidelines for the Care and Use of Animals for Experimental Procedures. The experimental protocols were approved by the Animal Care and Use Committee of New York University Medical Center and the Ethical Committee for Animal Research at the Albert Szent-György Medical and Pharmaceutical Center of the University of Szeged respectively. Animals were anesthetized with isoflurane anesthesia and one or several craniotomies were performed with stereotaxical guidance. One or more silicon probes were mounted in custom-made micro-drives to allow their precise vertical movement after implantation. The probes were inserted over the target region and the micro-drives attached to the skull with dental cement. The craniotomies were sealed with sterile wax. Two stainless steel screws were drilled over the cerebellum and serve as ground and reference for the recordings. Several additional screws were drilled into the skull and covered with dental cement to strengthen the implant. Finally a copper mesh was attached to the skull with dental cement and connected to the ground screw to act as a Faraday cage and prevent the recording from the environmental electric noise (Figure 2.1A. For more details see Vandecasteele et al., 2012). After recovery, the probe is moved gradually in 70 to 150 μm steps until the desired target is reached. The operated animals were housed in individual cages.

To record neuronal activity during sleep or waking behaviors the probes were connected to a pre-amplifier headstage attached to a long cable pending from the room ceiling that allow full movement to the animal (Figure 2.1B). The rats' positions during behavioral sessions were estimated using video tracking of two LEDs fixed to the headstage. The wide-band signal was low-pass filtered and down sampled to 1250 Hz to generate the LFP and was high-pass filtered (>0.8 kHz; 20 kHz) for spike detection.

Following the termination of the experiments, the animals were deeply anesthetized, and transcardially perfused first with 0.9% saline solution followed by 4% formaldehyde solution. The brains were sectioned by a Vibratome (Leica) at 70 µm sections, parallel with the plane of the implanted silicon probes.

For some of the analysis presented here another dataset was also included. It comprised recordings form the medial entorhinal cortex and hippocampus performed with high-density 32 or 64 electrode (Buzsáki-probes, Neuronexus) while the rats performed different maze tasks or sleep in their home cages. This dataset is publically available at http://crcns.org (hc-3 dataset, Mizuseki et al., 2014).

The experimental data analyzed for the present thesis were not entirely recorded by me but by other researchers from the Buzsáki laboratory (NYU): Antal Berényi, Sean Montgomery, Kenji Mizuseki and John Long.

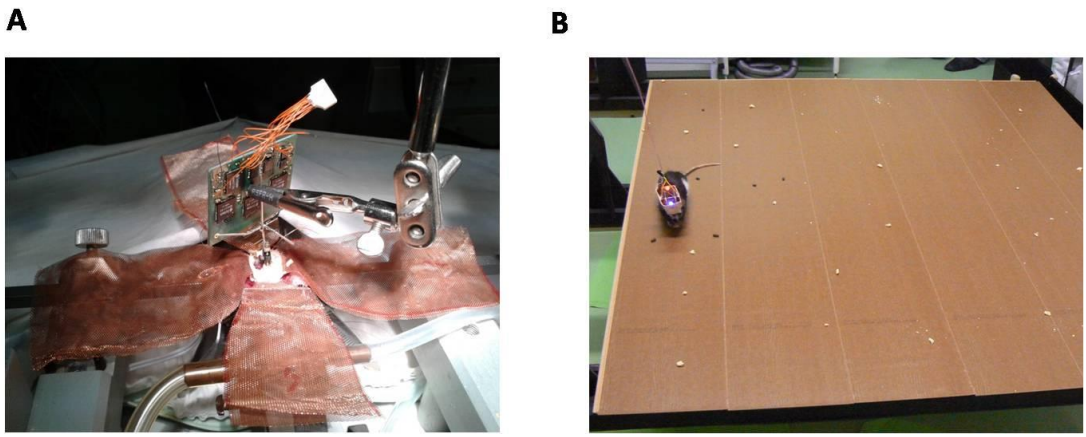

Figure 2.1: **A**: Implantation of a 256 channels silicone probe (NeuroNeuxus) in the hippocampus of a Long Evans rats. Observe the multiplexed pre-amplifier PCB and the microdrive where the probe is mounted. **B**: An animal being recorded during exploration for food reward (cookies) in an open field. Two LEDs mounted in the headstage are used for position tracking.

2.2. LFP source decomposition

All the LFP pre-processing and analysis were conducted with custom-made functions or publically available toolboxes in MATLAB (The MathWorks, Inc.).

To address the inverse problem of LFP, that is, to separate the different sources that contribute to the mixed signal, we employed a combination of independent component analysis (ICA) and current source density (CSD) analysis.

2.2.1. Independent Component Analysis

ICA is a blind source-separation technique (Comon, 1994; Bell and Sejnowski, 1995; Hyvärinen et al., 2004) that can isolate spatially segregated stable patterns of activity in a mixed signal recorded with an array of sensors. Applied to linear profiles of LFPs it can separate physiologically meaningful sources that can be attributed to known anatomical pathways. ICA is able to find the original sources that are statistically independent in a linear mixture. This can be achieved by different ways, thus many different ICA algorithms have been proposed that, although numerically different, are equivalent from a theoretical point of view (Hyvärinen and Oja, 2000; Choi et al., 2005). We employed the logistic infomax ICA algorithm (Bell and Sejnowski, 1995) as implemented in the EEGLAB toolbox (RUNICA; Delorme and Makeig, 2004) and the fast kernel density ICA algorithm provided by A. Chen (KDICA, http://cm.bell-labs.com/who//aychen/ica-code.html; Chen, 2006). Both algorithms give very similar results.

The application of ICA to a blind source separation problem can be formulated as follows:

Given a linear mixture of n sources $x_1,\ldots,x_n$ that are independent from each other (that is, observing the dynamics of one of them does not give any information about the dynamics of the others), the problem is to separate the source signals given only the mixture

$$x_j(t) = a_{j1}s_1(t) + a_{j2}s_2(t) + \cdots + a_{jn}s_n(t) \qquad (2.1)$$

For the following explanation we will eliminate the temporal dimension and denote by x the column vector whose elements are the mixture signals $x_1,\ldots,x_n$ and by s the column vector whose elements $s_1,\ldots,s_n$ are the independent sources:

$$x = As \qquad (2.2)$$

A is the mixing matrix with elements a_{ij}. The above equation can also be formulated as:

$$x_j = \sum_{i=1}^{n} a_{ji}\, s_i \qquad (2.3)$$

The above equation is called the statistical ICA model. It is a generative model because it describes how the observed mixed signal is generated by an iterative process of mixing of the independent components s_i. The components cannot be directly observed, they are latent variables. Also the mixing matrix ***A*** is a priori unknown. We only observe the mixed signal ***x*** and have to estimate both ***A*** and ***s***. After that we can, just by means of an inverse transform, obtain the independent components:

$$\mathrm{s} = \mathrm{W}\,\mathrm{x} \qquad (2.4)$$

where ***W*** is the inverse matrix of ***A***.

A common first step in the ICA is to sphere or whiten the mixed signals; that is, to remove any existing correlations. If $\boldsymbol{C = E\{xx'\}}$ is the correlation matrix of the mixed signals, the sphering can be accomplished by the linear transformation $\boldsymbol{V = C^{-1/2}}$

$$E\{yy'\} = E\{Vxx'V'\} = C^{\frac{1}{2}} \cdot C \cdot C^{-\frac{1}{2}} = I \qquad (2.5)$$

After sphering the independent components can be estimated by and orthogonal transformation of the uncorrelated signals ***y***. This is achieved by a rotation of the joint density ***p(y)***. The appropriated rotation is sought by maximizing the non-Gaussianity of the marginal densities of ***p(y)***. This relays on the assumption made by ICA (as stated by the central limit theorem) that any linear mixture of independent random variables has necessarily a more Gaussian distribution that the original variables. Most ICA algorithms perform this rotation of the joint density of the signals in an iterative way until it converges. That is achieved when the joint density becomes a product of the marginal densities:

$$p(s) = p(s_1) \cdot p(s_2) \cdots p(s_n) \qquad (2.6)$$

The ICA model makes several assumptions that must be fulfilled for the data in order to reach an accurate result (Hyvärinen et al., 2004; Brown et al., 2001): (1) Sources must be stationary. In the context of LFPs, the sources are mainly synaptic transmembrane currents in

fixed locations as determined by anatomy (Buzsáki et al., 2012). (2) The sources should not have Gaussian-distributed activation strengths, which is the case for brain dynamics (Buzsáki and Mizuseki, 2014). (3) The mixture of the sources must be linear and instantaneous, which can be assumed for electric fields elicited by ionic currents in the extracellular space (Plonsey and Heppner, 1967; Nunez and Srinivasan, 2006). (4) The number of sources must be equal or less than the number of sensors, which makes high-density electrode recordings particularly suitable for application of ICA. (5) It is assumed that the observed variable (in this case the LFP) is a mixture of scalar, one dimensional sources. It implies that if the same oscillatory source is observed with a phase delay by different electrodes, then ICA will decompose it into two ICs with a 90 degree phase delay. The temporal activation of the original source would correspond to a linear combination of the time series of those two ICs. Thus, it is important to stress that, though spatially distinct sources which are *perfectly* coherent cannot be properly separated, ICA does not find independent components (ICs) with true temporal independence, and temporal correlations and coherence measures may still be applied to analyze the temporal relationships between the resulting ICs (Bell and Sejnowski, 1995; Hyvärinen et al., 2004; Choi et al., 2005; Fernández-Ruiz et al., 2013).

Our case is that of multiple simultaneous samplings of the mixed signal (the raw LFP recorded by every electrode, Figure 2.2A). The time series of the LFP recorded by each electrode are the rows of the data matrix $\boldsymbol{D}$. ICA finds the square matrix $\boldsymbol{W}$ (with dimensions equal to the rows of $\boldsymbol{D}$) such that $\boldsymbol{WD} = \boldsymbol{C}$. $\boldsymbol{W}$ is the unmixing matrix because it separates the mixture of signals that is $\boldsymbol{D}$ into its independent sources. $\boldsymbol{C}$ has the same dimensionality as $\boldsymbol{D}$, with each of its rows being the time series of an independent component (Figure 2.2C, lower panel). Each independent component is obtained by multiplying each sampled signal by each row of $\boldsymbol{W}$ (the so called unmixing functions or ICA filters). This process can be also view as solving the inverse problem of the LFP; that is estimate the sources giving only the potentials distribution.

The inverse of the mixing matrix $\boldsymbol{W}$ that transforms the LFP data into the ICs gives the channel weight of each component that is captured for each sensor. When plotted according to the anatomical location of the electrodes, this corresponds to the spatial voltage loadings of each IC (Figure 2.2C, upper panel). We ranked the components by the amount of variance they explain in the original data (*relative power*). Once ICs have been extracted from the raw LFP

traces, they can be analyzed as if they were active independently from activities at other locations. We reconstructed the virtual LFP produced by a single IC by multiplying the IC time course by its correspondent voltage loading (Figure 2.2D). For each component *a*, that is achieved by

$$W_a^{-1} C_a = D_a \qquad (2.7)$$

That is also known as solving the forward problem, or reconstructing the potentials distribution given the current sources.

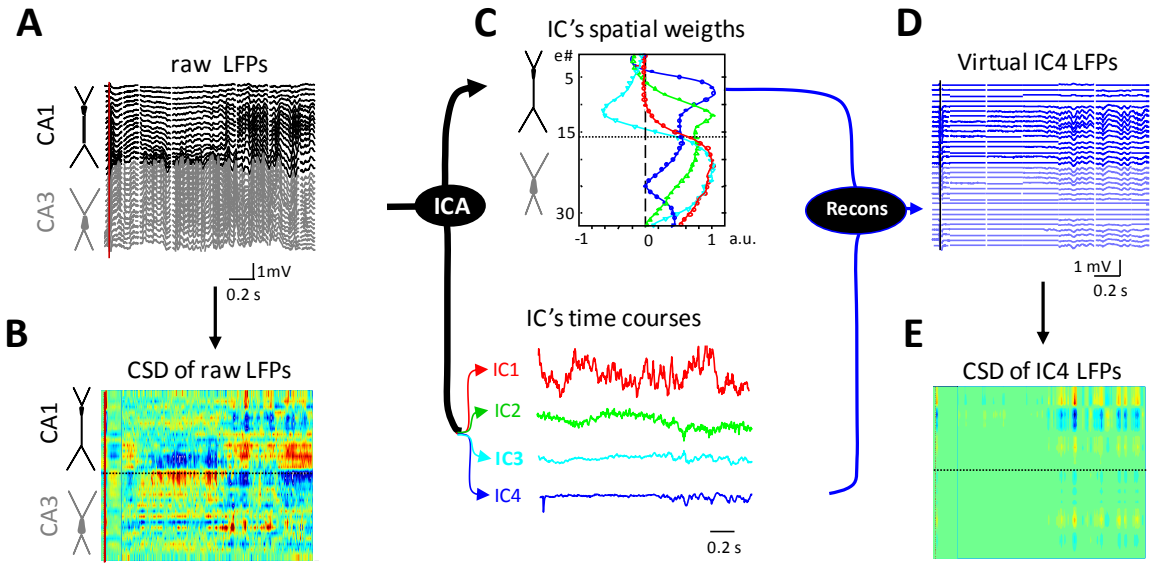

Figure 2.2: **A**: Raw LFPs along the CA1 and CA3 hippocampal subfields (black and gray traces, respectively). **B**: CSD of the LFPs renders a complex mixture of currents as expected for multiple synaptic inputs. **C**: ICA of LFPs provides four main ICs, each defined by the curve of spatial weights (top panel) and a time course (bottom traces). **D**: Reconstructed (virtual) LFPs for IC4. **E**: CSD of the virtual LFPs provides precise spatiotemporal maps of inward/outward currents for unique spatially coherent synaptic input. Modified from Fernández-Ruiz et al., 2012a.

Before application of the ICA algorithm, we performed several pre-processing steps. For hippocampal LFPs, there are only a small number of physiologically meaningful ICs with significant amplitude and identifiable spatial loadings (Fernández-Ruiz et al., 2012a, 2012b; Fernández-Ruiz et al., 2013; Benito et al., 2014). Before applying ICA, we therefore employed a principal component analysis (PCA) reduction maintaining 98.0 % of the original LFP variance.

This process aids in the convergence of ICA to stable components, and results in a smaller number of ICs. We also whitened the data before applying ICA to reduce the computational complexity of the analysis while maintaining its statistical consistency (Hyvärinen and Oja, 2000; Chen and Bickel, 2005).

Due to the parallel anatomical arrangement of the principal cells and the stratification of afferent axon terminals, the hippocampus is especially well suited for ICA decompositions of its LFPs. However, only those synaptic inputs with enough postsynaptic current, synchrony, and spatial clustering are suitable for ICA separation; thus, very weak or sparse currents are not easily discernible.

2.2.2. Current Source Density Analysis

The traditional approach to solve the inverse problem of the LFPs is performing current source density (CSD) analysis. CSD analysis (Freeman and Nicholson, 1975; Mitzdorf, 1985) determines the magnitude and location of the net transmembrane currents generated by neuronal elements within a small volume of tissue.

In a macroscopic level the transmembrane current density I_m per unit length is related with the extracellular current density $\boldsymbol{J}$ through the divergence:

$$\nabla \boldsymbol{J} = I_m \tag{2.8}$$

If we assume a quasistatic description of the electric field in the extracellular medium (neglecting capacitive and inductive effects), Ohm law can be applied,

$$\boldsymbol{J} = \sigma \boldsymbol{E} \tag{2.9}$$

where σ is in general the conductivity tensor.

The relation between the electric field $\boldsymbol{E}$ and the extracellular potential Φ

$$\boldsymbol{E} = -\nabla \Phi \tag{2.10}$$

allows us to establish a linear dependency between the extracellular current density $\boldsymbol{J}$ and the

gradient of the electric potential in the medium

$$\boldsymbol{J} = -\sigma \nabla \Phi \tag{2.11}$$

Substituting this expression of $\boldsymbol{J}$ into the current conservation equation, we get the Poisson equation, which establishes the relation between the electric potential and the volumetric current density

$$\nabla \sigma \nabla \Phi = -I_m \tag{2.12}$$

In the simplest approach, we employed a 1D approximation by calculating the second spatial derivative of the LFP profiles (Figure 2.2 B), and calculated the CSD according to a central differences formula,

$$CSD(z_i) = -\sigma \frac{\Phi(z_i + \delta) - 2\Phi(z_i) + \Phi(z_i - \delta)}{\delta^2} \tag{2.13}$$

where δ is the distance between electrodes.

This approach assumes isotropy and negligible net contributions in the XY-plane perpendicular to the cellular axis. That is suitable for laminated structures with parallel arrangement of principal cells, as is the case of CA1, if the recording electrodes are placed parallel to the main cell axis (z) and an homogeneous population of cells is synchronously active (as for example during evoked potentials). In this traditional approach to CSD estimation it is also assumed homogeneous resistivity.

However, the above assumptions are not fulfilled in most real cases. When the cells in a small volume of tissue are active only in a given time there can be a significant current spreading in the x and y directions. This may result in an underestimation of true sink and sources as well as in the occurrence of spurious ones. To address those issues we employed the recently developed inverse CSD (iCSD) method (Pettersen et al., 2006). This method consists of first define a forward model to describe the potentials that are produced by localized current sources and then invert this model by means of a numerical matrix inversion to allow direct calculation of localized discrete sources form the measured potentials distribution. The solution of the forward model is given by the following equation

$$\Phi(r_e) = \frac{1}{4\pi\sigma} \iiint_V \frac{CSD(r)}{|r - r_e|} d^3r \qquad (2.14)$$

In most LFP studies the application of CSD analysis does not take into account tissue inhomogeneity and anisotropy effects, assuming a negligible contribution of these effects (Buzsáki et al., 2012; Einevoll et al., 2013). In the present work we with also adopted this approach; however we took advantage of the iCSD method to explicitly incorporate a priori knowledge about the geometry of the sources, such as the volume of activated tissue and the relative position of the sources to the recording electrodes.

In addition to the raw LFP we performed CSD analysis of the reconstructed virtual LFP produced by a single IC, which renders a map of the current distribution of a single anatomical input or LFP source (Fernández-Ruiz et al., 2012a).

2.3. Time-frequency analysis of LFPs

To characterize the LFP signals in the spectral domain we employ a multi-taper implementation of the fast Fourier transform (Mitra and Pesaran, 1999; Chronux toolbox, http://www.chronux.org). Continuous data were segmented in 1-5 seconds epochs for all spectral analysis. Spectral power was estimated with a Hanning window and averaged across all data epochs.

In the multi-taper power spectrum method employed here a set of independent estimates of the power spectrum are computed, by multiplying the signal by orthogonal tapers (windows) which are constructed to minimize the spectral leakage due to the finite length of the data set. The tapers are the discrete set of eigenfunctions that solve the variational problem of minimizing leakage outside of a predefined frequency band. Once the tapers $\boldsymbol{w_k}(t)$ are computed for a chosen frequency bandwidth, the total power spectrum $\boldsymbol{P_X}$ can be estimated by averaging the individual spectra given by each tapered version of the time series $\boldsymbol{x}(t)$; the kth eigenspectrum $\boldsymbol{X_k}$ is the discrete Fourier Transform of $\boldsymbol{x}(t)\boldsymbol{w_k}(t)$

$$P_x(f) = \frac{\sum_{k=1}^{K} \mu_k \left| X_k(f) \right|^2}{\sum_{k=1}^{K} \mu_k} \tag{2.15}$$

This procedure yields a better and more stable estimate of a signal power spectrum than single taper methods.

Two basic measures of pairwise synchronization were employed: cross-correlation and coherence. The cross-correlation function is a measure of the linear covariance between two signals ***x*** and ***y*** and can be estimated as follows,

$$cc_{xy} = \frac{\sum_{k=1}^{n} \left(x_k - \bar{x} \right) \left(y_k - \bar{y} \right)}{\sqrt{\sum_{k=1}^{n} \left(x_k - \bar{x} \right)^2} \cdot \sqrt{\sum_{k=1}^{n} \left(y_k - \bar{y} \right)^2}} \tag{2.16}$$

where $\bar{x}$ and $\bar{y}$ are the means of the respective signals.

This method has the advantages of being a straightforward method that yields a normalized value giving a gross indication of the degree of similarity of two signals (i.e. LFPs recorded at separate locations). However, for a frequency resolved estimate of the linear covariance of two signals we need to employ the coherence.

$$coh_{xy}(f) = \sqrt{\frac{\left| \left\langle C_{xy}(f) \right\rangle \right|^2}{\left| \left\langle C_{xx}(f) \right\rangle \right| \cdot \left| \left\langle C_{yy}(f) \right\rangle \right|}} \tag{2.17}$$

where $\boldsymbol{C_{xx}(f)}$ is the cross-spectral density for the frequency *f* between ***x*** and ***y***, and $\langle ... \rangle$ indicates averaging over segments.

To assess spectral events at a high resolution in time and frequency, the complex wavelet transform (CWT) of the LFP was calculated using complex Morlet wavelets (Torrence and Compo, 1998). The CWT gives amplitude and phase measures for each wavelet scale at all time

points in the data, obtained by convolving the real and imaginary parts (which are phase shifted by 90^o) of the wavelets with the data vectors.

A wavelet is a scalable function with zero mean, well localized in time.

$$\int_{-\infty}^{\infty} \psi(t)dt = 0 \tag{2.18}$$

A family of wavelets can be constructed from a "mother" function $\Psi(t)$,which is confined to a finite interval, translated with a factor *u* and expanded with a scale parameter *s*,

$$\psi_{u,s}(t) = \frac{1}{\sqrt{s}} \cdot \psi\left(\frac{t-u}{s}\right) \tag{2.19}$$

Then the wavelet analysis of a signal *x* can be performed by

$$\left\langle x(t), \psi_{u,s}(t) \right\rangle = \int x(t)\psi_{u,s}(t)dt \tag{2.20}$$

In our case we employed the Morlet complex waveform,

$$\psi(t) = \left(e^{i\omega_0 t} - e^{-\omega_0^2\sigma_t^2/2}\right) \cdot e^{-r^2/2\sigma_t^2} \tag{2.21}$$

where ω_0 is the center frequency of the wavelet and σ_t a bandwidth parameter determining its rate of decay. The width or number of cycles of the wavelet is given by $\omega_0\ \sigma_t^2$.

If this complex wavelet is convolved with the signal *x* we get the CWT of that signal,

$$W(t) = (\psi \circ x)(t) = \int \psi\ (t'\mathrm{x}(\mathrm{t}-t')\,dt' = \mathrm{A}^W(\mathrm{t})\,\mathrm{e}^{i\phi_W(t)} \tag{2.22}$$

where $\phi_W(t)$ is the phase for each time sample. The Morlet mother waveform has Gaussian modulation in both time and frequency, thus offering optimal resolution in both domains.

The simpler Hilbert transform was also employed in some cases (as when only the theta oscillations were considered) to extract the phase or amplitude of LFP signals. The phase $\phi_W(t)$

and amplitude $A_x(t)$ are given respectively by the argument and modulus of the complex analytical signal:

$$\xi(t) = x(t) + ix_H(t) = A_x(t)e^{i\varphi_x(t)} \quad (2.23)$$

where $x_H(t)$ is the Hilbert transform of $x(t)$, defined as:

$$x_H(t) = \frac{1}{\pi} P.V. \int_{-\infty}^{\infty} \frac{x(t')}{t - t'} dt' \quad (2.24)$$

with *P.V.* denoting the Cauchy principal value.

Both wavelet and Hilbert transforms give very similar results in all cases.

The phase-amplitude cross-frequency coupling (CFC) during theta oscillations for a given LFP recording was assessed using the modulation index (MI) introduced by Tort et al. (2008).We took the phase of the LFP recorded at the CA1 pyramidal cell layer and the amplitude of either LFP recorded in different layers or the time course of different LFP-generators, in all cases the procedure was exactly the same. The raw LFP signal (Figure 2.3A) was band-pass filtered in the low frequency band (Figure 2.3B) and the phase of the analytic signal given by the Hilbert transform or CWT was calculated (Figure 2.3C). Amplitude of the filtered signal in the broad gamma band (30-300 Hz, Figure 2.3D) was also obtained from the CWT. The MI was calculated by measuring the divergence of the observed amplitude distribution from the uniform distribution (Figure 2.3E). Comodulogram phase-amplitude plots were constructed representing in pseudocolor scale the MI values of multiple phase-amplitude frequency pairs (Figure 2.3F). The statistical significance of the MI values (P-value) was assessed by a surrogate analysis (n=1000 surrogates) with random shifts between the phase and amplitude time series (Canolty et al., 2006).

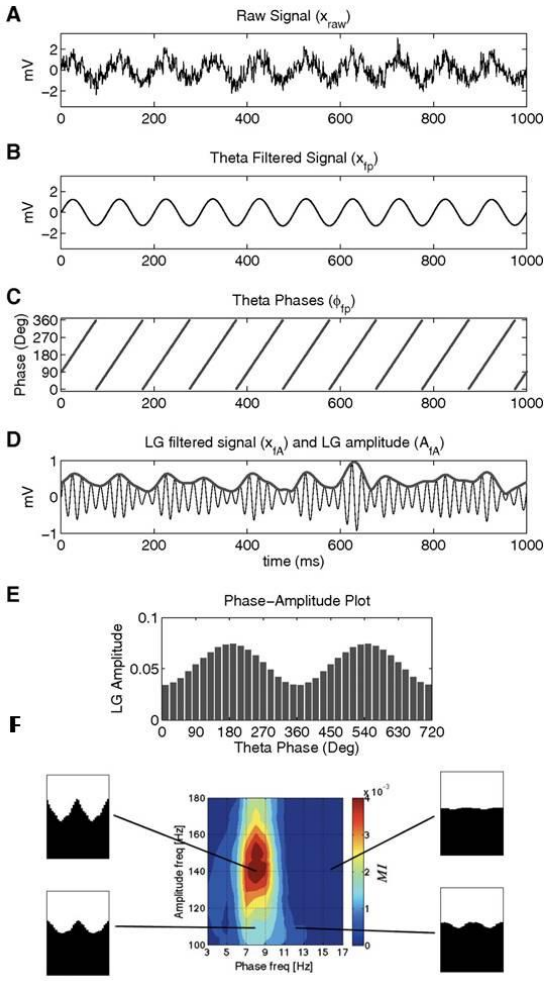

Figure 2.3: **A**: Example of raw LFP signal. After filtering in the theta band (B), the phase is calculated using the Hilbert transform. **C**: The same or other signal is filtered in the frequency band of interest and its amplitude (**D**) is obtained from the CWT. The mean amplitude distribution over theta phase is then calculated (**E**). The phase-amplitude MI is obtained by measuring the divergence of the observed amplitude distribution from the uniform distribution. A phase-amplitude comodulogram plot is constructed representing in pseudocolor scale the obtained MI values for multiple phase-amplitude pairs (in this case the phase was not only calculated for the theta filtered signal but for a range of frequencies). Modified from Tort et al., 2008 and Tort et al., 2011.

2.4. Single unit analysis

Neuronal spikes were detected from the digitally high-pass filtered LFP (0.8–5 kHz) by a threshold crossing-based algorithm (*Spikedetekt2*; https://github.com/klusta-team/spikedetekt2). Detected spikes were automatically sorted using the masked EM algorithm for Gaussians

mixtures implemented in KlustaKwik (Kadir et al., 2014; https://github.com/klusta-team/klustakwik/), followed by manual adjustment of the clusters using the KlustaViewa software (Rossant et al., 2015; https://github.com/klusta-team/klustaviewa/; Figure 2.4) to get well-isolated single units. Multiunit or noise clusters where discarded for the analysis. Putative pyramidal cells and interneurons were separated on the basis of their autocorrelograms and waveforms characteristics (Csiscvari et al., 1998; Stark et al, 2014; Mizuseki et al., 2009), assisted by monosynaptic latency excitatory and inhibitory interactions between simultaneously recorded, well-isolated units (Bartho et al., 2004; Mizuseki et al., 2009). Most of the unit clustering and classification were performed by Kenji Mizuseki at the Buzsáki laboratory.

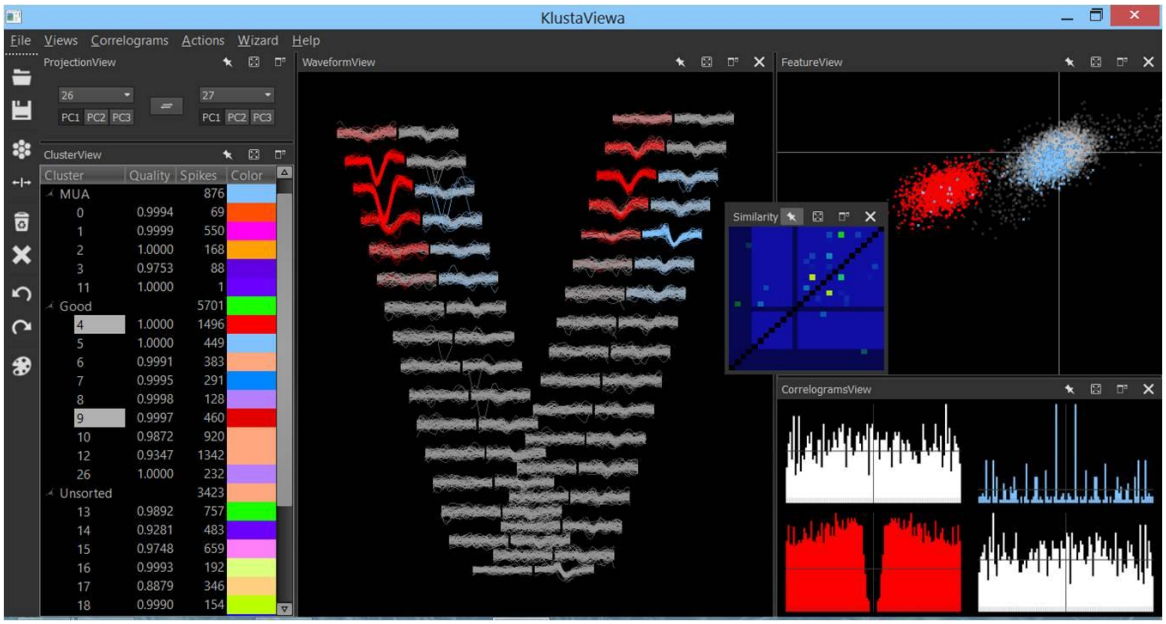

Figure 2.4: Screen capture from KlustaViewa, an open-source software for manual clustering of neuronal spikes. In the central panel two single units with different anatomical location are displayed. Observe the different features provided for assisting the process: auto and cross-correlograms. PCA projections, similarity matrix. From Rossant et al., 2015.

The phase-locking of spikes to the LFP was measured for individual units using the wavelet or Hilbert phase at the time of each spike. Modulation indices were calculated using the mean resultant length of the phases, and significance was estimated applying the Rayleigh test for non-uniformity using the circular statistics toolbox provided by P. Berens (Berens, 2009). Unit-LFP analyses were implemented by Erik Schomburg at the Buzsáki laboratory.

2.5. Modeling of LFPs with finite elements method

Multiple physical problems can be mathematically formulated as a partial derivatives differential equation. As a general rule, those differential equations are very hard to solve. Only in those cases in which it is possible to make simplifications on the dimensionality and geometry of the problem an analytical solution is available. However, in most of the cases analytical methods are not feasible or are inexact (as can be the case of a tridimensional electromagnetic problem in a complex geometry). For solving this kind of problems numerical models are necessary and useful. Those methods discretize the differential equation into a linear system of equations, solving it in an iterative way. One of those methods is the analysis by means of finite elements (FEM).

The basis of FEM is to divide the geometry in which a differential equation of a scalar or vector field needs to be solved (i.e. the electric potential) in small elements, typically tetrahedral. In each element field equations determined by a variational principle and local sources are solved. Boundary conditions are applied and thus it is possible to obtain the algebraic system from which a solution of the problem is found. FEM allows explicit models of the geometry and electrical properties of the brain to be generated and to solve potential and current distributions in such a complex structure over time. In our case, the physical problem that needs to be solved with FEM can be described as follows. The initial condition is a certain distribution of volumetric current sources in a tridimensional complex structure (i.e. the rat hippocampus). Each of the sources is simultaneously activated with different time series. As a result of the uneven spatiotemporal varying summation of currents in the volume an electric potential distribution arise. Thus our goal is to calculate this potential distribution for each spatial point at anytime.

As such, we modeled the rat hippocampus establishing the geometry of current sources and their temporal activation, and fixed the boundary conditions. Two different models were built, one of the whole dorsal hippocampus in its planar section, and another of just the dentate gyrus region. The structure was enclosed in a larger volume simulating the extracellular space. This outer compartment was sufficiently large so as not to distort the field lines in the central region of interest. We tested different surrounding volumes (up to four times longer in each direction) while maintaining boundary conditions. The chosen volume rendered LFPs that

were at least 90% of the maximum amplitude obtained with the largest volume (>95% in most tested points). For the sake of simplicity, the tissue was considered to be purely resistive, isotropic and homogeneous (Logothetis et al. 2007; but see Bédard and Destexhe, 2011). The volumetric character of FEM current sources allows the electrical currents produced by multiple synchronously activated neurons to be compiled in a few block-like current generators that jointly obey the principle of charge conservation. This is an important advantage, which makes it suitable to reproduce LFPs in a volume generated by activated sections of layered structures made up of neurons arranged in parallel as is the case of the hippocampus or cortex. Accordingly, the size and geometry of the blocks of current represent the physical extension of the synchronously activated neurons, i.e., the portion of the population of cells that elicits postsynaptic currents upon coherent activation of a group of axons from homologous afferent units (Figure 2.5A).

We found that eighth of these blocks with 100 μm thickness in the case of CA1 and four 60 μm thickness block for each blade of the DG were sufficient to reproduce the main laminar features of hippocampal LFPs. In the case of CA1, one for the basal dendrites, one for the pyramidal cell body layer and six for the apical dendrites. For the DG, one block represented the granular cell body layer and three the dendrites. These blocks were bent to replicate the curved geometry of the hippocampus and divided into approximately 200 μm sections that could be independently activated to analyze the effects of the spatial coherence and synchrony of the inputs. For simplicity, we used non-overlapping blocks of current, representing inputs with imaginary topological projection of varying synaptic territories.

In the present models we excluded any possible contribution of the extracellular currents from other cellular elements apart from pyramidal and granular cells (e.g. interneurons or glia). Most of those others types of cells have multipolar dendritic trees (Amaral, 1978) and hence, a closed-field extracellular configuration of the electric field is established by their synaptic activation (Lorente de Nó, 1947). Consequently, their currents do not (or they only poorly) spread beyond their physical limits (Lindén et al., 2011; Einevoll et al., 2013; Buzsáki et al., 2012). In consequence, these cells do not add their currents in the extracellular space and they only negligibly contribute to the LFP (even if some subtypes are strongly synchronized). Indeed, the results presented in the experimental section justify their omission from the model.

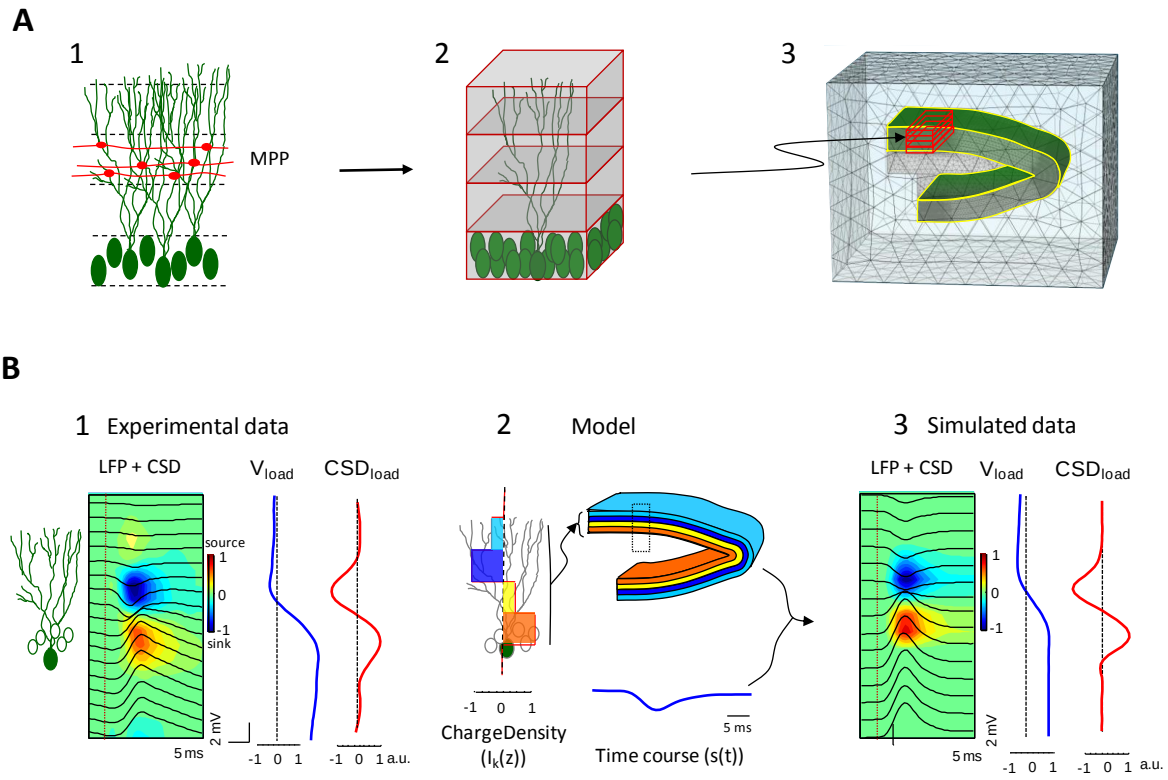

Figure 2.5: ***A****:* The gross cytoarchitecture of the granule cell (GC) population (**1**) was assembled as four stacked rectangular blocks each representing a subcellular domain. (**2**) The blocks were given appropriate curvature and dimensions to reproduce a stereotyped U-shaped geometry of the dorsal dentate gyrus (DG). A tetrahedron adaptive recording mesh simulating the conductive extracellular medium was built in and around the cellular component and was large enough not to distort electrical fields. ***B****:* The block sources were activated using real time activations. In this example we used the excitatory medial perforant pathway (MPP) that makes synaptic contact in the middle third of the dendritic tree (see ***A1***). Total charge was balanced across all blocks at every instant. Charge was distributed throughout all four compartments according to weights obtained in the spatial map of CSD analysis for the electrical activation of this pathway. V_{load} and CSD_{load} represent the spatial weights of voltage and CSD along the GC main axis. The excitatory sink (in blue) is surrounded by a strong passive source (warm colors) in cell soma and a weaker source in distal dendrites. (**2**) At all times, the blocks received proportional charge density with predefined polarity and identical time course. (**3**) Example of FEM simulated data. Modified from Fernández-Ruiz et al., 2013.

We applied Dirichlet boundary conditions by setting the field to the ground value on the external surface of the enclosing volume and imposing charge conservation inside the total volume. A tetrahedral adaptive grid of the highest resolution (smallest size, 0.05 μm) was used to ensure the correct resolution of field equations in the curved compartments (Figure 2.5*A3*).

The FEM approach is widely used in magnetoencephalography and scalp electroencephalography (Chen and Mogul, 2009; Salvador et al., 2011; Thielscher et al., 2011), although to the best of our knowledge it has not previously been used in the study of LFPs. We used a commercial FEM software tool, COMSOL Multiphysics® (www.comsol.com).

Time-dependent analyses were performed using the AC/DC module of COMSOL for all nodes in the extracellular and cellular volume. The spatial and temporal dynamics of LFP and CSD distributions were evaluated after activation of individual subcellular domains by different inputs (the rationale of the performed simulations is illustrated in Figure 2.5*B*). The temporal activation of a particular synaptic afference, such as the MPP excitatory input, was taken as the input signal, $s(t)$. For simplicity, we represent here an MPP-evoked fEPSP. The axons of this pathway establish synaptic contact with GCs in the middle third of their dendritic tree (Figure 2.5*B1*, green axons). The spatial distribution of the CSD corresponding to this activation (Figure 2.5*B1*, contour map) was compartmentalized into four spatial blocks that jointly configured the GC population, such that they roughly reproduced the same spatial profile (Figure 2.5*B2*). The sum of charge densities was set to zero, as imposed by current conservation law. The electric fields and potentials elicited by these currents were calculated for the entire tissue volume by FEM.

Linear profiles of simulated LFPs comparable to those recorded *in vivo* were built using several linear tracks along the vertical *z*-axis, which contained up to 40 registration points spaced at 50 μm intervals and that were placed in the middle of the structure to produce the most homogenous field contribution. LFP profiles were constructed from the instantaneous voltage signal recorded at each simulated recording point.

3. Results

3.1. Current sources of hippocampal LFPs

One of the ultimate goals of the investigations on neural circuit dynamics is to understand the input-output transformation of neuronal signals, i.e., how neuronal activity in an upstream region affects the firing rate and spike timing in neurons of a downstream region. Unfortunately, studying LFP signals recorded from a single or few sites as they are most commonly recorded, cannot properly address the problem of input-output transformation because the LFP signal recorded at any given site represents a weighted sum of multiple neuronal sources in unknown proportions (Buzsaki et al., 2012; Logothetis, 2008; Einevoll et al., 2013). Ideally, one would like to decompose this macroscopic signal into its individual sources and relate them to the output spiking of neurons to reveal the relative influence of the individual inputs to spike outputs during different behaviors.

Information extracted from LFP signals can be improved significantly by monitoring multiple sites at high spatial resolution (Csicsvari et al., 2003; de Cheveigné et al., 2013). Since afferents to dendrites in the hippocampus are spatially segregated, their behavior-dependent contributions can be separated by sufficiently high density sampling of the LFP (Buzsaki et al., 1986; Brankack et al., 1993; Montgomery et al. 2009; Fernández-Ruiz and Herreras; 2013).

In the first part of the present work I characterize the main current sources of hippocampal LFPs. For this purpose, LFP recordings were performed with high-density silicone linear probes (either single-shank or 8 shanks probes with 32 electrodes spaced 50 μm; Figure 3.1.1A) covering the full transversal axis of the hippocampus of behaving rats. Such probes allow us to record LFPs and unit activity in all hippocampal layers and subregions. The electrodes were slowly advanced during the days following the implantation until reaching the final position spanning from the CA1 stratum oriens to the DG lower blade or CA3 str. oriens. Once finalized the experiment the position of the electrodes was histologically verified and compared with the electrophysiological data (Figure3.1B).

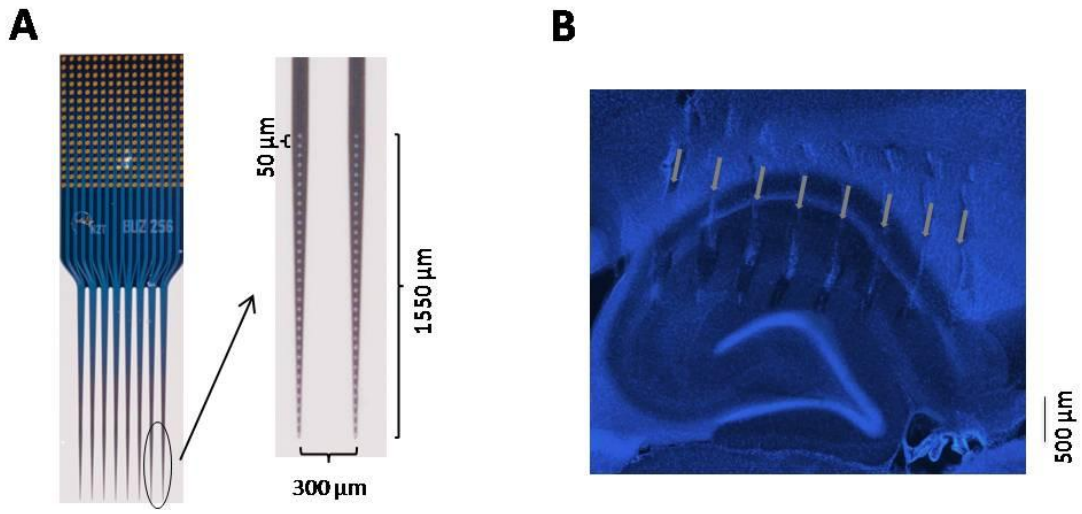

Figure 3.1: **A:** Silicon probe employed for hippocampal recordings (Neuronexus). It has 8 shanks separated 300 µm each with 32 electrodes spaced 50 µm. Thus it covers 1550 µm in depth and 2100 µm in extension. B: Final position of the probe was verified histologically after perfusion of the animal. Transversal section of the dorsal hippocampus stained with DAPI. Modified from Schomburg, Fernández-Ruiz et al., 2014.

3.1.1. Experimental investigation

3.1.1.1. CA1 region

Linear recordings along the vertical axis of the hippocampus clearly show the characteristic laminar variations of LFPs (Figure 3.2A). The hippocampus, and specially the CA1 region, has a great advantage for the study of LFPs due to the parallel arrangement of their cells and the stratification of the synaptic inputs. This anatomical organization results in layer-specific LFP patterns elicited by the inputs innervating the pyramidal or granular cells in restricted dendritic domains (Montgomery et al., 2009; Brankack et al., 1993; Bragin et al., 1995a,b; Fernández Ruiz et al., 2012; Benito, Fernández-Ruiz et al., 2014).

ICA discriminates the contributing sources to the LFP based on their distinct spatial distribution. When applied to the multi-electrode wide-band LFP signals of the CA1 region, ICA found three major pathway-specific independent-components (ICs). By convoluting the LFP with the inverse of the mixing matrix estimated by ICA we get the relative voltage weight of every IC in each electrode. Projecting those weights to the anatomical space (i.e. the spatial

arrangement of the electrodes in the tissue) we obtain the spatial voltage loading in the dorsoventral axis (z) of each IC (Figure 3.2B). The second derivative in the z-axis of those voltage loadings represents the CSD loading of this particular IC (Figure 3.2C), that is the transmembrane currents elicited by this particular input in the target population.

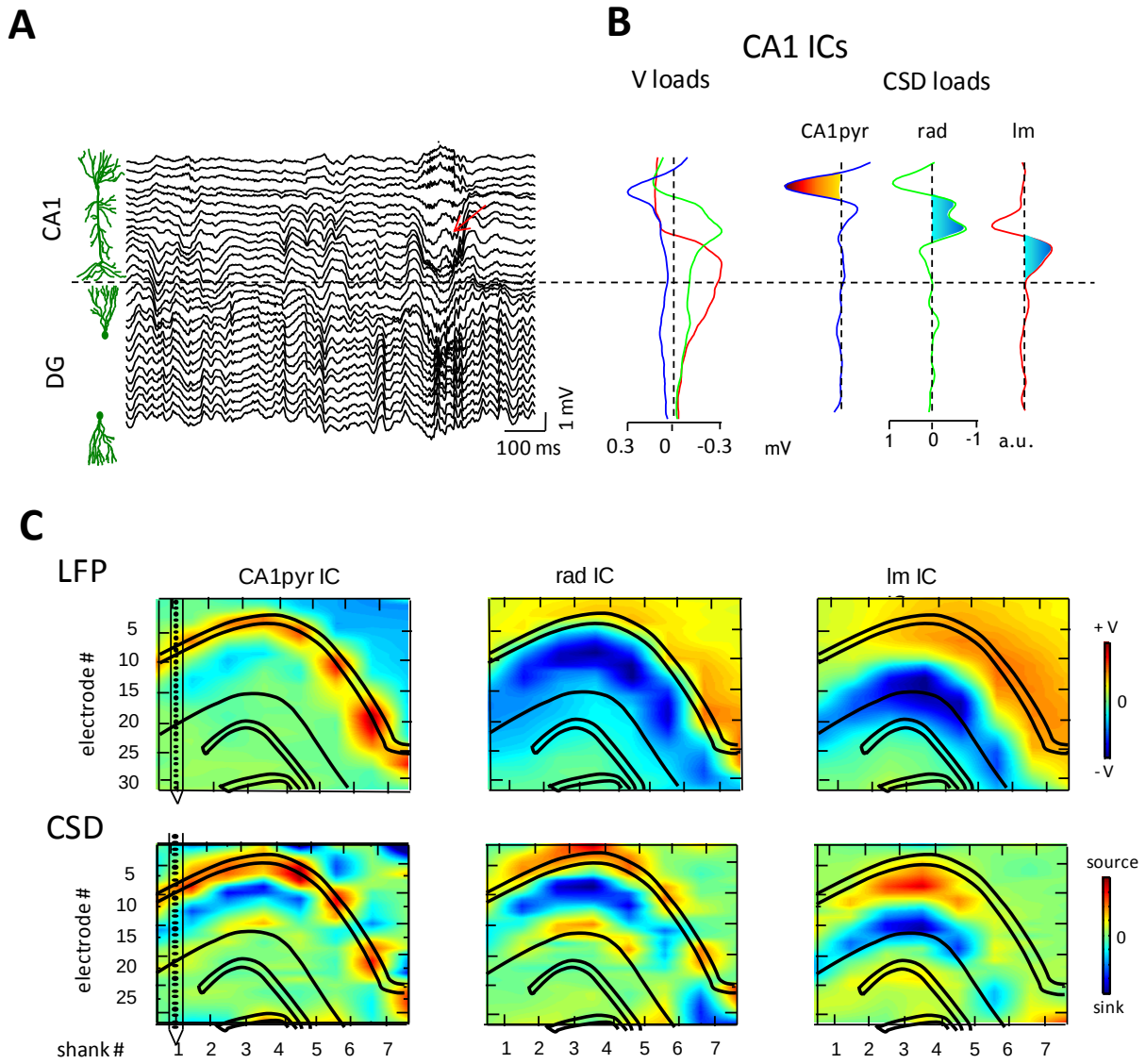

Figure 3.2: **A:** LFP profile along CA1 and DG displaying some characteristic CA1 LFP patterns, sharp wave ripples (red arrow).**B:** Three main ICs were found for CA1 LFPs with largest voltage and active currents at different layers: the pyramidal layer (*CA1pyr*), str. radiatum (*rad*) and str. lacunosum-moleculare (*lm*). **C:** 2D voltage and CSD distributions for the 3 ICs highlight their layer-specific distributions. Modified from Schomburg, Fernández-Ruiz et al., 2014.

The maximal amplitude of the first component (*rad*) is at the level of the str. radiatum and its CSD depth profile matched the source–sink–source distribution of the spontaneously occurring sharp-waves during immobility (Figure 3.2A-B green traces; Bragin et al., 1995; Montgomery and Buzsáki, 2007; Fernández-Ruiz et al., 2012), corresponding to the apical dendritic excitation of CA1 pyramidal neurons (manifested as a strong sink in the str. radiatum) by the synchronous CA3 output (Buzsáki et al., 1983). Another IC (*lm*) peaked below the first component, corresponding to the str. lacunosum-moleculare-related current sink (Figure 3.2A-B red traces; Brankack et al., 1993; Benito et al., 2013). The peak amplitude of the third component (*CA1pyr*) occurred at the depth of CA1 pyramidal layer (Figure 3.2A-B; blue traces), also identified by the large amplitude ripples and unit firing (Mizuseki et al., 2011). This IC is characterized by a prominent current source centered at the pyramidal layer.

The above results were obtained by applying ICA to single-shank recordings but I also applied it to the 2D matrix of 256 electrode arrays (8 shanks separated 300 μm). By doing so the same 3 main ICs were obtained in the CA1 region. When plotted in two dimensions they display clear layer-specific distributions (Figure 3.2 C). The *CA1pyr* IC shows larger positive voltage along the CA1 pyramidal layer and the CSD map reveal a source surrounded by smaller sinks. This distribution matches the expected from a perisomatic inhibition and its passive return currents in apical and basal dendrites. The *radiatum* component displays larger negative voltage along the CA1 str. radiatum and a polarity reversal in the pyramidal layer. The CSD map reveals the expected strong sink in the dendritic domain of the Schaffer collaterals (CA3 to ipsilateral CA1 input) flanked by sources in the str. lacunosum-moleculare and pyramidal layer. The *lac-mol* IC has larger negative voltage around the hippocampal fissure (the separation between CA1 and DG) but the CSD analysis reveals a current dipole restricted to CA1 distal dendrites, the dendritic domain of the axon terminal from entorhinal cortex layer 3.

Voltage and CSD spatial distribution were constant for all the animals (n = 7) and behavioral states, indicating that they are reflecting the underlying anatomy of inputs to the CA1 regions. The combination of CSD analysis and ICA decomposition of LFPs is revealed as a useful tool to precisely identify the different hippocampal layers and more importantly to separate and identify the current sources of the LFP. However this would require more extensive

analysis so the next step was to build a model of the rat hippocampus to get a better understanding of the relations between source geometry and voltage distribution in the structure.

The present results in freely moving animals confirm and extend our previous work in anesthetized rats (Fernández-Ruiz et al., 2012a,b; Benito, Fernández-Ruiz et al., 2014). In the next paragraphs it follows a brief summary of previous experimental findings closely related to what has been presented in this section.

In the urethane-anesthetized preparation the *radiatum* and *lm* components were also the main contributors to CA1 LFPs, however the CA1pyr showed significantly less relative power than in the awake animal. This can be explained by a reduced firing rate of CA1 perisomatic-targeting interneurons under urethane (Ylinen et al., 1995; Klausberger and Somogy, 2008). With local pharmacological manipulations we demonstrated that the radiatum component activity was selectively decreased by non-NMDA glutamate blockers (DNQX). Targeted blockade of the ipsilateral CA3 with lidocaine injections also selectively decreased *radiatum* IC power. Those tests confirmed that the synaptic glutamate currents evoked by the input of the Schaffer collateral pathway from CA3 to the str. radiatum dendrites of the CA1 pyramidal cells were the underlying cause of the LFP activity captured by the *radiatum* IC. For this reason we also termed it as *Schaffer* component. Pharmacological manipulations rendered less clear results for the *lm* component. As well as the *radiatum* IC, *lm* component activity was impaired by local injection of DNQX, indicating its glutamatergic nature. However it was also affected by GABAa blockers (bicuculline) pointing towards a contribution from inhibitory currents. This can be explained by the activity of several types of interneurons, which target the CA1 pyramidal cell dendrites at the str. lacunosum-moleculare, including oriens-lacunosum and neurogliaform cells; most of them are strongly feedforward activated by the entorhinal layer 3 axons (Klausberger and Somogy, 2008; Leao et al., 2012; Lasztóczi and Klausberger; Basu et al., 2013).

To go beyond a mere characterization of the main sources of CA1 LFPs and to show the usefulness of studying pathway-specific LFP components instead of the original mixed LFP signal, these previous works focused on the analysis of the temporal dynamics of the *radiatum* component and its relation with CA1 and CA3 units. The low firing rate and functional

clustering of CA3 pyramidal cells allowed us discriminating elementary synaptic events in the *radiatum* IC, which were termed as micro-field excitatory postsynaptic potentials (µ-fEPSPs; Fernández-Ruiz et al., 2012). *Radiatum* IC activity shows an ordered succession of µ-fEPSPs that appear to be generated by functional clusters of CA3 pyramidal neurons, to which individual units are recruited variably. Such pattern implies a hierarchical internal operation of the CA3 region based on sequential activation of pyramidal cell assemblies. A fraction of these excitatory packets readily induce firing of CA1 pyramids and interneurons, the so-called Schaffer-driven spikes, revealing the synaptic origin in the output code of single units. This finding supports the postulate that synchronous activity in cell assemblies is a network language for internal neural representation (Buzsáki, 2010; Harris, 2005).

In a subsequent work (Fernández-Ruiz et al., 2012b), we assessed the plastic changes underwent in the CA3-CA1 pathway spontaneous activity following long-term potentiation (LTP) and determined how pairs of pre- and postsynaptic neurons modify spike transfer compared to the population. We found that the ongoing *radiatum* IC activity and the share of postsynaptic spikes fired by Schaffer input specifically in CA1 units increases after LTP without significant change of the mean firing rate. A re-organization of the presynaptic cell assemblies synchronously firing to elicit CA1 spikes was also found. Thus the results provided first time evidence for pathway-specific ongoing plasticity and its impact over spontaneous network activity consisting on the increased spike transfer between nuclei connected by specific potentiated channels. This constitutes provides evidence that LTP induction produces a pathway-specific enhancement of ongoing activity that is effectively propagated to subsequent relays of the network. These observations complement and extend on classic LTP properties observed with evoked stimuli by showing their ongoing correlates and supports the view of synfire chains (Abeles, 1991) as a prominent mechanism for information transfer in neural networks.

3.1.1.2. Dentate Gyrus

Despite the fact that LFPs in dentate gyrus have been much less intensively researched than in the CA1 region, it has been know for long time that this structure exhibits a rich variety of LFP patterns and oscillations, including theta and gamma rhythms (Bragin et al, 1995a),

dentate spikes (Bragin et al, 1995b), slow oscillations (Isomura et al., 2006) and odor-evoked beta oscillations (Heale et al., 1994). However, due to the complexity of its local circuits and the scarce knowledge regarding the synaptic inputs and firing properties of its different cell types during behavior, the mechanisms of generation of the different LFP patters observed in the DG remain largely unknown. It has been shown that DG theta and gamma oscillations are strongly modulated during exploratory and learning behavior in rodents (Givens, 1996; Skaggs et al., 2006; Csicsvari et al., 2003; Montgomery et al., 2009), pointing towards an important function of these rhythms in cognitive functions involving this structure. DG oscillatory dynamics also has a strong impact on its main target region, CA3, (Mori et al., 2004; Akam et al., 2012; Neunuebel and Knierim, 2014) and the computations performed in the whole hippocampal circuit (Montgomery et al., 2009; Sullivan et al., 2013).

There are two main extrinsic afferences to the DG, the medial (MPP) and the lateral (LPP) perforant paths originating in layer 2 of medial and lateral entorhinal cortex and innervating the distal and middle thirds of granular cell (GC) dendrites. So is to be expected that these two inputs are major contributors to DG LFPs. However there are many others inputs that can also contribute substantially. On one hand the associational-commissural fibers innervate the inner third of GC dendrites and on the other the multitude of GC layer and hilar interneurons innervate the soma and dendritic regions of the GCs.

Following the same procedure as that previously described for the CA1 LFPs we identify three main ICs in the DG. The three ICs have similar voltage loadings, with a plateau-like maximum between cell layers throughout the hilus, which declined outwardly and reversed its polarity at different points, and characteristics points for each of them (Figure 3.3B). The CSD loading shows more differences between ICs.

The first IC (*LPP,* Figure 3.3B; blue traces) is the one that reverses its polarity more superficially (closer to the fissure) and has a sink in the superficial GC dendrites and a source closer to their soma. This current distribution is similar to that obtained in the DG for evoked potentials stimulating the LPP (Leung et al., 1995; Benito, Fernández-Ruiz et al., 2014). The second component (*MPP,* Figure 3.1.3B; red traces) has a reversal point around 100 μm below the LPP and a sink in the middle third of the GC dendrites surrounded by two smaller sources at the distal dendrites and GC soma. This current distribution is similar to that obtained in the DG

for evoked potentials stimulating the MPP (Leung et al., 1995; Benito, Fernández-Ruiz et al., 2014). The third IC (*GCsom*, Figure 3.3B; green traces) has a source at the GC soma and a sink in the middle of the dendritic region and its voltage loading reverse at a similar depth than the *MPP* IC. This current distribution could be produced by a perisomatic inhibition, as it is the case of the dentate basket cells (Han et al., 1993; Houser, 2007).

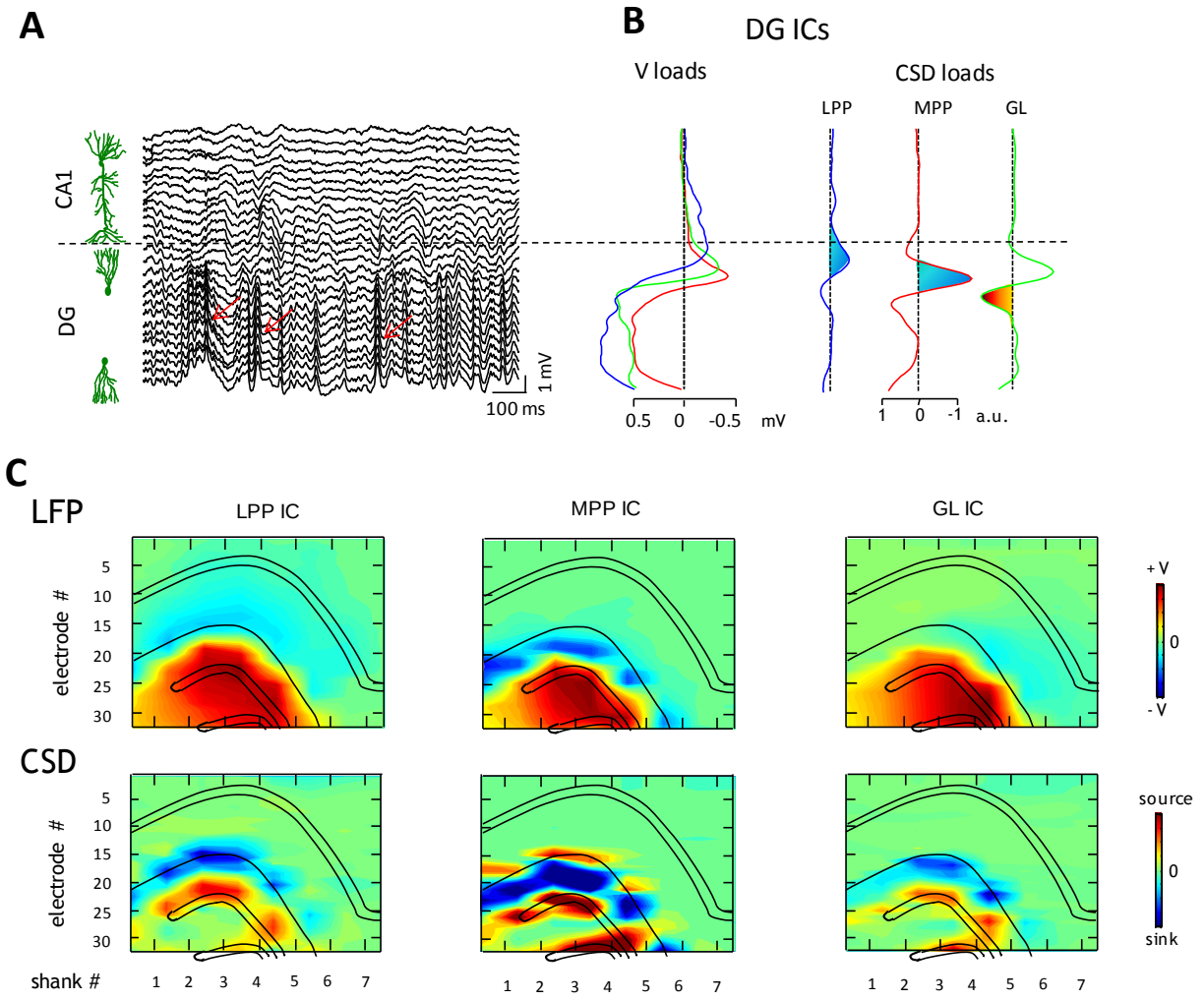

Figure 3.3: **A:** Similar LFP profile as illustrated in Figure 3.1.2 but featuring a characteristic DG LFP pattern, dentate spikes (red arrow). **B:** Three main ICs were found for DG LFPs. All of them display large positive voltage across the hilus but reverse polarity at different depths in the str. moleculare. Largest currents were restricted to the outer third of the str. moleculare (*LPP*), middle third (*MPP*) and GC layer (*GCsom*). **C:** 2D voltage distributions for the 3 ICs were dominated for the positive hilar potentials but the CSD maps illustrated their different laminar specificity.

The 2D plots for the three components further illustrate their characteristic spatial distributions. The voltage maps of the three of them are characterized by strong positive voltage in the hilus that decay toward the GC dendrites. In the three cases it reverts in the str. moleculare but only the *MPP* shows strong and localized negative voltage. This can be explained because the dipolar configuration of both *LPP* and *GCsom* favors a passive decay of the negative voltage gradient while the quadrupolar configuration of the *MPP* favors a more closed negative field. This is similar to what happened with the *radiatum* IC in CA1 which has also a quadrupolar configuration in contrast to the CA1 *lm* IC which has a dipolar one (Figure 3.2B,C).

The 2D CSD maps confirm the distal sink and inner dendritic source of the *LPP* IC, the source-sink-source configuration of the *MPP* and the dendritic sink- somatic source of the *GCsom* (Figure 3.3C). It is important to note the lack of any currents for the three components in the hilus. That is to be expected as the axon is the only GC element in this region and it drains only a negligible amount of current.

As was also the case for the CA1 LFP ICs, the present results for the DG LFPs confirm and extend our previous results in urethane-anesthetized rats (Fernández-Ruiz et al., 2013; Benito, Fernández-Ruiz et al., 2014). In those previous works we showed with local pharmacological manipulations that the activity of the *MPP* and *LPP* components was selectively decreased with the injection of DNQX (a non-NMDA glutamate blocker). On the contrary, the *GCsom* component was affected by both glutamate and GABAa (bicuculline) blockers. This result can be explained by two mechanisms. Either the activity captured by the *GCsom* component is contributed by excitatory and inhibitory currents onto the perisomatic region of the GC or it is only elicited by inhibitory currents delivered by interneurons relaying for its activation on excitatory inputs. The lack of somatic excitatory inputs leads us to think in the second alternative as the most plausible.

Another test for the pathway-specificity of the LFP ICs was achieved in those previous works by the electrical stimulation of afferent pathways to the hippocampus (Fernández-Ruiz et al., 2012a; Fernández-Ruiz et al., 2013; Benito, Fernández-Ruiz et al., 2014). When subthreshold stimuli (not strong enough to evoked a population spike, i.e. the synchronous discharge of action

potentials in the target population) were delivered to the medial and lateral perforant paths and the Schaffer collaterals, a field EPSP (fEPSP) was recorded in the DG and CA1 respectively, indicating synchronous excitatory synaptic currents onto the target populations of cells (Leung, 1979; Leung et al., 1995). After ICA decomposition of the LFPs, those fEPSPs were selectively captured by the *MPP*, *LPP* and *radiatum* components selectively. This result confirms that the currents elicited by both the spontaneous and evoked activity of those pathways are selectively captured by specific ICs. Thus ICA decomposition of hippocampal LFPs allows the separation and identification of pathway-specific contributors to the LFPs (Fernández-Ruiz and Herreras, 2013).

3.1.1.3. Characterization of hippocampal LFP sources

The temporal and spectral dynamics of the LFP ICs during different behavioral states contain a large amount of information about the computations performed by the hippocampal circuits (Schomburg, Fernández-Ruiz et al., 2014). Although I will extend on this aspect in the last section of the Results, some gross quantifications of the ICs activity are provided in Figure 3.4.

To quantify the contribution of each IC to the recorded LFPs we calculated the relative variance of the LFP matrix that is accounted by each IC. The results in figure 3.1.4A were obtained pooling together all the ICs extracted during sleep and behavior in all the recording shanks that cover both CA1 and DG regions in 7 animals. The 6 main ICs reported here usually account for more than 95% of the total variance of the LFPs in the selected recording tracks, once the noise and artifactual activity was removed (see Section 3.1.3). The remaining variance was explained by other sources with very small contribution to the LFP.

The IC with largest variance was the *LPP*, followed by the *lm* and *MPP* components. Together the three DG ICs have more variance that the three CA1 ICs, as is expected due to fact that DG LFPs are in general larger that CA1 LFPs (Fernández-Ruiz et al., 2013). In the second chapter of the Results I will analyze the biophysical factors that explain this phenomenon. The IC with lower variance was the *CA1pyr*, what can be explained by having its current restricted to somatic region. An important factor determining the contribution of the different current sources

to the LFPs is their dipolar moments. Sources with a larger dipolar moment, as the *lm* and *LPP*, which have the geometrical configuration of a linear dipole are expected to produce larger fields (Nunez et al., 2006; Plomsey, 1993). On the contrary, sources like *rad*, *CA1pyr* or *MPP* ICs have the geometry of a linear quadrupole, thus a shorter dipolar moment, and are expected to produce closer fields and contribute less to the LFPs.

In Figure 3.4B averaged power spectrums of the 6 ICs corresponding to times while rats are sleeping in his home cage (red traces) or awake performing different navigational tasks (blue traces) are compared. Although each IC has different spectral dynamics the averaged spectrums during behavior are dominated by the ubiquitous presence of the theta rhythm (note the peak around 8 Hz). The spectral theta peak is more prominent in the *lm* component, as corresponds to the largest theta dipole being located in the str. lacunosum-moleculare (Branckack et al., 1993; Buzsáki, 2002). During sleep there are two differentiated stages, the slow-wave sleep characterized by 1-2Hz oscillations, and the rapid-eye movement sleep, characterized by theta oscillations of slightly lower frequency than those present during locomotion. Both oscillations are visible with different relative power in the spectrums of the 6 ICs.

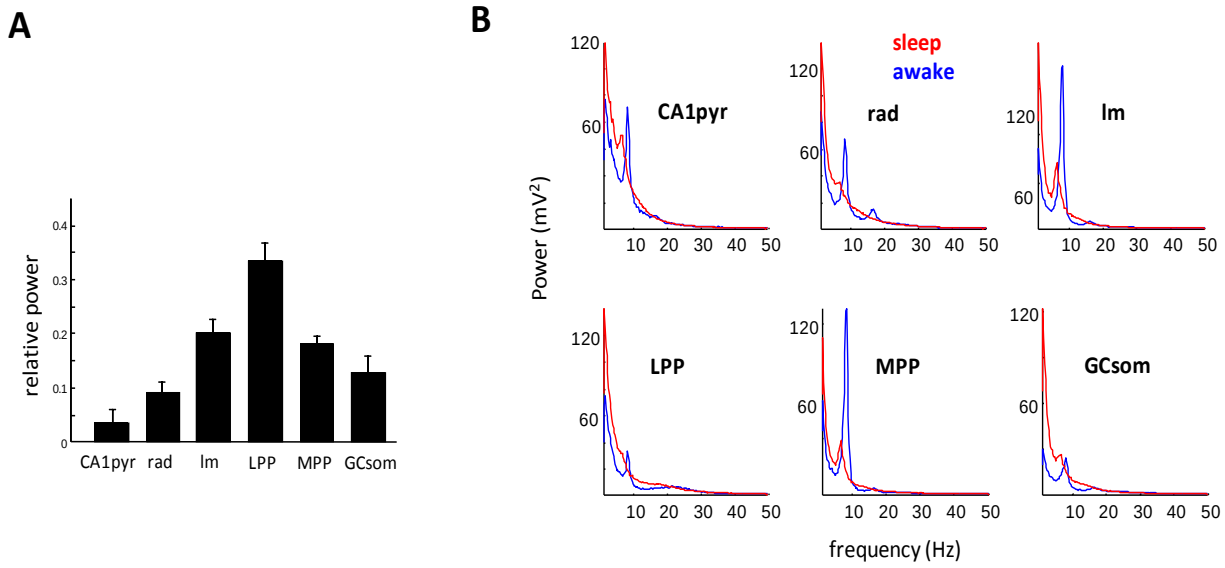

Figure 3.4: **A:** Relative power for the six main hippocampal LFP ICs averaged across shanks, sessions and animals (n = 7 animals). **B:** Power spectrum of the 6 ICs for periods where animals were sleeping in their home cages (red) or performing different navigational tasks (blue). Data averaged across shanks, sessions and animals (n = 7 animals).

In this section we have shown that the application of ICA to large-scale recordings of hippocampal LFPs is able to disentangle their underlying synaptic sources. We found three main sources of CA1 and DG LFPs respectively. Each of them was characterized by a restricted laminar distribution of currents that allows their matching with the known synaptic domain of main extrinsic and intrinsic inputs to the CA1 pyramidal cells and DG granular cells populations. In addition those sources display different spectral characteristics. This suggests the possibility that the study of their spectro-temporal dynamics would be informative to understand the computations performed by the hippocampal circuits during behavior. This will be extensively explored in following sections.

3.1.2. Finite Elements simulations of LFP's

The combination of ICA and CSD analysis allowed us to solve the inverse problem of the LFPs; that is, given the recorded LFPs, separate and identify their underlying current sources. As a test of the accuracy of the above results we sought to use the extracted LFP sources to solve the forward problem of the LFPs, i.e. to reproduce the original LFP distribution. For this purpose we built a 3D model of the dorsal hippocampus of the rat with FEM (see Methods).

The model simulates a transversal lamella of the dorsal hippocampus similar to that were the recording electrode was placed in all the animals (Figure 3.1B). This lamella was extended 4 mm in depth to simulate a whole block of the dorsal hippocampus. All the simulated recordings were performed in the middle of the structure to minimize any possible border effect.

In the model each hippocampal layer was represented as a polygonal block. Thus, the cellular and dendritic portions were represented as stacked longitudinal blocks of current sources, each representing a subcellular "population" domain that when activated act as laminar dipoles. In preliminary simulations we found that eighth of these blocks with 100 μm thickness in the case of CA1 and four 60 μm thickness blocks for each blade of the DG were sufficient to reproduce the main laminar features of hippocampal LFPs. To implement the exact geometry of the current sources of the LFP, average CSD loadings from each LFPs ICs were discretized into eight or four point curves that were used as weights to implement the sources in CA1 and DG region of the model (see Methods).

In the first set of simulations we implement in the model the three main sources of CA1 and DG LFPs that were identified in the previous section in isolation. We took 100s of activity from the six main ICs extracted while the rat was resting in the home cage, and use them as inputs to the whole CA1 or DG regions, that were assumed to be simultaneously and homogeneously active.

LFPs were sampled in a linear track in the middle of the hippocampus, approximately perpendicular to the cellular layers (Figure 3.5A and 3.6A). After the independent activation of each source, the averaged voltage power along this line was calculated and used to construct voltage loading curves for each IC and its second derivative to construct CSD loading curves (Figures 3.5B and 3.6B).

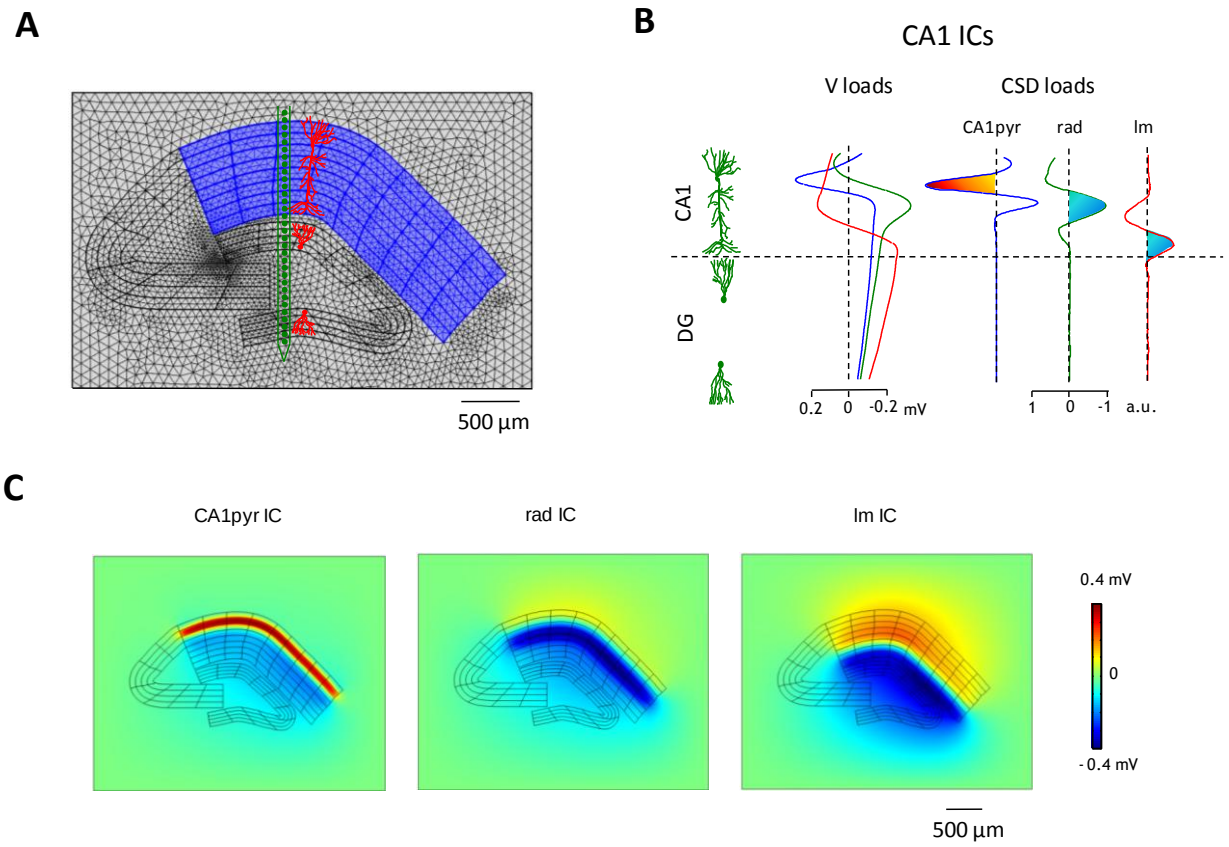

Figure 3.5: **A:** FEM model of the rat dorsal hippocampus highlighting the CA1 region (blue). **B:** Voltage and CSD loadings along a vertical profile spanning CA1 and DG (indicated by the position of the green linear probe in A) illustrating the simulated CA1 LFP sources (note their similarity with the experimentally obtained ICs in Figure 3.1.2B). **C:** Averaged 2D voltage distributions obtained with the activation of the 3 CA1 LFP sources illustrate their layer-specific distribution.

For CA1 LFP ICs, voltage and CSD loadings obtained from the activation of the three sources were remarkably similar to those obtained experimentally (compare Figure 3.3B and Figure 3.2B).The*CA1pyr* component displays a sharp peak in its voltage loading at the pyramidal layer and the corresponding source surrounded by two sinks in the CSD loading (Figure 3.5B, blue traces). The largest amplitude of the *rad* IC is at the level of the str. radiatum, around 200 μm below the pyramidal layer, and for the *lm* IC at the str. lacunosum-moleculare, around 500 μm below the pyramidal layer. The *rad* component CSD loading has a larger sink flanked by two smaller sources while the lm displays a rather symmetrical current dipole (Figure 3.5B, red and green traces).

The model also allows us to calculate the voltage distribution in the whole hippocampus and surrounding extracellular space. We took a 2D plane parallel to the transversal axis of the hippocampus situated in the middle of the structure and plot the voltage distribution resulting from the activation of the three sources independently (Figure 3.3C). The 2D maps obtained were highly similar to the pseudo 2D voltage maps constructed from the voltage loadings of the ICs obtained experimentally (compare Figure 3.5C and Figure 3.2B). In the three cases the laminar distribution of the three ICs matches with the corresponding CA1 sublayers.

Current source 2D maps were omitted due to the fact that they did not offer any additional information given that this was exactly what was introduced in the model initially.

We repeat the above procedure for the DG ICs. As for the ICs extracted from the recorded LFPs, the three main DG ICs have voltage loadings with large positive amplitudes across the whole hilus which decay beyond the GC layers and reverse at different depths in the str. moleculare (compare Figure 3.6B and Figure 3.3B). The *LPP* component has the most superficial reversal point, as correspond to its sink in the outer third of the str. moleculare (Figure 3.6B, blue traces). The *MPP* IC reverses closer to the GC layer and displays a large sink in the middle of the str. moleculare flanked by two smaller sources (Figure 3.6B, blue traces). The *GCsom* has a voltage and CSD loading with reversal point and source location intermediate between the *LPP* and *MPP* ones.

2D voltage maps for the three DG ICs display also similar features with those constructed from the experimental data (compare Figure 3.6C and Figure 3.3C), in all the cases dominated by

large hilar positive potentials. Note the more restricted negative voltage of the *MPP* ICs compared to the *LPP*; this can be explained by the more "close-field" configuration of the *MPP*, as will be analyzed in the next section. In comparison the *GCsom* IC elicits very small negative fields.

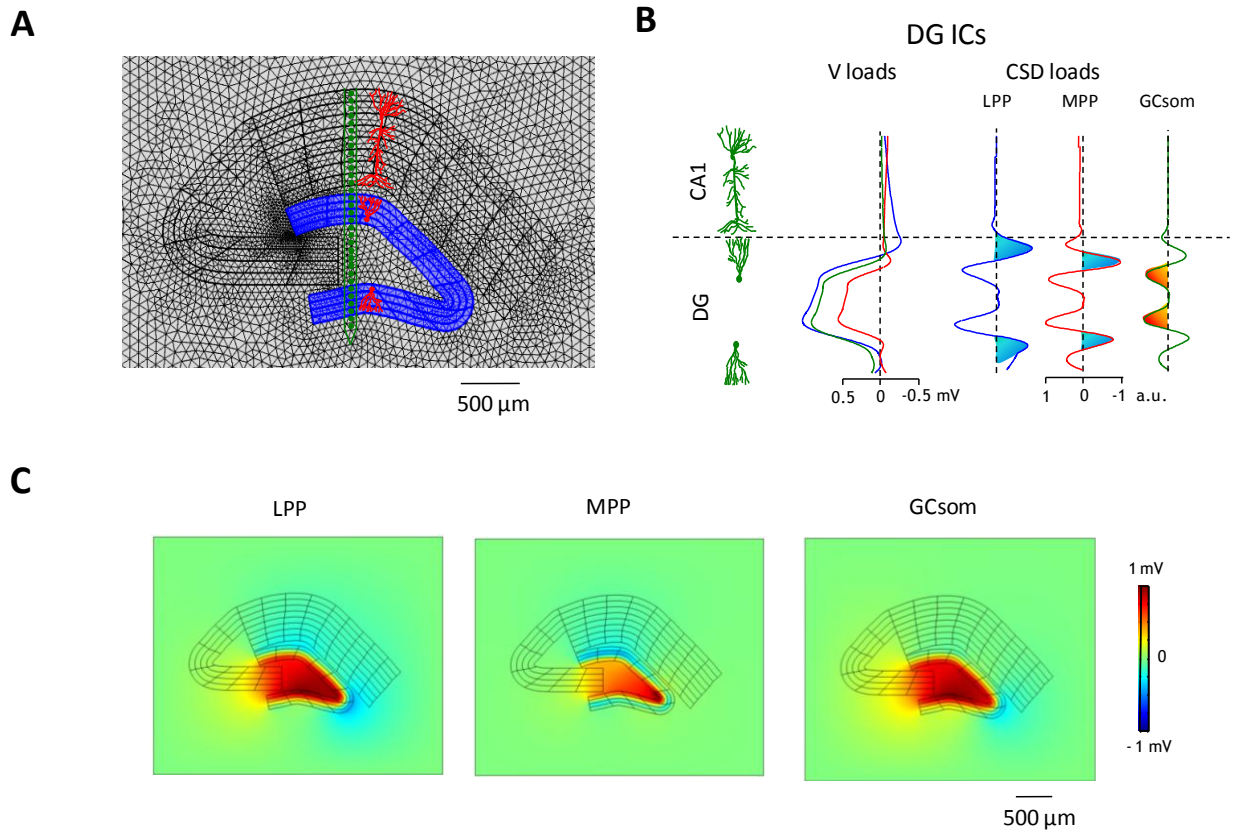

Figure 3.6: **A:** FEM model of the rat dorsal hippocampus highlighting the DG region (blue). **B:** Voltage and CSD loadings along the same vertical profile as in figure 3.1.5 of the three simulated DG LFP sources (note their similarity with the experimentally obtained ICs in Figure 3.1.3B). **C:** Averaged 2D voltage distributions obtained with the activation of the 3 DG LFP sources are dominated by positive hilar potentials but display different location and spread of negative potential in dendritic layers.

The above results show that the presented model accurately reproduces the voltage distributions experimentally obtained for the six main current sources of CA1 and DG LFPs. However a question remains about if those sources when activated simultaneously with similar dynamics as those observed in the experiments reproduce the observed profile of LFPs. To

answer this question we performed another set of simulations in which the six sources were activated simultaneously.

We performed these simulations feeding the model with the ICs time series extracted in either during sleep or during running activity. By doing this we sought to reproduce in the model the two main hippocampal LFP patterns: theta oscillations and sharp-wave ripples, SWR (see Introduction). To sample LFPs a recording linear probe with electrodes spaced 50 μm was simulated in the middle of the hippocampus, spanning the CA1 and DG regions.

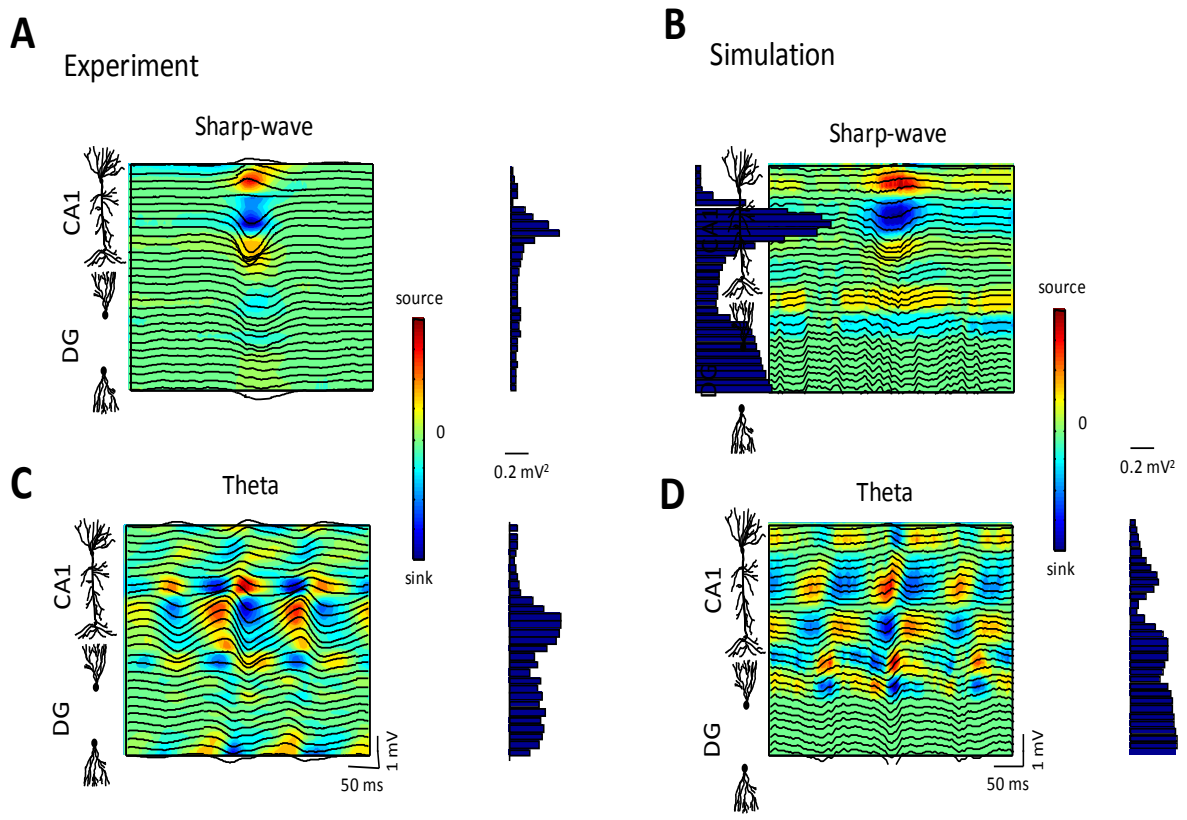

Figure 3.7: **A:** Averaged LFP profile of sharp-wave ripples show a large negative LFP deflection at str. radiatum and the corresponding dominating power at that layer (histogram). The CSD map illustrates the characteristic source-sink-source distribution for the excitatory Schaffer input to the CA1 pyramidal cells dendrites. **B:** LFP, CSD and power profiles were constructed in the same way for simulated SWR and display similar laminar profile as the experimental ones. C: Averaged LFP and CSD profile for theta oscillation during running. Largest currents and LFP power were present in the str. lacunosum-moleculare but phase shifted sink and sources also appear at str. radiatum and DG str. moleculare. **D:** Simultaneous activation of the 6 hippocampal LFP sources presented in this section with temporal activations extracted from experimental recordings during running result in a similar laminar potential and CSD distribution.

SWR are characterized by a large negative LFP wave, and the corresponding sink, at the CA1 str. radiatum which reverse at the pyramidal layer, and it is accompanied by sources at the pyramidal layer and str. lacunosum-moleculare (Figure 3.7A). This activity is caused by a synchronous input of CA3 pyramidal cells to CA1 eliciting a large depolarization of str. radiatum dendrites accompanied by their return passive currents (Bragin et al., 1995; Fernández-Ruiz et al., 2012). The averaged power along the CA1-DG during SWR is dominated by a large increase at the str. radiatum (Figure 3.7A, histogram). In the simulated LFPs all the main characteristics of the LFP and CSD profiles of SWR were replicated, remarkably the large negative LFP amplitude at the str. radiatum and the characteristic source-sink-source current distribution (Figure 3.7B).

The CSD map of theta oscillation is more complex that the one obtained for SWR because in the former case is not only one pathway (i.e. source) which is dominating but the simultaneous activity of several, if not all, of them (Brackack et al., 1993; Buzsáki, 2002). The largest theta currents and fields are present at the str. lacunosum-moleculare but they are accompanied by shifted sink/sources at the str. radiatum and str. moleculare of the DG and with lower intensity in str. pyramidale and oriens (Figure 3.7C). Along the depth profile theta waves gradually shift their polarity displaying a 180° reversal between pyramidal layer and str. lacunosum-moleculare. Both the LFP and CSD profile characteristics of theta oscillations were replicated in our simulations.

With the above simulations we were able to prove that our model accurately reproduces the laminar characteristics of hippocampal LFPs. This confirms that the six current sources identified with ICA are sufficient to account for the main LFP patterns observed in the hippocampus. Having settled the fundamental basis of our analytical approach, in the next sections we will employ the FEM hippocampal model and the ICA + CSD decomposition of LFPs to investigate the biophysical and physiological mechanisms of LFP generation in the hippocampus as a tool to interpret the underlying activity of neural circuits.

3.2. Biophysical factors shaping the generation of LFPs in the DG

As a step forward in the present study we decided to employ the model presented in the previous section to analyze the generation of LFPs in the DG. We chose to focus on this particular hippocampal region because it has been far less studied than the CA1 or CA3 and despite the fact that large oscillation can be observed in the DG during behavior their generating mechanisms are largely unknown.

The amplitude and phase of LFPs in a given brain structure is influenced by spatial factors such as cell morphology, synaptic arrangement and geometrical configuration of cellular layers (Kajikawa and Schroeder, 2011; Ho et al., 2012; Buzsáki et al., 2012). Although some of these factors have been extensively studied in single cell models (Einevoll et al., 2013; Schomburg et al., 2014; Linden et al., 2011), others, notably those referring to the macroscopic geometry of the cellular populations, have been mostly neglected, in part due to the difficulties of modeling those using standard techniques. Here we take advantage of the ability of FEM to explicitly model the tridimensional arrangement of a whole brain structure, i.e. the hippocampal dentate gyrus, to directly address these factors. For the following simulations we employed a reduced version of the hippocampal model reproducing only the dentate gyrus region (see Figure 2.6).

Two assumptions are usually made when interpreting LFPs: (1) the dominant polarity (positive or negative) is determined by the inhibitory or excitatory nature of the synaptic inputs; and (2) the closer the LFP is to the synaptic domain the larger its amplitude. However, several observations in the DG challenge both these assumptions. In this region positively oriented spontaneous LFP events can be observed (Bragin et al., 1995a,b), which are rarely observed in the brain. Moreover, LFP power reaches a maximum in the hilus (i.e., at a distance from the GC layer).

3.2.1. Influence of synaptic domains and cell morphology

In the previous section we described three main synaptic sources of DG LFPs that we identified as the transmembrane currents on the GC elicited by the lateral perforant path input (*LPP*), the medial perforant path (*MPP*), and a perisomatic inhibition (*GCsom*). Despite their

different chemical nature (*MPP* and *LPP* glutamatergic, thus excitatory, and *GCsom* likely gabaergic, thus inhibitory) the three of them were characterized by large positive polarity in the GC layers and hilus and a reversal in the str. moleculare (Figure 3.3). However there are other known inputs to the GCs that apparently do not elicit sizeable contributions to the recorded LFPs. We investigated in the model the amplitude and polarity of DG LFP produced for different types of synaptic inputs, employing the time series of experimentally obtained ICs and variable source configurations (see Methods).

Both dendritic excitation (Figure 3.8A) and somatic inhibition (Figure 3.8B) produced large positive LFPs in the hilus that reverse in the str. moleculare. Inversion of the polarity of current sources, whether simulating distal dendritic inhibition (Figure 3.8C) or somatic excitation (not shown), switched the LFP polarity at all sites. Although negative LFPs in the hilus are also observed experimentally these were far less frequent than positive LFPs, suggesting that anatomical pathways that generate negative hilar LFPs (e.g., dendritic inhibition) do not fulfill the spatiotemporal requirements to contribute to LFPs as strongly as others (see below).

As we showed in Figure 3.4 the IC with larger contribution to DG LFPs was the LPP while the MPP was the smaller. Because the contribution of a given synaptic input to the LFP depends on both geometrical and functional factors, and the latter may differ for excitatory and inhibitory inputs during ongoing activity, we ran simulations using the same temporal activation in all cases. We compared the three experimentally observed source configurations plus two others we did not observed but were predicted by the anatomy (Houser, 2007;Amaral et al., 2007; Han et al., 1993), dendritic inhibition and a proximal commissural-like excitation (see colored GC cartoons in Figure 3.8D). The relative power of LFP elicited by simulated inputs was similar to those observed in the experiments, the differences could be attributed to the different temporal dynamics of the inputs in the latter. The excitatory *MPP* and *LPP* inputs and the inhibitory *GCsom* input elicited positive LFPs across the hilus, whereas distal dendritic inhibition and proximal excitation elicited negative LFPs. However, we noticed that the extension and location of the active synaptic domain produced a clear effect whereby the power was stronger the more distal the input and the narrower the active domain, the stronger the power. This result can be explained by the increase of dipolar moment in these source configurations.

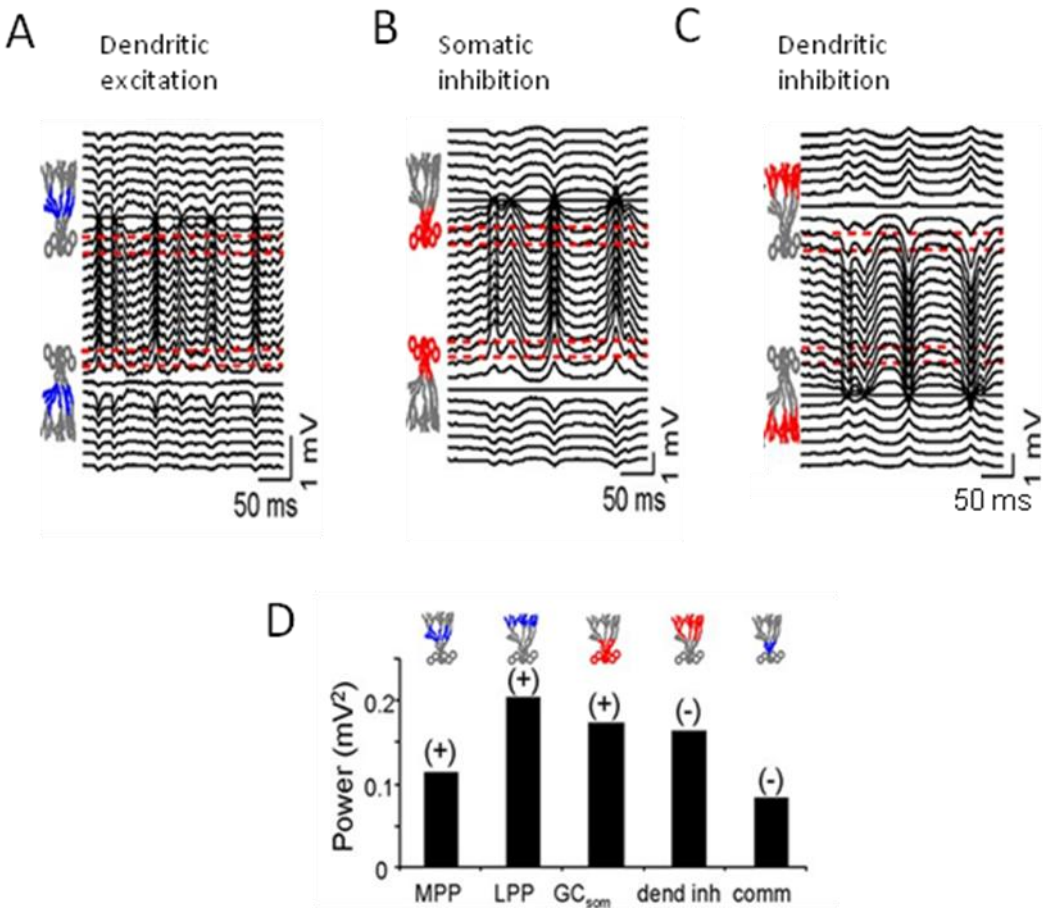

Figure 3.8: **A**: Comparison of LFP elicited by different inputs to the DG. LFPs were obtained using the same temporal activation as those recorded in the experiments. The GC drawing on the left mark the cellular bands used as excitatory (blue) or inhibitory (red) synaptic domains. ***A***, ***B***, sample epochs of dendritic excitatory (*MPP*) and somatic inhibitory (*GCsom*) LFPs. Note the large, steady and positive potentials across the hilus in both cases. Negative hilar potentials were only obtained by modeling imaginary cases of distal dendritic inhibition or proximal excitation (***D***). No such LFP generators were found in the experiments. **D**: Absolute power and dominant polarity of the model LFPs in the hilus for each of the experimental cases plus two imaginary cases representing dendritic inhibition and proximal excitatory inputs (commissural like). All the simulations used identical input activation to reveal the cytoarchitectonic influences. The maximum power was obtained for inputs with stronger dipolar moment (e.g., distal LPP input), regardless of the polarity. Modified from Fernández-Ruiz et al., 2013.

A plausible interpretation of the aforementioned observations is that outward somatic currents (either active or passive) add up preferentially in the hilus and they generate positive LFPs. However, to comprehensively interpret the way volume-conducted currents sum or cancel at sites distant of the generating cells, both the cellular geometry and population architecture

must be considered. We first explored a key aspect of the former, the number, and orientation of the GC dendritic arbors.

The simulations were repeated using the source configuration of a somatic inhibition in realistic GCs with a single polarized dendritic tree (Figure 3.9A) or imaginary GCs with two dendritic trees, more similar to the morphology of hippocampal and cortical pyramidal cells (Figure 3.9B). For simplicity, we sampled the LFPs on the planar section of the GC population. Compared with the realistic morphology with only one dendritic tree (Figure 3.9A), a bipolar dendritic arbor led to dramatic changes in hilar LFPs, which were smaller in magnitude and display negative polarity (Figure 3.9B). Examining the spatial distribution of the current density and potential (dashed and continuous lines in the right panels), large potentials were confined to a narrow cellular domain containing the active synapses. Whereas in the realistic neuronal configuration outward currents exited the cellular compartment through the somatic surface in both blades and they entered the hilus (Figure 3.9*A*, high density of lines of current), in the bipolar dendritic configuration they were cancelled out except in a small region at either edge (Figure 3.9*B*). In all cases, the dominant polarity of the LFP in the hilus was determined by the direction of the currents in the closer cellular compartment (as long as the distance between parallel layers remains constant within certain limits).

We next examined the influence of the relative polarity of dipole layer generators on LFP magnitude by simulating an imaginary model of the DG in which the GCs were similarly oriented in both blades instead of having an inverted disposition (Figure 3.9C). We did this to obtain an identical, instead of opposite, source distribution in both blades. This configuration yielded hilar LFPs with the smallest amplitude and displayed a polarity reversal half way between cell layers, right in the middle of the hilus.

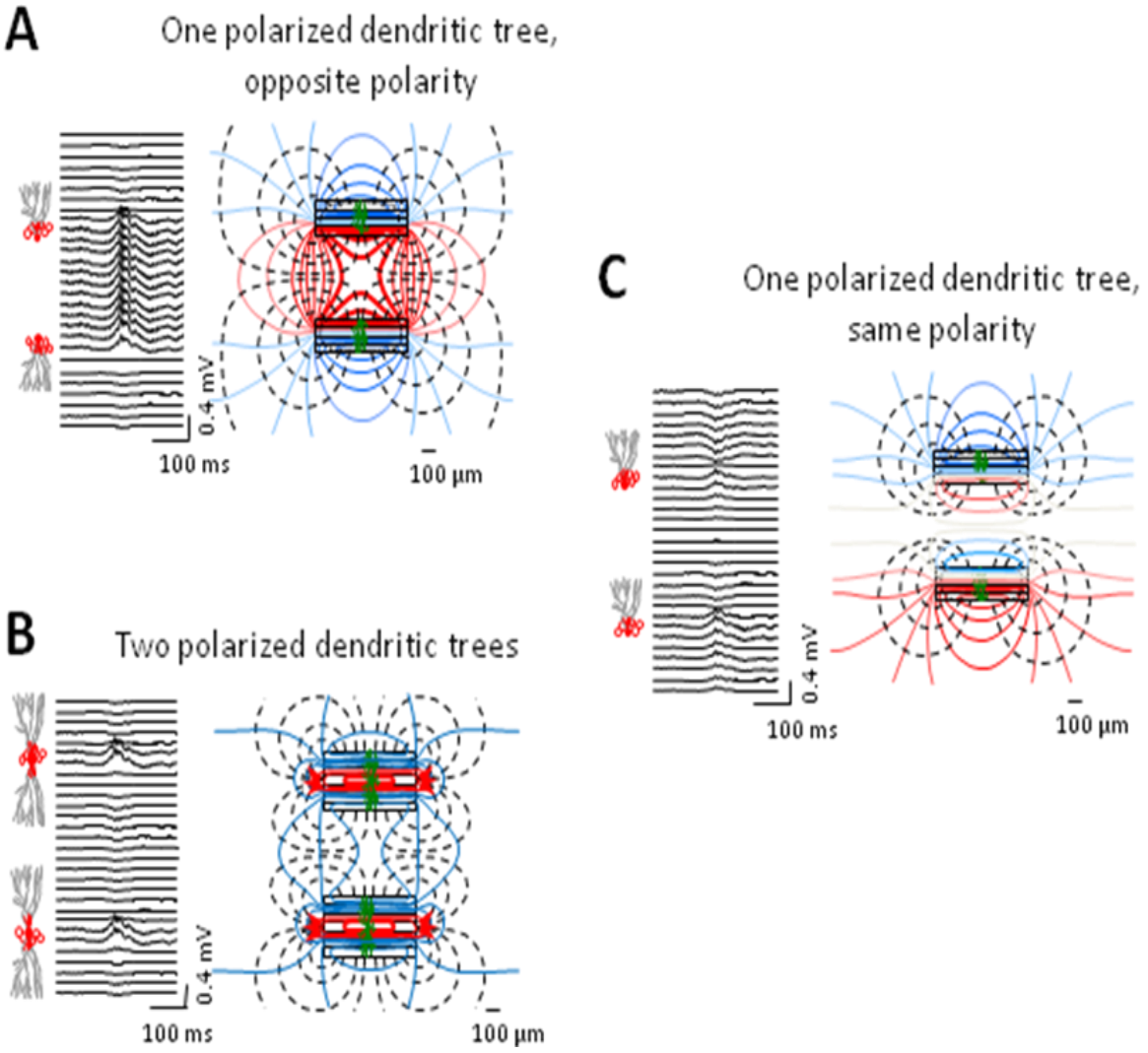

Figure 3.9: **A:** LFP profile along a vertical track crossing the planar section of the DG obtained from the activation of GCs with a somatic inhibitory input. Note the large amplitude and positive polarity of hilar potentials compared with dendritic sites. The lines of current (black dashed) and isopotential lines (solid colored) to the right show the collective behavior of the cell component (stacked rectangles) as a laminar dipole in which the soma layer oriented toward the hilus acts as the current source and the outer dendritic segment as the current sink. **B**: Similar plots were constructed for the LFPs generated by the same input introduced in a DG formed by hypothetical GCs with two polarized dendritic trees. Note very small negative LFPs in the hilus. Only perisomatic layers exhibited sizable LFPs with positive polarity. The bulk of the inward currents were directed toward inner synaptic sites, spreading weakly through the outer volume. **C**: When the same input was introduced to a hypothetical DG in which GCs had single dendritic arbors but same polarity in both blades the simultaneous somatic inhibition in the two blades cancelled out the hilar LFPs, while distant sites beyond the cell layers developed weak negative and positive potentials. Modified from Fernández-Ruiz et al., 2013.

3.2.2. Influence of Dentate Gyrus cytoarchitecture

Although the aforementioned simulations explain the polarity of hilar potentials, they do not fully clarify why LFPs are larger in this region than near the synaptic domain or how they propagated away from the cellular layers. We investigate the influence of the geometry of the DG on the generation and propagation of LFP focusing only in one of the identified sources, the MPP, as geometrical factors should affect similarly to the fields elicited by each synaptic input.

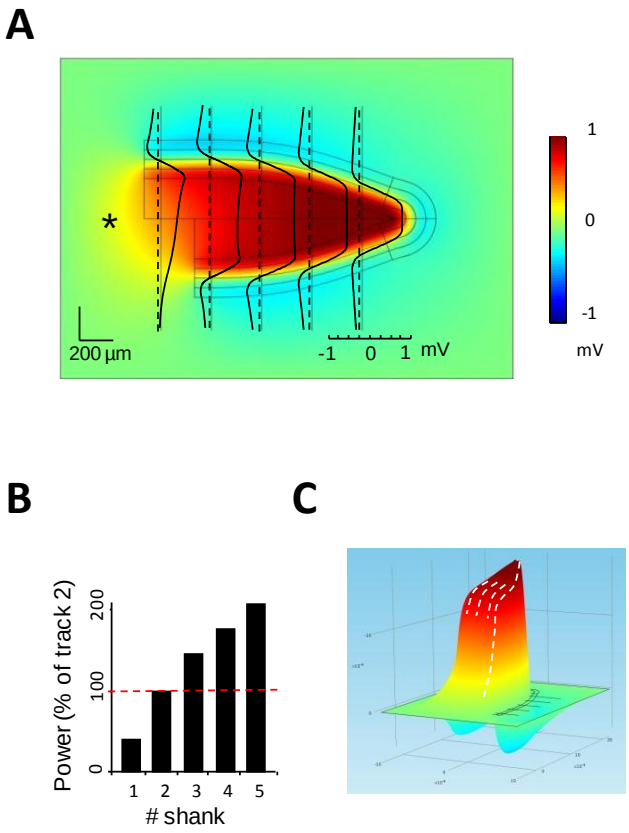

Figure 3.10: **A**: 2D voltage distribution after the activation of DG by an MPP input. Linear recording tracks were placed every 200 µm and averaged voltage profiles plotted (black curves). Note positive hilar potentials getting larger closer to the apex (concave part). This voltage distribution was very similar to the one obtained experimentally (compare with Figure 3.1.3C). **B**: Mean power of LFP in the middle of the hilus expressed as percentage of track 2 power illustrates the same effect. **C**: The three-dimensional representation of the amplitude and polarity helps to visualize the giant positive potentials confined to the hilus. In contrast, smaller negative potentials are generated in synaptic and outer sites. Note that the asymmetrical segregation of positive and negative LFPs in the volume belongs to a single synaptic input. Modified from Fernández-Ruiz et al., 2013.

The 2D voltage distribution of the experimentally recorded MPP input was characterized by small negative dendritic potentials and large positive potentials in the hilus whose power increased toward the apex (see Figure 3.3C and Fernández-Ruiz et al., 2013a). Identical results were obtained in the simulations, when the model was fed with MPP-like (i.e. medial dendritic excitation) current distributions (Figure 3.10*B;* note that we plotted LFPs in five vertical tracks so that one was placed in a zone with a single blade at the open end). Examination of the lines of current revealed that the increasing concentration of outward currents toward the apex was brought about by the concave structure. The largest spread of volume-conducted currents out of the DG was through the open end (asterisk), resulting in positive LFPs of significant amplitude (as much as 0.5 mV up to 400 μm from the cell layers). This indicates a possible large "contamination" of DG activity in LFPs recorded in proximal CA3. The power of simulated hilar LFPs along the midline followed the same spatial trend as that seen *in vivo* with the apex exhibiting an amplitude around 5-fold that of the open end (205.3% and 39.3% the value in shank no. 2, respectively). The pseudo-3D representation of the MPP evoked LFPs revealed the sharp spatial transition and the relative magnitude of positive and negative LFPs (Figure 3.10C) both in and between cell layers.

The aforementioned results suggested that the large amplitude of hilar potentials is due to simultaneous activation of the GCs in the two blades. We further investigated this by simulating an input to only the lower blade of the DG. As only the lower blade remained active, the DG was virtually converted into a planar structure, and we found that hilar LFPs were dramatically reduced (10.7–24.7 % of control values in tracks 1–5; Figure 3.11), whereas the negative LFPs in the synaptic sites of the lower blade appeared to increase, as the removal of positive hilar potentials reduced cancellation (Figure 3.11A-B, red arrows). Notably, with only lower blade activation, positive fields propagated across the top blade and above (Figure 3.11A-B, compare red ovals), due to the loss of the mutual cancellation of extracellular currents from laminar dipoles of opposing polarity. We also calculated the ratio of LFP power in the hilus versus the str. moleculare (points were separated by 300 μm; Figure 3.11*D*) as a measurement of the boosting effect produced by layer folding and curvature. In planar structures, this ratio is close to one due to the symmetry of the electric field in laminar dipoles. The ratio increased from ~4 to ~22 toward the apex for homogeneous activation in the two blades, and it fell below 1.5 when only the bottom blade was activated (Figure 3.11*D*, grey bars).

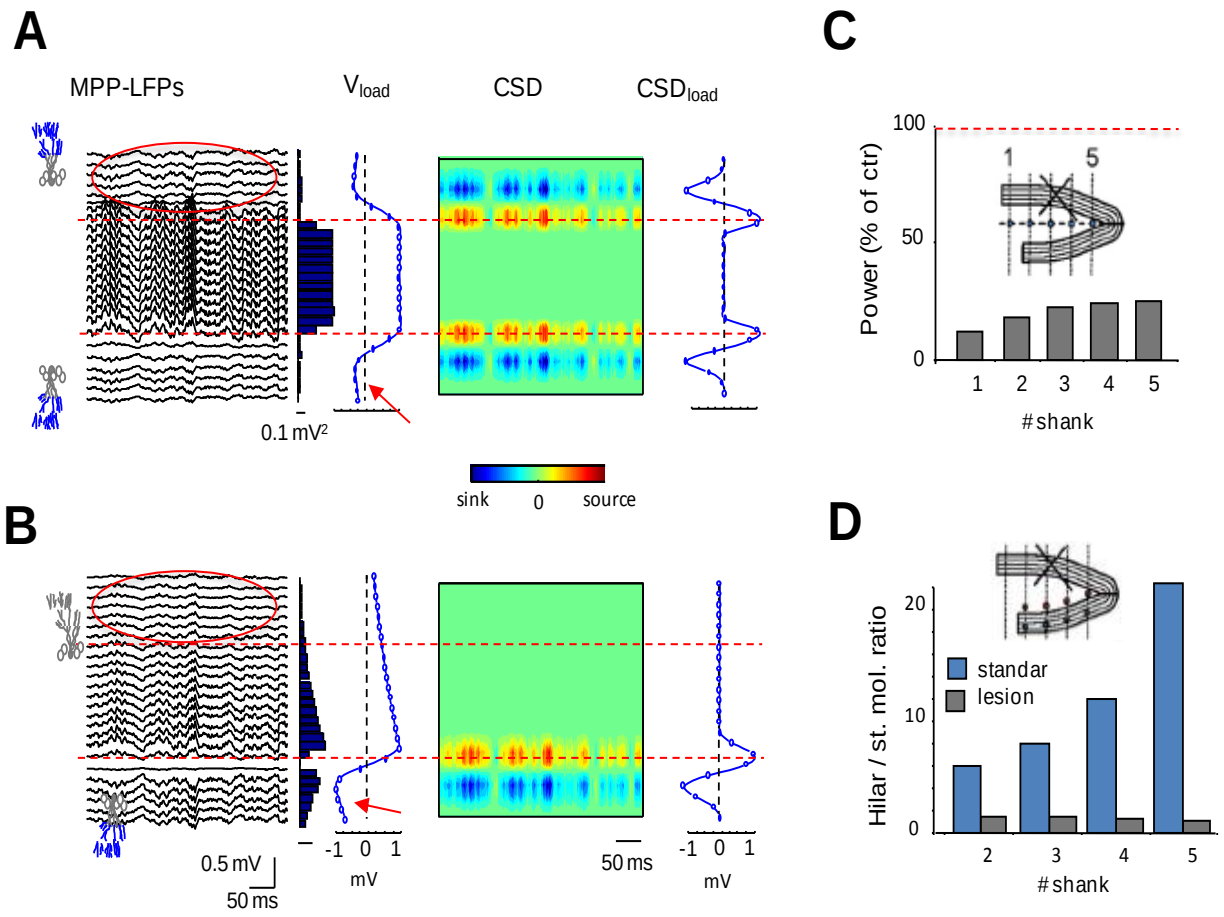

Figure 3.11: LFP and CSD profiles after activation of both DG blades (**A**) or only one (**B**). Note the strong reduction of LFP power in the hilus (histograms), and the modification of the spatial distribution of MPP potentials (V_{loads}), which resembled synaptic activation in a single planar layer (linear decay from the active blade). Despite the intact CSD_{load} distribution in the lower blade, the local synaptic sites increased in amplitude (small red arrows) due to reduced cancellation by the absence of positive potentials from the other layer. Note that LFPs were also evident in the deactivated blade (compare red ovals), as the current reached this location volume-conducted through the hilus from the distant active blade. No reversal of polarity was observed for these LFPs. **C**: Power of the hilar LFPs inactivation of the top blade expressed as the percentage of control (homogeneous activation in the two blades). Inset illustrate sites (in blue) used for estimations. **D**: Hilar to stratum moleculare ratio of LFP amplitude in control and after inactivation of the top blade. The pairs of sites used for estimation were 300 µm apart along recording tracks (inset). Note the increasing boosting effect toward the apex in control and the nearly complete linearization after the inactivation of the top blade, which then reached values close to 1. Modified from Fernández-Ruiz et al., 2013.

The results obtained from the simulations and presented in this section were replicated also experimentally (Fernández-Ruiz et al., 2013b). In urethane-anesthetized rats we performed local injections of DNQX to block all excitatory synaptic activity in one blade of the DG while recording its LFPs with a four-shanks silicon probe covering the whole structure. This pharmacological manipulation was equivalent to the simulation where only one of the GC layers was activated. In those experiments we observed also a dramatic reduction of hilar LFPs and very similar LFP and CSD profiles for the *MPP* elicited LFPs as those presented here.

These results confirm the important role of layer folding and curvatures in the boosting of hilar potentials and the necessity of incorporating cytoarchitectonic features into simulations for correctly interpreting intracranial or even surface EEG recordings.

3.2.3. Influence of spatiotemporal dynamics of synaptic inputs

As the simulations performed so far were designed to study the influence of structural factors (i.e. cell morphology or tissue geometry) we do not take into account the spatiotemporal dynamics of the synaptic inputs. For this reason the activation of the whole GC population was always synchronous. As a next step we performed simulations using different synaptic inputs of varying spatial coverage and position. To this end, GCs blocks of varying size (200, 400, or 800 μm in extension) were activated pairwise in both blades with different (uncorrelated) inputs obtained from experimental recordings (Figure 3.2.5). To better evaluate the mixing of currents from different GC sources the activated blocks were non-overlapping, i.e., only one input was injected to each GC block.

When we considered a representative simulation is considered that involves four inputs to 400-μm-wide spatial modules and recording across a shank placed the middle of DG (no. 3, located across blue modules; Figure 3.12*A*), the LFPs contained a mixed contribution by all four active strips. The mixture of activities recorded along a given vertical track can be separated by ICA from the linear LFPs. In the simulation illustrated here, ICA revealed three components, each with distinct spatial distribution and magnitude (Figure 3.12, V loadings).The largest IC corresponded to activity from the local (blue) GC population surrounding recording shank 3, whereas the other two captured the volume-conducted activity from adjacent modules (green and

red blocks). Voltage loadings retrieved for distant sources (red and green traces) were similar to that of the local sources but considerably spatially smoothed, while CSD loadings of the ICs revealed only large currents for the local component. Importantly, hilar LFPs were smaller than those observed during synchronous activation of the whole DG, and the amplitudes approached those recorded in the dendritic domains (Figure 3.12*A*, histogram). The multiple current sources contributing to hilar LFPs caused continuous variation of the spatial coherence of LFPs within the hilus due to the uneven spatiotemporal contribution of the sources. The spatiotemporal distribution of hilar LFPs may become very complex and heterogeneous, as illustrated by sample snapshots of the voltage distribution, magnitude, and polarity at different instants (Figure 3.12*B*). The cytoarchitectonic influence of co-active modules and strong curvatures could still be examined by comparing the mean power of LFPs in different configurations (Figure 3.12*C*). Together, our simulations revealed a number of effects relevant to the interpretation of LFPs in the DG: (1) regardless of the number and spatial coverage of the synaptic inputs, the power of hilar LFPs increased toward the apex (Figure 3.12D) and always reached a maximum amplitude lower than that induced by a synchronous input to the whole DG; importantly, even the narrowest mirrored strips produced larger LFPs than a single blade activation (Figure 3.12C-D red bars); (2) the decrease of LFP power was more accentuated in the narrower activation modules due to the reduced clustering of volume-conducted currents in smaller modules (86 ± 14%, 52± 8% and 33 ± 11% of control LFP power - taken during synchronous activation of the whole DG-averaged over all five recording tracts in configurations with 800, 400, and 200-μm-wide modules, respectively; mean ± SEM; Figure 3.12C-D); (3) compared with homogeneous activation by a single input, the reduction in power in the central tracks was greater for the larger modules (Figure 3.12*C-D*; although the absolute value remained unchanged), whereas the apex was less sensitive to module size; and (4) the unbalance of positive and negative relative amplitudes in both sides of the GC domains decreased markedly. This heterogeneous spatial behavior was a combined function of multiple factors, including the size of spatial modules, layer separation at the open end and the radius of DG curvature.

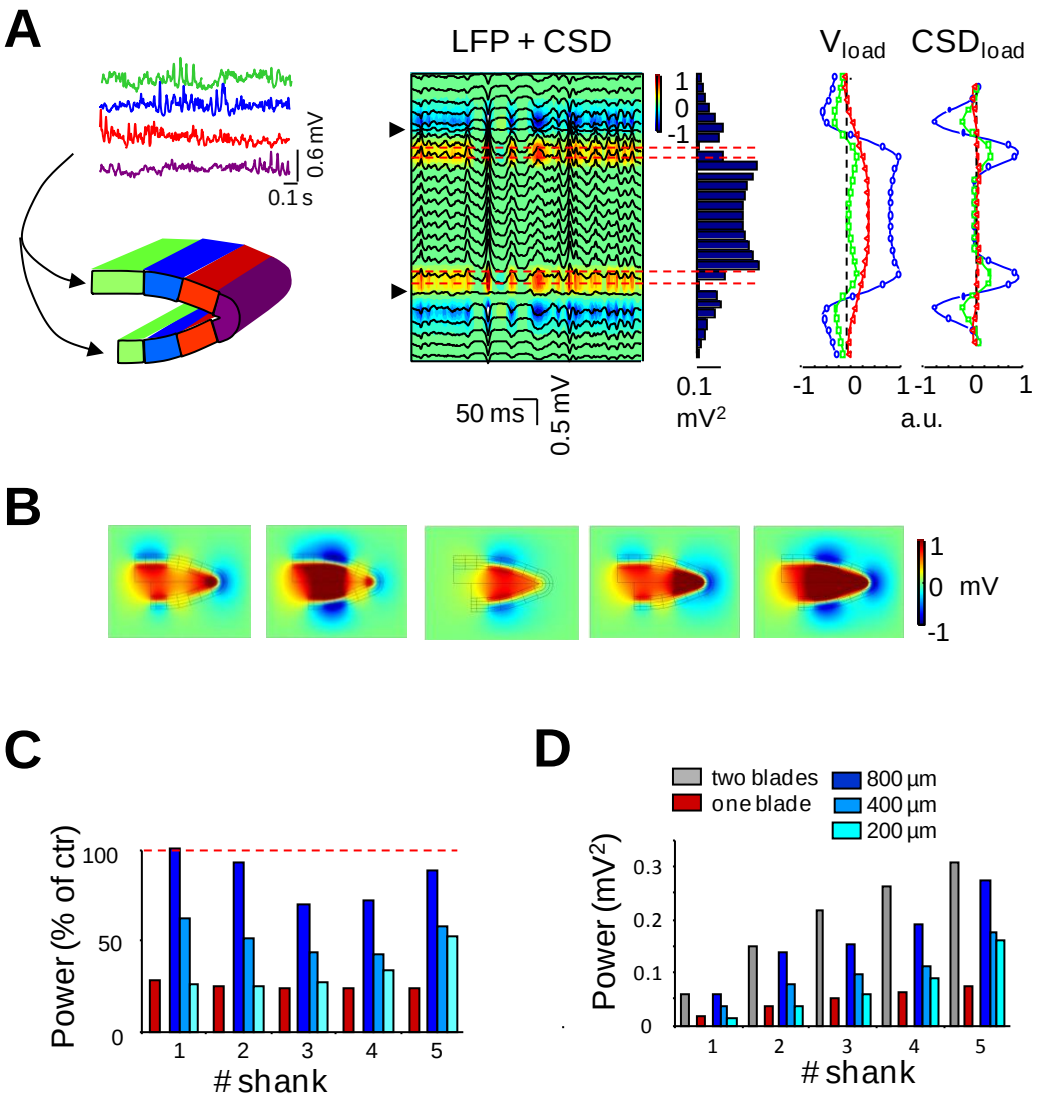

Figure 3.12: **A**: Results obtained for a model configuration using non-overlapping, 400- µm -wide modules in both blades (left, colored). Activations (top, colored traces) in all the domains where uncorrelated. A representative epoch of simulated LFPs and its CSD maps calculated for the central track (no. 3). In the histogram of mean LFP power there is a large reduction in power in the hilus compared with the uniform activation by a single input. ICA disentangled the local activity (blue) from that in adjacent domains that had mixed with LFPs by volume conduction (V_{loads} and CSD_{loads}). **B**: Snapshots of voltage distribution at four different instants reflect the extremely varying spatial distribution of LFPs contributed by multiple sources in **A**. Note the extreme variation and regionalization of hilar potentials. **C**: Change in the mean LFP power along the hilus normalized to the control (i.e., coherent input in the two blades), and the change in the absolute power (**D**) for the different configurations of GC population activation either in mirrored modules of different sizes (blue bars) or as a single source extending through one or the two blades. Modified from Fernández-Ruiz et al., 2013.

We also calculated the ratio of LFP power in the hilus versus that in the GC dendritic domains, as this value is highly sensitive to the size of the spatial coverage of inputs. The hilar/ str. moleculare power ratio estimated between points 300 μm apart in the same recording track (Figure 3.13*A*, inset) increased toward the apex due to the shorter distance between the current sources in both blades and the proximity to the concave DG section. In any given recording track, this ratio decreased in parallel with the size of the activated modules (Figure 3.13*A*, blue bars), confirming that this value serves as an index of the spatial extension of synaptic inputs. In all cases, the lowest ratio (close to 1) was observed during activation of a single DG blade (red bars), whereas the largest ratio was observed when both blades were activated in total synchrony (gray bars). Notably, the contribution of an entire single blade to the hilus was much lower than that of the mirrored activation over a reduced GC module (Figure 3.13*A*, compare one blade versus 200 μm module activation).

The covariance of LFPs recorded at two sites depends on the distance and the temporal dynamics of the active sources whose currents elicit measurable LFP at these points. This was estimated by the cross-correlation index of LFPs in pairs of sites that were increasingly far apart (Figure 13*B*). The activation of a single pathway extending throughout the entire GC population (two blades) generated correlated temporal dynamics everywhere (Figure 13*B*, gray line). However, when two or more modules were active simultaneously with uncorrelated dynamics, the time course of the mixed LFPs varied, hence the correlation decreased. Moreover, the correlation of the LFP at a given pair of recording sites was proportional to the size of the coherently activated modules. This effect was mediated by the differential contributions of volume-conducted currents arising from each of the simultaneously activated sources located at different parts of the DG, as demonstrated quantitatively by the correlation between pairs of points separated by increasing intervals along the middle of the hilus(Figure 3.13*B*, blue lines).

These simulations results can be compared with the experimentally measured DG ICs. The hilar/ str. moleculare power ratio along the DG observed for MPP and LPP inputs was similar to the obtained in the model for the synchronous activation of the whole GC population (Fernández-Ruiz et al., 2013b). Besides the cross-correlation for the activity of both ICs along the DG was markedly higher that the obtained in the model for the activation of small modules of the GC population. Those observations suggest that the most likely case for LPP and MPP

inputs to the GC population *in vivo* is that of synchronous activation of extended domains of GCs in both blades of the DG simultaneously.

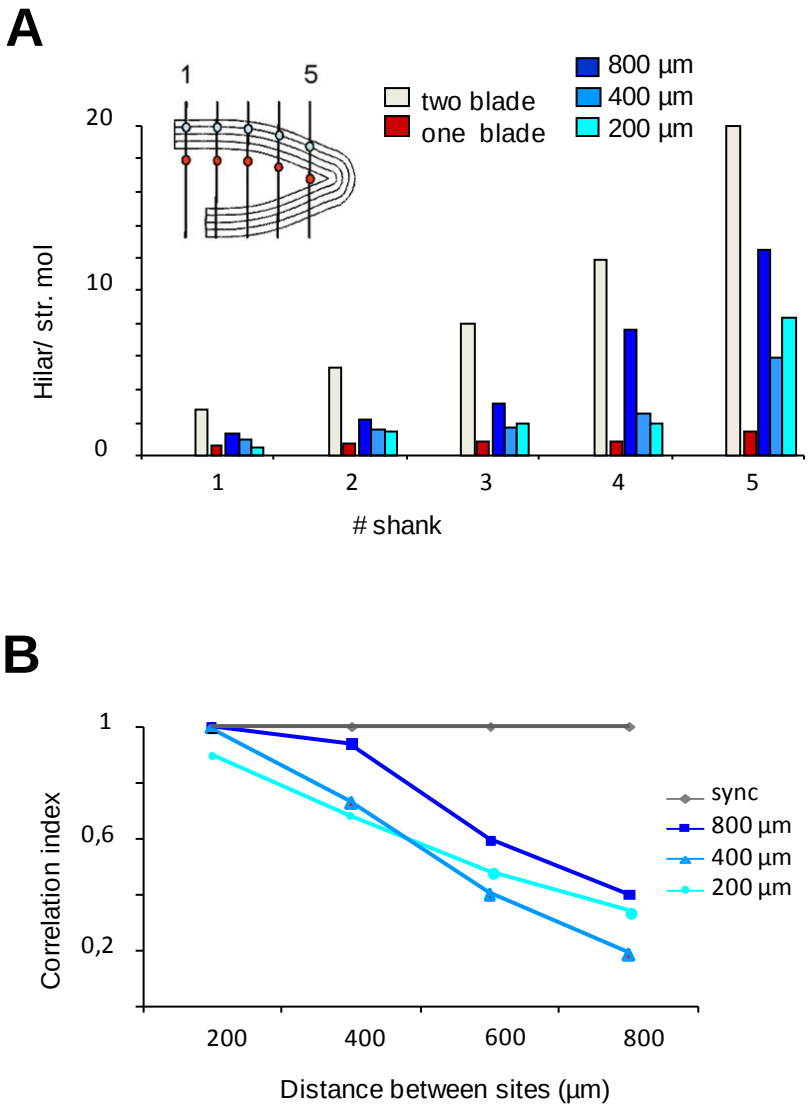

Figure 3.13: **A**: The hilar/GC ratio was measured along the plane of symmetry between hilar and synaptic points of the same track, as indicated in the scheme (inset). Largest values for always obtained with the synchronous activation of both blades (grey bars) and lower ones for the single blade activation (red bars), with intermediate values for the activation of modules of different size (blue bars). **B**: Cross-correlation of LFPs in pairs of sites along the midline in the hilus. Color codes as in ***A***. Modified from Fernández-Ruiz et al., 2013.

The simulation data presented here were derived using multiple inputs in non-overlapping spatial GC domains. Given the complexity of the underlying interactions, we did not present data pertaining to spatially overlapped inputs. However, it can be shown that in cases of complete overlapping of multiple inputs, the resulting LFPs maintained their spatial coherence. Thus, the divergence of hilar LFPs arose from the uneven mixing of the volume-conducted currents produced by the differential spatial coverage in a curved structure, as demonstrated here for non-overlapping inputs.

In the present section we have studied the genesis of LFPs in the DG as a way to investigate the influence of tissue geometry on extracellular potentials in curved structures of the brain. We have shown that it is the particular U shape of DG with opposite dipoles, activated synchronously in both blades, the responsible of the enormous amplitude with positive polarity LFPs in the hilus. This particular architecture exerts a boosting effect over extracellular potentials, amplifying them and invalidating the established assumptions about LFPs that are fulfilled in laminar structures. The accomplishment of a mesoscopic tridimensional model of rat DG and the application of FEM to resolve extracellular fields, led us to quantitatively evaluate the influence of different geometrical (curvatures, relative polarity of the sources) and dynamical (synchrony, spatial correlation) factors in shaping LFPs

3.3. Theta-gamma cross-frequency coupling in the hippocampus-entorhinal circuit

The hippocampal-entorhinal system is characterized by the ubiquitous occurrence of distinct oscillatory patterns, including the prominent theta and gamma rhythms (Buzsaki et al., 1983; Leung, 1998; Buzsaki 2002; Fell and Axmacher, 2011, Vanderwolf, 1969). Theta phase coordination of gamma rhythms within and across brain regions has been studied extensively, however its cellular mechanism and functional relevance remain largely unknown (Bragin et al., 1995; Lisman and Idiart, 1995; Lisman and Jensen, 2013; Schroeder and Lakatos, 2009; Canolty and Knight, 2010; Fell and Axmacher, 2011; Buzsaki and Wang, 2012; Colgin et al., 2009).

The CA1 region of the hippocampus is under the control of two major upstream regions: hippocampal area CA3 and the entorhinal cortex. CA3 axons make synapses with CA1 pyramidal cells in the stratum radiatum while layer 3 entorhinal cells (EC3) innervate the stratum lacunosum-moleculare (Witter et al., 1989; Amaral and Witter, 1989). Their layer-segregated inputs mediate both dendritic excitation and feedforward inhibition in CA1 (Buzsáki, 1984). To determine the coordination of gamma oscillations by the theta rhythm in CA1, the dynamic interactions between the entorhinal and CA3 inputs to the CA1 region, and their impact on the CA1 output, we used high-density extracellular recordings, combined with source separation techniques, while rats performed different navigational tasks and slept in their home cages.

Experiments were carried out while animals ran on a linear track (250 cm long), a T-maze or open field (Mizuseki et al., 2009; Mizuseki et al., 2012; Pastalkova et al., 2008; Diba and Buzsáki, 2008; Montgomery and Buzsáki, 2007; Berényi et al., 2014). Theta epochs during behavioral tasks were classified as RUN, while those during sleep were classified as REM.

3.3.1. Sources of gamma oscillations in CA1

It was already known that the phase of theta rhythm modulates the power of gamma oscillations; however, large controversy remains regarding how many independent gamma oscillators are present in the CA1 region and how are their exact interactions (Colgin et al., 2009;

Belluscio et al., 2012; Scheffer-Teixeira et al., 2013; Lasztoczi and Klausberger, 2014). Thus the first goal of this part of our research was to clarify those points.

We took the times of theta activity during both sleep (REM) and behavior (RUN) and concatenate epochs until having acceptable homogeneous samples of 600 s that were used for subsequent analyses. RUN/REM comparisons were performed for theta epochs from the same session and animal.

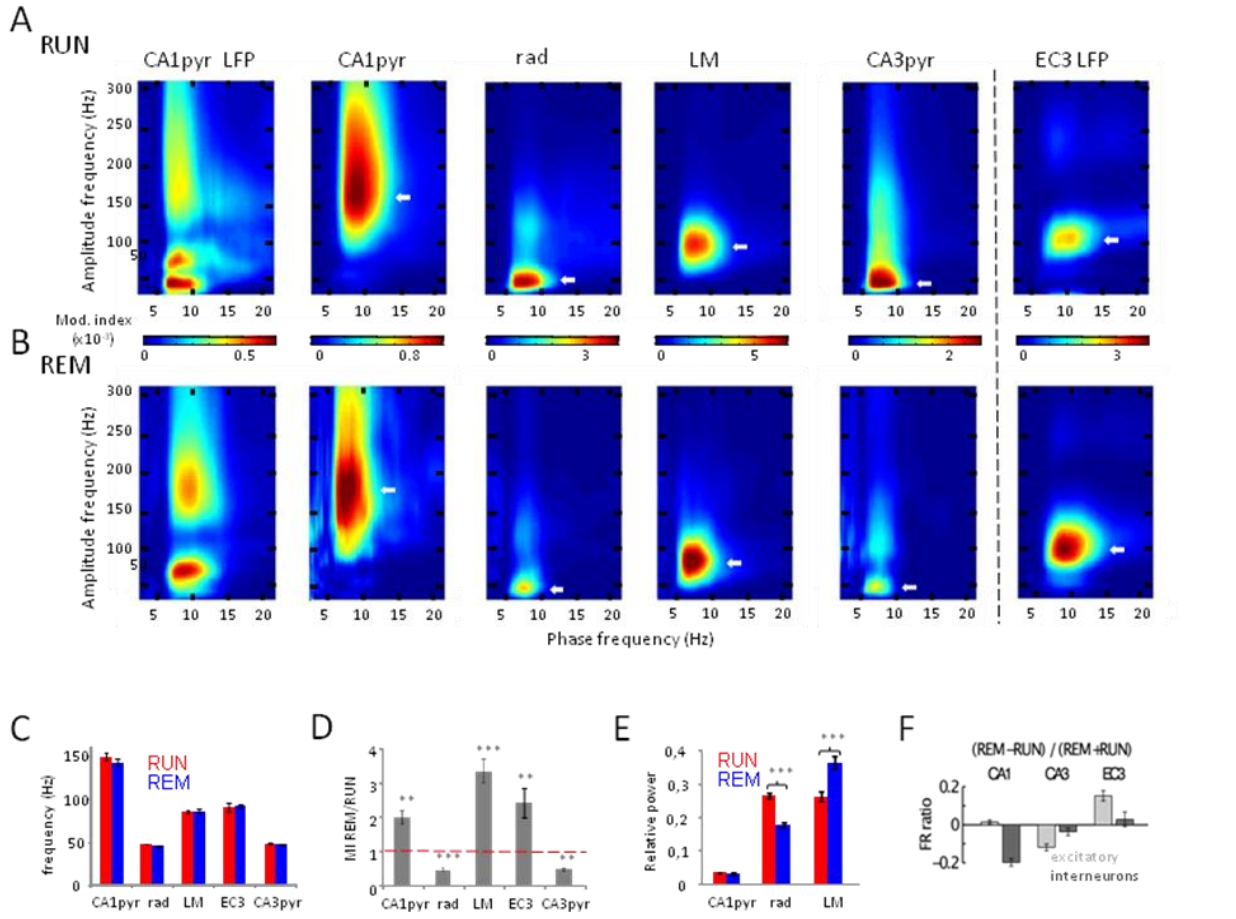

Figure 3.14: **A:** Gamma amplitude-theta frequency comodulogram of LFP in the CA1 pyramidal layer (CA1 str. pyr. LFP) showed strong theta phase modulation of three gamma sub-bands during RUN ($gamma_S$, $gamma_M$, and $gamma_F$; white arrows). Each IC obtained for CA1 LFPs displayed modulation in one dominant sub-band. White arrows indicate the frequency of peak power. Note similar gamma frequencies in the rad and CA3pyr ICs, and the lm IC and EC3 LFP, respectively. **B:** Same as in A during REM sleep. **C**: Group data of peak frequencies (six rats for CA1 and CA3 ICs, four rats for EC3 LFP). **D** and **E**: REM/RUN MI ratio (D) and relative power (30–300 Hz) in different layers (E). (*/**/***$p < 0.05/0.01/0.001$; t test). **F**: Mean ± SEM of firing rate (FR) ratios of single units between REM and RUN ([REM - RUN]/[REM + RUN]). Reproduced from Schomburg, Fernández-Ruiz et al., 2014.

We filtered CA1 pyramidal layer LFP in a broad gamma band, from 30 to 300 Hz, and extracted the signal amplitude for every frequency step by means of complex wavelet transform (see Methods). I also filtered the LFP between 1 and 20 Hz and by the same procedure extracted the phase for every frequency step. Then we calculated the modulation of the high frequency amplitude by the phase of the slower frequency employing the modulation index (MI) introduced by Tort et al., 2010. With the MI for every amplitude-phase pairs we constructed 2D comodulogram plots (Figure 3.2.1A-B). This procedure reveals three distinct but overlapping gamma sub-bands during RUN (Figure 3.2.1A, first panel). One of the oscillations occupies the slower gamma spectrum (30-60 Hz) so I labeled it as slow gamma or $gamma_S$, another gamma oscillations span from 60 to 100 Hz so I termed it as mid-frequency gamma or $gamma_M$. The third component spans a wide frequency range of the upper gamma spectrum, from 120 to 250 Hz, so I named it as fast gamma or $gamma_F$.

Because underlying currents of gamma LFP in the pyramidal layer reflect a combination (in unknown proportions) of active excitatory and inhibitory currents and passive return currents from the dendritic layers (Csicsvari et al., 2003; Glickfeld et al, 2009; Schomburg et al, 2012; Fernández-Ruiz et al., 2012), we employed ICA to separate the observed gamma oscillations of the raw LFP into their pathway-specific synaptic sources (see Methods). For this purpose we took the LFPs from all the electrodes located in the CA1 region (thus including the pyramidal and dendritic layers), filtered them between 30 and 300 Hz and performed ICA. The same three main ICs as shown in the previous chapter were found: *CA1pyr*, *radiatum (rad)* and *lac-mol (lm)*. Cross-frequency phase-amplitude analysis of the three ICs revealed significantly theta-modulated gamma bands in all animals ($p < 0.001$ for each IC, surrogate test; 7 animals in total).In the *CA1pyr* IC, theta oscillations most strongly modulated fast gamma frequencies (Figure 3.14A, second panel; mean ± s.e.m., 149.4 ± 4.3 Hz). In the *rad* IC, the dominant theta-modulated gamma frequencies were between 30 and 70 Hz (Figure 3.14A, third panel; 47.3 ± 0.6 Hz). Compared to the *rad* IC, theta-coupled gamma oscillations in the *lm* IC were significantly faster ($p < 0.0001$, t-test; Figure 3.14A, fourth panel; 85.7 ± 1.8 Hz). Thus ICA decomposition of CA1 gamma LFPs was able to separate the contribution of three independent gamma generators, each one with activity in a discrete frequency band.

To clarify the origin of those gamma generators we looked at the CA1 input regions. CA3 pyramidal cells send their axons to the CA1 stratum radiatum and it was already now that they elicit strong slow gamma there (Cscivari et al., 2003, Fernández-Ruiz et al., 2012a; Fernández-Ruiz et al., 2012b; Zemankovics et al., 2013), so they are the most likely candidates for being responsible of radiatum $gamma_S$. When we applied the same procedure as described in this section to the LFP recorded in the CA3 pyramidal layer, we found a theta-modulated gamma band similar to that in the *rad* IC ($p > 0.05$, t-test between frequencies), with a peak frequency of 47.6 ± 1.2 Hz (Figure 3.14A, fifth panel). These similar gamma oscillations can be attributed to the fact that the same CA3 pyramidal cells that send axons to the CA1 also leave collaterals in the same CA3 region (Li et al., 1994; Ishikuza et al., 1990). The CA1 stratum lacunosum-moleculare is densely innervated by axons from the entorhinal cortex layer 3 so we also applied the same analysis to the LFPs recorded there. Gamma oscillations there, were similar to those displayed by the *lm* IC ($p > 0.05$, t-test between frequencies) with a peak frequency of 90.0 ± 4.9 Hz (Figure 3.14A, sixth panel), pointing also to EC3 projecting cells as the responsible for the *lm* $gamma_M$. The *CA1pyr* IC is most likely of local origin because the pyramidal layer and perisomatic region do not receive extrinsic afferences as the dendritic layers but is innervated by multitude of CA1 interneurons. Its peak frequency around 150 Hz suggests that it can be elicited by fast $GABA_A$ IPSPs onto the CA1 pyramidal cells but the fact that its theta-modulated gamma frequency extends up to 250 Hz, suggests that it can capture also contributions from action potentials (Schomburg et al., 2012; Ibarz et al., 2013; Scheffer-Teixeira et al., 2013).

REM sleep is characterized by prominent theta rhythm in the hippocampus so we sought to verify if theta-gamma dynamics described for the RUN state were preserved during sleep. We found the same three ICs for CA1 gamma LFPs during sleep. The frequency distribution of the theta modulated gamma sub-bands was largely similar to waking for all of them and also for CA3pyr and EC3 LFPs (Figure 3.14B,C; $p > 0.05$, t-test). We employed two different methods to quantify the differences between both states. The modulation index (MI, Tort et al., 2008) to quantify the strength of theta-gamma coupling and the relative power (or relative variance of the IC; Fernández-Ruiz et al., 2012) of the gamma filtered ICs. Both MI and power of $gamma_S$ in the *rad* IC were significantly reduced during REM compared to RUN ($p < 0.0001$, t-test; Figure 3.2.1 B,D,E), whereas theta-$gamma_M$ coupling and power in the *lm* IC were significantly increased ($p < 0.0001$, t-test; Figure 3.2.1 B,D,E). These changes were accompanied by a parallel reduction of

theta-gamma$_S$ coupling in CA3pyr($p < 0.01$, t-test; Figure 3.14 B,D) and increased theta-gamma$_M$ coupling in EC3 LFP during REM ($p < 0.01$, t-test; Figure 3.14 B,D).

We also checked the firing of the neurons in the CA1, CA3 and EC3 to see if their changes in firing rate matched with those observed in the LFPs during waking and sleep. Individual units were extracted from the high-pass filtered LFPs and were classified into putative pyramidal cells and interneurons based on their waveform, autocorrelograms and other characteristics (see Methods). For each individual neuron the mean firing rate was calculated for both states and a (REM-RUN) / (REM+RUN) ratio used for comparison. Consistent with the LFP changes, CA3 and EC3 pyramidal neuron firing rates decreased and increased, respectively, during REM compared to RUN ($p < 0.05$, Kruskal-Wallis ANOVA, followed by Tukey's honestly significant difference test; Figure 3.2.1F). In summary, theta-modulated gamma power in the respective dendritic domains of CA1 pyramidal cells mainly reflects the gamma band activity in their respective afferent regions and is modulated as a function of brain state and network architecture.

3.3.2. Coherence segregation of layer-specific gamma sources

If gamma oscillations in the hippocampal CA1 are layer specific as I proposed in the previous section, is to be expected that their within-layer coherence is much larger than their cross-layer coherence. As a first step to verify this, coherence maps in the broad gamma frequency band (30-100 Hz) were constructed between LFPs at reference sites in different layers and the remaining 255 channels. This procedure reliably outlined the anatomical boundaries in CA1 for stratum pyramidale (Figure 3.15A, first panel), stratum radiatum (second panel), and stratum lacunosum-moleculare (third panel).

Then we compared the gamma coherence (30-100 Hz) for all the three main CA1 LFP ICs extracted in every shank of the 8-shanks probe were the appropriated layer was recorded. The coherence matrix for a single case is displayed in Figure 3.15B. High coherence values (warm colors) were only obtained for same ICs in separate shanks but not across shanks. The across animals quantification of coherence relative to distance (n = 6 rats; Figure 3.15C) shows similar results. Gamma coherence remained relatively high (> 0.4) for ICs from different shanks

in the same layer, even up to 1.8 mm away, whereas gamma coherence between ICs from different layers was consistently lower even in the same shank.

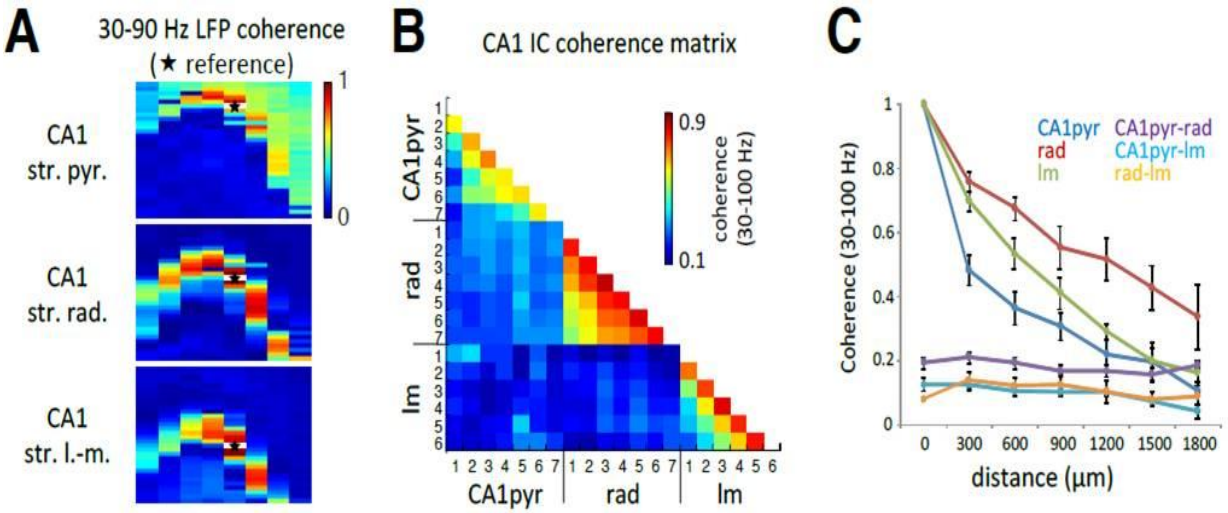

Figure 3.15: **A**: Gamma (30–90 Hz) coherence maps between LFP recorded from a reference site (white patch with star) and every other recording site on a 256-channel probe spanning most of a transverse plane in the dorsal hippocampus in one example session, for CA1 str. pyramidale (top), str. radiatum (middle), and str. lacunosum-moleculare (bottom) references. **B**: Gamma coherence between pathway-specific CA1 ICs (extracted separately for each shank). Similar to cross-layer LFP coherence, ICs reflecting different synaptic pathways exhibited low coherence with other CA1 ICs across all shanks (numbered 1–7), but high coherence between like ICs from different shanks. **C**: Coherence of gamma ICs decreased monotonically with distance between shanks, whereas coherence between different ICs was low, regardless of shank separation. Modified from Schomburg, Fernández-Ruiz et al., 2014.

3.3.3. Theta-phase coordination of gamma oscillations in CA1

Theta-frequency gamma-amplitude coupling analysis was useful to reveal distinct gamma oscillations in CA1. We next sought to study how the theta rhythm organizes those gamma oscillations in time. We next examined gamma power variation as a function of theta phase of the LFP recorded from CA1 str. pyramidale and filtered between 5 and 12 Hz (0° and 180° refer to positive polarity peak and negative polarity trough, respectively). LFP and IC's power was calculated for each frequency step from 30 to 300 Hz by complex wavelet transform. Z-scored gamma power for each frequency was plotted for each bin of theta phase to construct 2D comodulograms. Two theta cycles are represented for clarity.

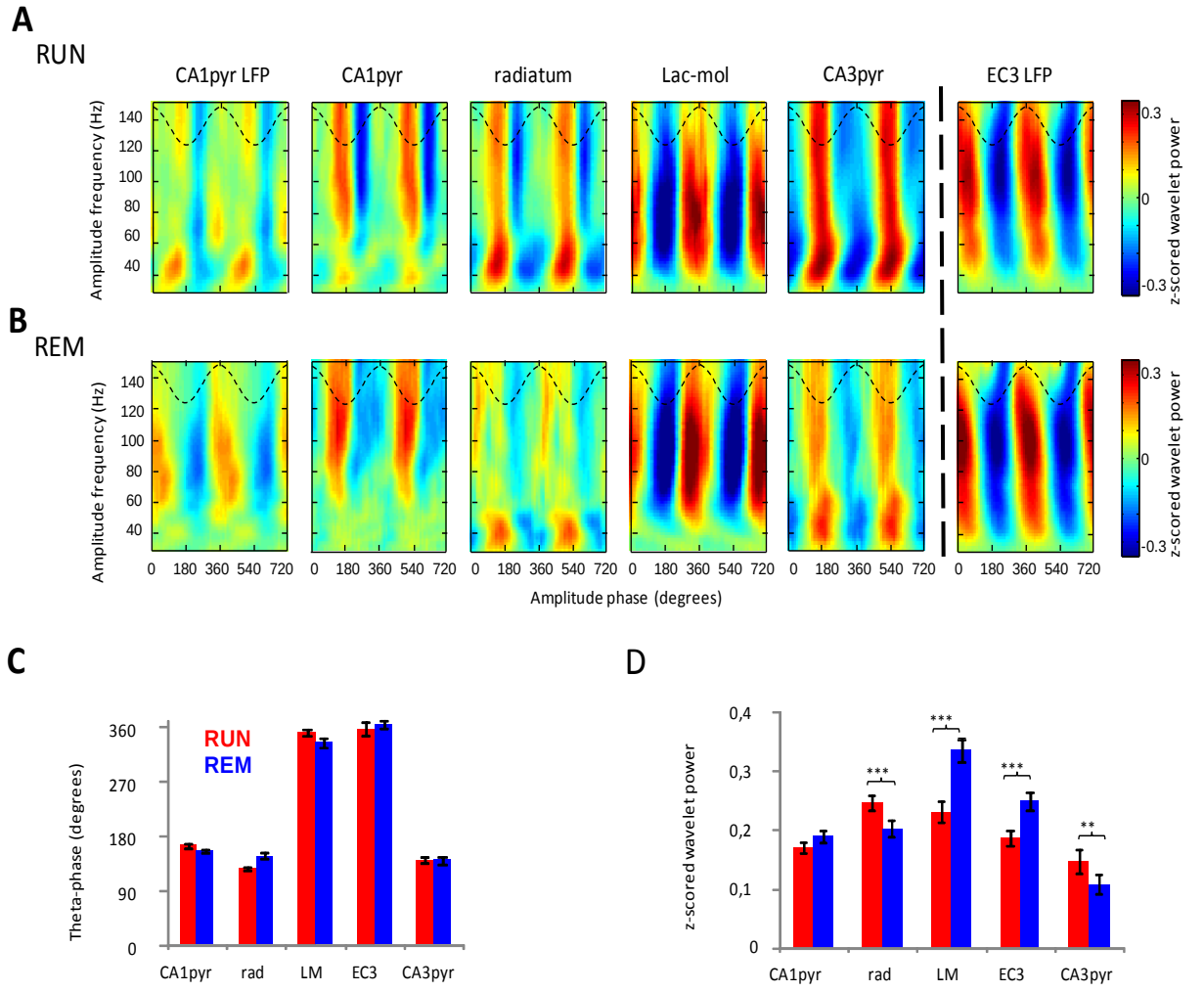

Figure 3.16: **A**: Gamma amplitude-theta phase modulation plots of LFP in CA1 pyramidal layer (leftmost panel) and CA1 LFP ICs during RUN. The $gamma_S$ (single arrowhead), $gamma_M$ (double arrowheads), and $gamma_F$ (triple arrowhead) dominated the descending phase, peak, and trough of the CA1 pyramidal layer theta waves, respectively. Dashed black line, reference theta phase of the LFP recorded in CA1 pyramidal layer. **B**: Same as in (A) during REM. **C**: Group data (six animals for CA1 and CA3, four rats for EC3) for preferred theta phase of each layer's theta-modulated gamma band (30–60, 60–110, and 100–250 Hz for *rad*, *lm*, and *CA1pyr*, respectively). **D**: Z-scored theta-modulated gamma power across animals. (**/***$p < 0.01/0.001$, respectively; t test). Modified from Schomburg, Fernández-Ruiz et al., 2014.

For the LFP recorded from CA1 pyramidal layer we found three gamma sub-bands with distinct theta-phase distribution (Figure 3.16A, first panel): $gamma_S$ (indicated by one arrowhead) at the descending theta phase, $gamma_M$ (two arrowheads) at the theta peak, $gamma_F$ (three arrowheads) at the theta through. Theta-phase gamma-amplitude analysis applied to the

ICs confirms this phase separation and clarifies the layer origin of each gamma component. $Gamma_F$ power (>100 Hz) dominated in the *CA1pyr* IC and was maximal near the trough of the theta cycle (174.8 ± 3.3°; Figure 3.16A,C), coincident with the highest probability of spikes of the CA1 pyramidal cells and interneurons at this phase (Buzsáki et al., 1983; Csicsvari et al., 1999; Mizuseki et al., 2009). $Gamma_S$ (30-60 Hz) was most prominent in the *rad* IC, occurring predominantly on the descending phase of theta (128.3 ± 2.0°; Figure 3.16A,C), which coincides with the preferred phase of gamma oscillations in the CA3pyr LFP (138,9 ± 4,5°; Figure 3A,C), and most CA3 spiking (Csicsvari et al., 2003; Mizuseki et al., 2009). The $gamma_M$ (60-120 Hz) that dominated the *lm* IC was phase-locked to the peak of the reference theta waves (348.8 ± 5.3°; Figure 3.16A,C), coincident with maximal EC3 gamma LFPs (355,8 ± 14,8°; Figure 3.16A,C), and pyramidal cell firing in the entorhinal cortex L3 (Mizuseki et al., 2009).

We also compared the theta phase distribution of gamma power during REM sleep. Although in the raw LFP was not evident the presence of the three gamma bands (Figure 3.16B, first panel), all the ICs display very similar phase and frequency power distribution as during RUN. The theta phase and layer distributions of slow and mid-gamma activity was qualitatively similar to RUN (non-significant differences in theta phases of maximal gamma power, $p > 0.05$, t-test; Figure 3.16B,C), but theta-modulated gamma power decreased in the *rad* and *CA3pyr* ICs ($p < 0.001$, t-test) while it increased in the *lm* IC and EC3 LFP ($p < 0.0001$, t-test) during REM (Figure 3.16B,D).

As a next step, we further looked at the modulation of principal cell firing by the theta phase. For this purpose, we calculated the preferred theta phase for each excitatory neuron during RUN and REM in CA3, EC3 and CA1 (see Methods). The preferred firing phase of most CA3 pyramidal cells during both RUN and REM is at the descending phase of the theta cycle (Figure 3.17, first panel), coinciding with the preferred phase of the radiatum $gamma_S$. In the case of the EC3 pyramidal cells the preferred firing phase in both states is around the peak of the theta cycle (Figure 3.17, second panel), coinciding with the preferred phase of the lac-mol $gamma_M$. During RUN CA1 pyramidal cells tend to fire at the theta through or early ascending phase (Figure 3.17, second panel), however during REM some cells shift their preferred phase toward the peak, reflecting an increased drive by EC3 input during this state (Mizuseki et al., 2010).

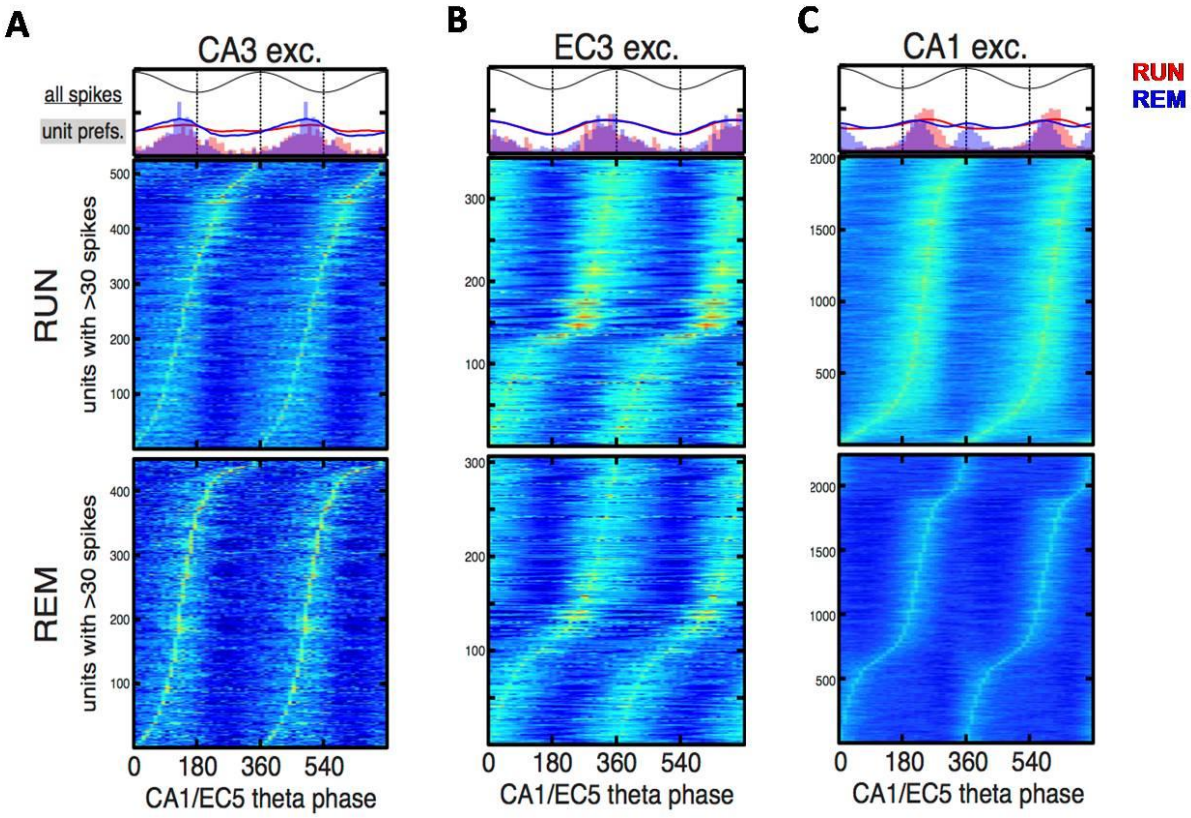

Figure 3.17: Theta-phase modulation of pyramidal cells in CA3 (**A**), entorhinal cortex layer 3 (**B**) and CA1 (**C**) during RUN and REM. Units were sorted according to their z-scored theta-phase firing probability (raster plots). Histograms on the top represent the summed probability distribution of preferred phases and curves the summed probability distributions of firing rates (red for RUN and blue for REM) for all the units that were significantly theta-modulated (Rayleigh test $p < 0.01$). Black curve indicate reference theta phase in the CA1 pyramidal layer or entorhinal cortex layer 5. Note that the preferred phase for CA3 and EC3 pyramidal cells is similar to that obtained for rad and CA3pyr $gamma_S$ and lm and EC3 LFP $gamma_M$ (compare with figure 3.2.3A,B).

The diagram in Figure 3.18 summarizes the above results and proposed schematics for CA1 network function. At the theta peak, projection neurons in entorhinal cortex L3 increase their firing eliciting $gamma_M$ oscillations locally and in the stratum lacunosum-moleculare. After that, during the descending theta phase, CA3 pyramidal cells fire evoking $gamma_S$ oscillations also locally and in the CA1 stratum radiatum. The same CA3 axons that innervate pyramidal cell dendrites in the str. radiatum make abundant synapses onto CA1 interneurons. This feedforward

inhibition may be responsible for the $gamma_F$ oscillations at the trough of the theta cycle. The firing probability of CA1 pyramidal cells is maximal around and after the theta through so it may be enhanced by the integration of coincident inputs from EC3 and CA3 and their exact timing controlled by the fast perisomatic inhibition, however this hypothesis still need to be demonstrated.

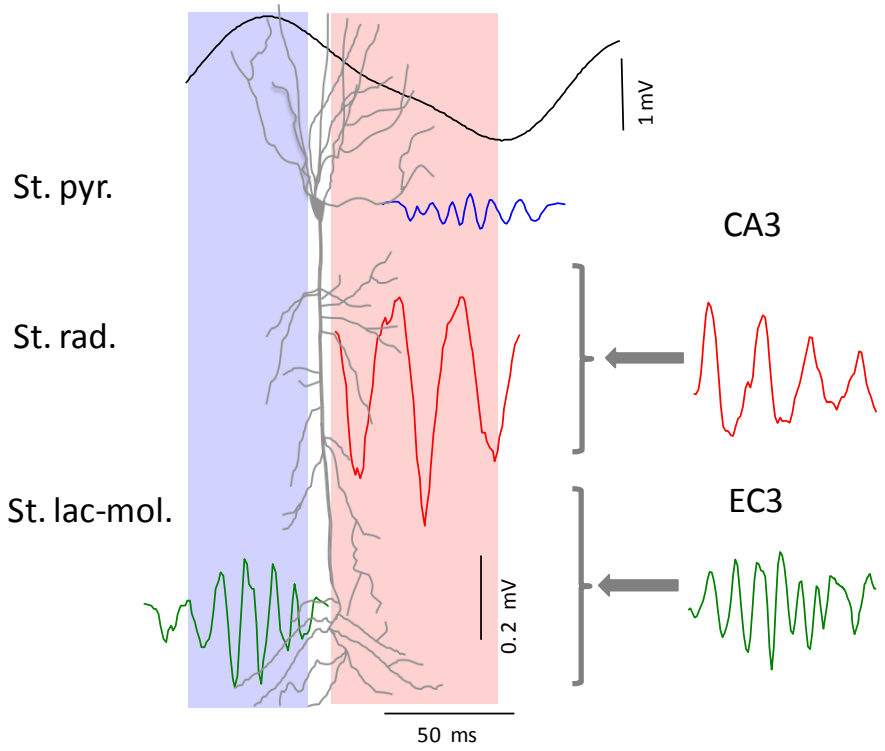

Figure 3.18: Diagram summarizing the average ordering of the maximal phases for the gamma sub-bands, afferent input, and CA1 spike output over the theta cycle. Reproduced from Schomburg, Fernández-Ruiz et al., 2014.

3.3.4. Variation of theta-coupled gamma oscillations along the CA1 transversal axis

Along its transversal axis the CA1 region can be divided into a proximal region (closer to the CA2/CA3 border), an intermediate and a distal region (closer to the subiculum). There are important anatomical differences among them, as different entorhinal regions innervate the proximal and distal poles (Steward, 1976; Witter et al., 1989). It has also been suggested a functional specialization along the transverse axis. Place cells located in proximal sites are better

and more spatially informative while those located in more distal sites have multiple place fields and less spatial coherence (Henriksen et al., 2010). Less spatially selective cells in distal CA1 seem to be on the contrary more sensitive to the presence of objects (Burke et al., 2011) and odor cues (Igarashi et al., 2014).

We studied the variation in theta-gamma dynamics along the CA1 transverse axis to check if they can offer a potential mechanism for the observed functional differences. For this purpose, we classified all the recording shanks from 6 animals as belonging to the proximal, intermediate or distal regions of CA1. Then we applied ICA to the LFPs recorded by each shank and performed theta-frequency gamma-amplitude analysis for the three main CA1 ICs, both during REM and RUN states.

Radiatum $gamma_S$ in proximal sites showed a stronger theta-gamma coupling than at distal sites, whereas the opposite relationship was observed for the $gamma_M$ band in the str. lacunosum-moleculare ($p< 0,001$ and $p<$, ANOVA tests; n=6 rats; Figure 3.19A). During REM sleep, *radiatum* $gamma_S$ power decreased in all sites while *lm* $gamma_M$ increased in all of them. However their spatial trends remained constant: $gamma_S$ power gradually decreasing from proximal to distal and $gamma_M$ increasing in the same direction (Figure 3.19B). Conversely, the proximodistal distribution of $gamma_F$ in the pyramidal layer changes as a function of the brain state. During RUN the theta-gamma coupling of the pyramidal layer $gamma_F$ is stronger in proximal sites while during REM it shifted toward the opposite CA1 border ($p< 0,001$ and $p<$, ANOVA tests; n=6 rats; Figure 3.19A,B), coinciding with the trend of the predominant oscillation in each case, str. radiatum $gamma_S$ during RUN and str. lacunosum-moleculare $gamma_M$ during REM.

Changes in *CA1pyr* theta-$gamma_F$ coupling along the proximodistal axis and between RUN and REM mostly reflected changes in its theta phase distribution. A bimodal phase distribution, exhibiting increased power at both the trough and peak, emerged on the distal end during RUN and at all sites during REM (Figure 3.20A). The altered phase distributions were limited to the *CA1pyr* ICs; quantifying the phase distribution with the 'center of mass' of gamma power showed significant variation in *CA1pyr* from proximal to distal ends during both RUN and REM ($p < 0.001$, ANOVA tests; Figure 3.2.7B), but not in the other components ($p > 0.05$, ANOVA tests; Figure 3.20B).

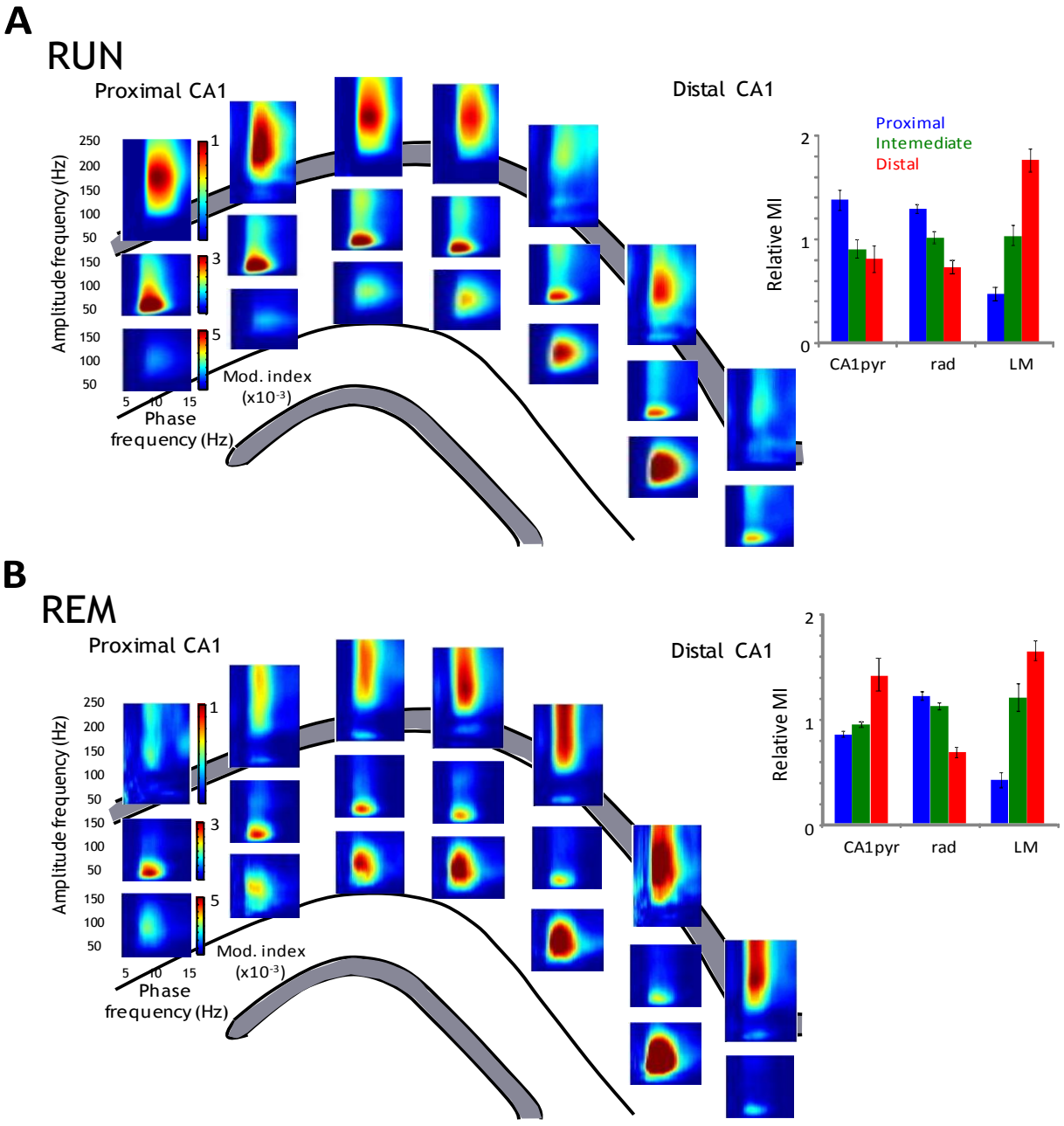

Figure 3.19: **A**: Two-dimensional distribution of the theta coupled gamma oscillations during RUN. Each set of three panels was constructed from the gamma-amplitude theta-phase comodulograms coupling of the ICs on each recording shank. The *rad* IC's $gamma_S$ became less strongly theta-modulated along the transversal (proximo-distal) axis, whereas lm $gamma_M$ increased its theta-coupled gamma power. CA1pyr $gamma_F$ largely followed the *rad* IC gradient. The bar plot on the right shows group data of MIs, normalized by the average across all shanks (six rats). Each comparison showed significant variation from proximal to distal sites ($p < 0.001$; ANOVA). **B**: Similar display during REM. Note the opposite trend of CA1pyr theta-$gamma_F$ coupling along the proximo-distal axis compared to RUN. Reproduced from Schomburg, Fernández-Ruiz et al., 2014.

Regarding the observed variations in the strength of theta-gamma coupling and theta-phase distribution along the proximodistal axis, no significant change in the mean frequency of theta modulated gamma activity was observed for any of the three ICs in both states (Figure 3.20C).

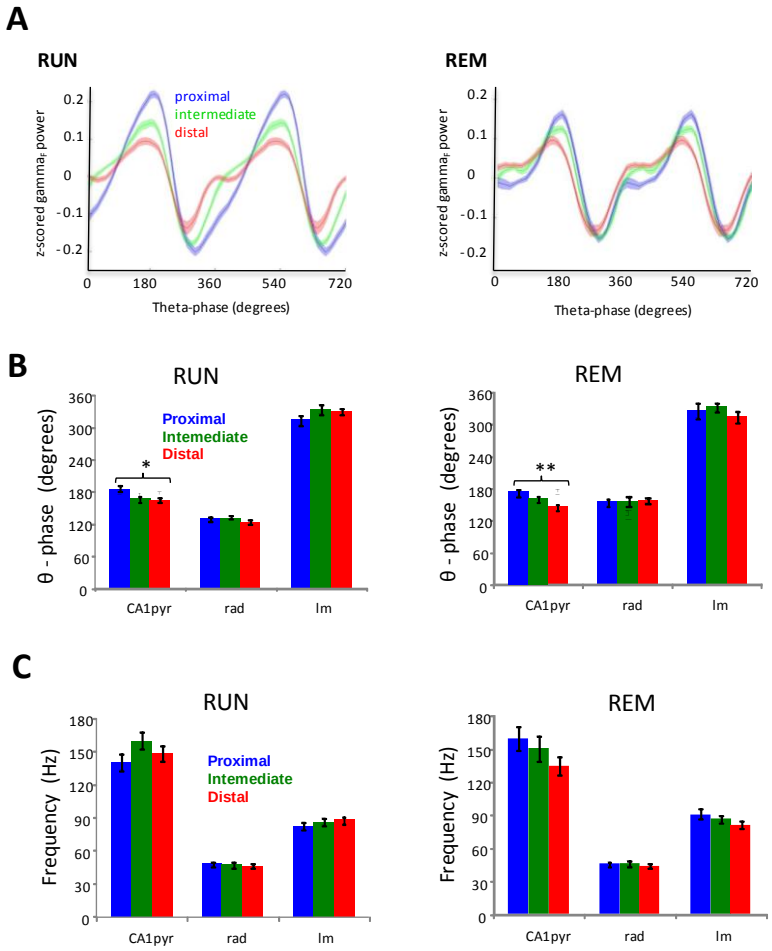

Figure 3.20: **A**: Theta phase distribution of CA1pyr gamma$_F$ power in RUN and REM at three segments along the transversal (proximo-distal) axis of CA1. Note increased bimodality of the gamma$_F$ power distribution (arrowheads) toward the distal end compared to the CA3 end ($p < 0.001$ for mean phases both in RUN and REM, ANOVA tests, six rats) and stronger overall bimodality during REM. **B**: The 'centers of mass' of theta-phase (power-weighted mean phase) of *rad* gamma$_S$ and *lm* gamma$_M$ did not show significant changes along the proximo-distal axis in both RUN and REM ($p > 0.05$, t-test; 6 rats). However the *CA1pyr* gamma$_F$ shifts its preferred theta-phase from the theta trough at proximal CA1 to closer to the theta peak at distal sites in both RUN and REM (*/** $p < 0.05/0.01$, ANOVA tests; 6 rats). **C**: Mean frequency of the three CA1 ICs (*CA1pyr*, *rad*, and *lm*) did not significantly change along the proximo-distal axis of the hippocampus in both RUN and REM states ($p > 0.05$, t-test; 6 rats). Modified from Schomburg, Fernández-Ruiz et al., 2014.

The differences found in the relative strength of the str. radiatum $gamma_S$, elicited by the CA3 input to the CA1, and the str. lacunosum-moleculare $gamma_M$,likely elicited by the EC3 input to CA1 pointed to a heterogeneous contribution of both inputs along the CA1 axis. CA3 inputs appear to be predominant in proximal sites and during RUN while EC3 inputs dominate in distal sites and during REM. Pyramidal layer $gamma_F$ varies along the axis according to the brain state, reflecting its variable modulation by both CA3 and EC3 inputs.

3.3.5. Theta-gamma cross-frequency coupling during a memory task

We have focused here on characterizing theta-gamma dynamics in the entorhino-hippocampal circuits and found different gamma oscillations organized by the theta rhythm. I also found that theta-gamma dynamics in the hippocampus displays strong state-dependent modulation during sleep and navigation; however they have also been implied in cognitive functions, as memory and learning (Buzsáki and Moser, 2014; Lisman and Jensen, 2013). Thus I sought to test if the above characterized gamma oscillations have specific modulation during a hippocampus-dependent memory task. For this purpose I choose the delayed-alternation T-maze task (Ainge et al., 2007; Montgomery and Buzsáki, 2007; Pastalkova et al., 2008). In this task rats learn to run from a starting area through a central arm and then turn left or right, collect a water reward a return to the starting area (Figure 3.21A). To increase their motivation for doing the task, rats are water deprived and can only drink during the task. After one of such trials they are forced to wait for 5-10 seconds and then start over again, but to get the reward animals have to turn to the opposite direction as in the previous trial. After a few days of training animals learn the task reaching a performance above 80 % (an error is when the animal chose to turn to the same direction as the previous trial). It has been shown that rodents with impaired hippocampal function cannot successfully perform this task (Aigne et al., 2007). In the central arm the animal is recalling the previous memory and uses this information to make a correct choice in the juncture of the maze. In the lateral arms the animal is encoding the current direction and has to keep this information in the working memory during the delay period (Wood et al., 2000; Montgomery and Buzsáki, 2007).

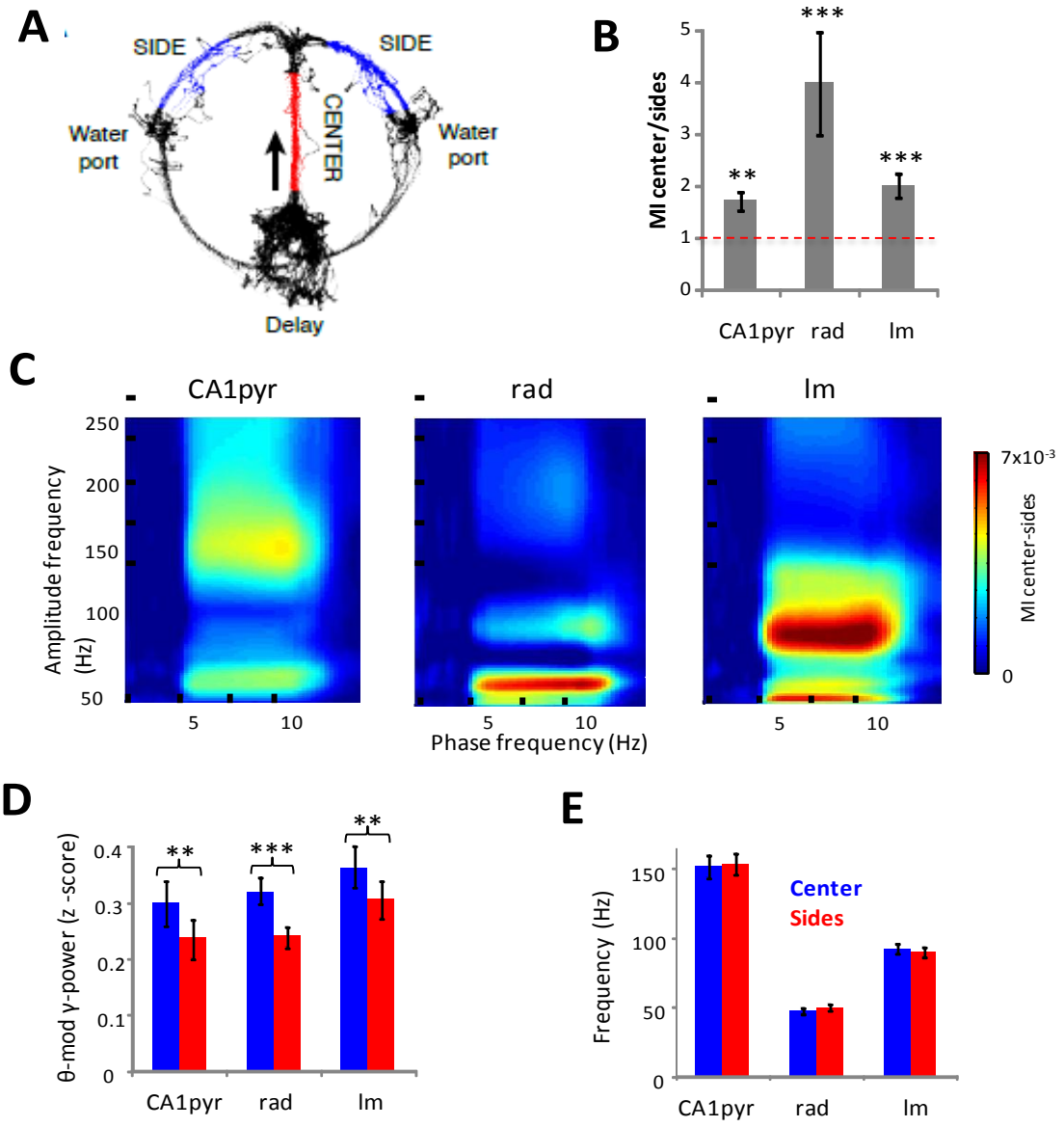

Figure 3.21: **A**: Example running trajectories during one session of a hippocampus-dependent delayed alternation T-maze task. Colors indicate sections choose to compare LFP and unit activity during center arm running (CENTER, red) to running in side arms (SIDE, blue). **B**: The theta-gamma modulation indices (MI) for CA1 ICs were significantly greater during CENTER running compared to SIDE (t-test, n = 3 rats). **C**: Differences in the theta modulation of the gamma power of each IC showed that the strongest changes were at the gamma frequencies characteristic of each afferent pathway (compare Figure 3.2.2A). **D**: Z-score-normalized power of each CA1 IC at the frequencies of strongest theta modulation were significantly greater during CENTER (red) running compared to SIDE (blue)(t-test; 3 rats). Changes were stronger for *rad* gamma_S. **E**: Mean frequency of the three ICs did not significantly change between CENTER and SIDE running ($p > 0.05$; 3 rats). Modified from Schomburg, Fernández-Ruiz et al., 2014.

We compared the spectral activity of each of the three main CA1 LFPs ICs (*CA1pyr*, *radiatum* and *lac-mol*) while the rats were running in the central arm versus while they were running in the side arms. Only theta periods were included in the analysis and was checked that the velocity of the animal was not significantly different ($p > 0.5$ t-test) for the selected periods in each arm. Both theta-gamma coupling (Figure 3.21B) and gamma power (Figure 3.21D) were significantly stronger for each CA1 IC during center arm running, compared to the side arm with the largest changes present in CA1 str. radiatum ($p < 0.001$, t-test). These behavior-related changes were specific to the gamma sub-bands that dominate the respective ICs during theta: $gamma_F$ (120-180 Hz) for CA1pyr, $gamma_S$ (30-60 Hz) for radiatum and $gamma_M$ (60-100 Hz) for lac-mol (Figure 3.14C). These results indicate that theta-gamma coupling in the hippocampus is selectively enhanced during memory recall.

Theta-gamma analysis indicates that both CA3 and EC3 inputs are recruited during the recall phase of the task, although the CA3 input seems to be preferentially enhanced, as reflected by the largest increase in radiatum $gamma_S$. To further investigate if there is a predominance of CA3 input over the EC3 we checked the firing of the cells in the input and target regions in three additional animals with simultaneous hippocampus and entorhinal recordings, performing the same task in a slightly different maze (Figure 3.21A). We aggregated spikes from each neuron type within each session to compare overall firing rates, because place-specific firing of hippocampal pyramidal cells would confound single unit comparisons of firing rates between arms (O'Keefe and Nadel, 1978).CA3 pyramidal cell and CA1interneuron firing rates were significantly greater during center arm running compared to side arms ($p < 0.01$ for CA3 pyramidal cells, $p < 0.05$ for CA1 interneurons, t- test on center/side ratios; Figure 3.21B). Although CA1 pyramidal cell firing rates were not significantly changed in the side arms compared to the center ($p > 0.5$ t-test, Figure 3.21B) they showed a significantly greater probability of firing at the theta peak, the preferred phase of EC3 input (Figure 3.21C, first panel). CA3 and EC3 pyramidal cells maintain their theta-phase preference constant in the center and side arms, the descending theta phase for the formers and the theta peak for the latter (Figure 3.21C, second and third panels). Together with the increased firing of CA3 pyramidal cells in the central arm, this last result also pointed to an enhanced control of CA1 dynamics by CA3 input during memory recall.

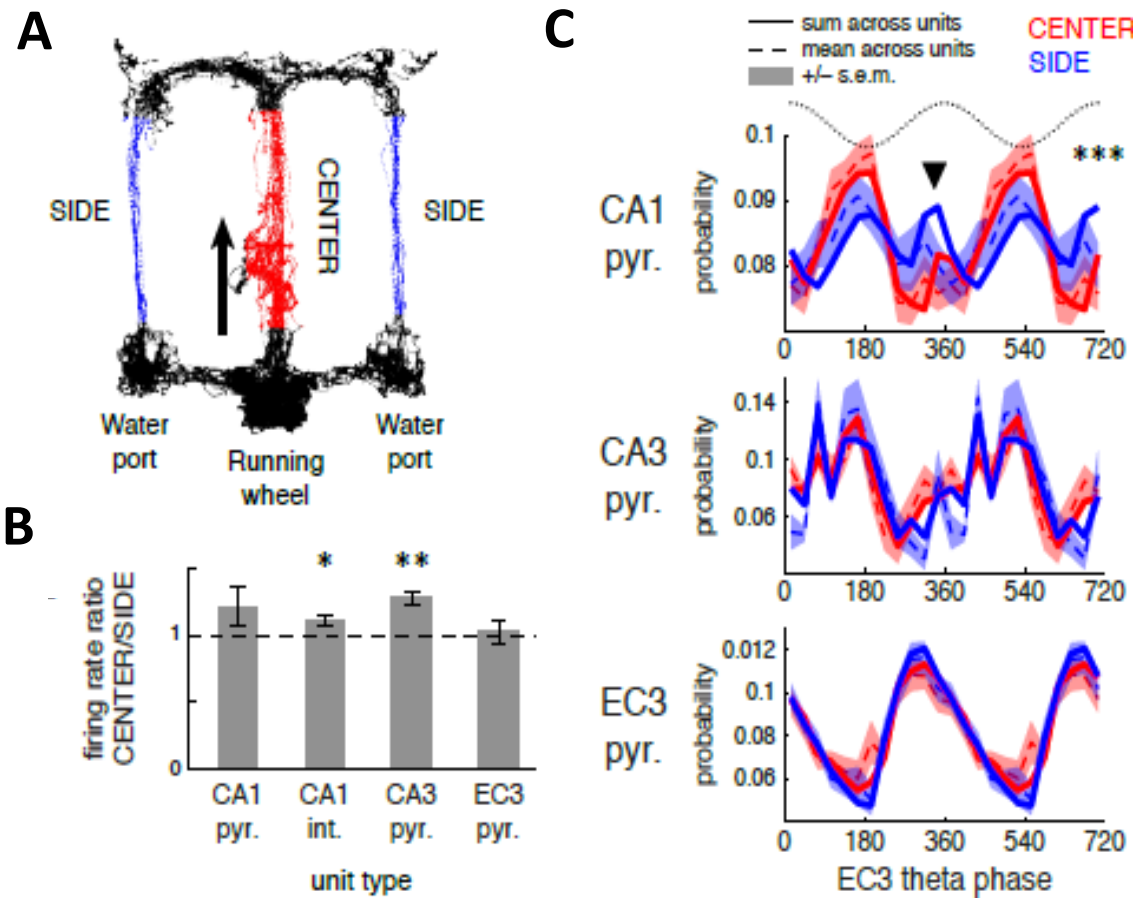

Figure 3.22: **A**: Example trajectories during one session of a similar delayed alternation task with wheel running during the delay period (Pastalkova et al., 2008), which was performed by the animals used in the unit analyses. **B**: Population firing rate ratios within individual sessions revealed that the CA3 pyramidal cells were significantly more active during CENTER running compared to SIDE (t-test). CA1 interneurons also fired at significantly greater rates in CENTER. Across sessions, the measured CA1 and EC3 pyramidal cell population rates were not consistently different in CENTER versus SIDE running ($p > 0.05$). **C**: Theta phase (EC3 phase reference) distribution of spiking in CA1 (top), CA3 (middle), and EC3 (bottom) pyramidal cell populations during CENTER to SIDE running. Lines show the distribution when spike phases were summed across all clustered pyramidal cells, dashed lines (shading) show mean (±SEM) across single units firing > 30 spikes during CENTER and SIDE epochs. Significance thresholds: */**/***$p < 0.05/0.01/0.001$. Reproduced from Schomburg, Fernández-Ruiz et al., 2014.

Overall, these experiments demonstrate that the changing balance of CA3 and EC3 inputs during different phases of a hippocampus-dependent memory task can affect the theta-organization of both gamma activity and spiking in CA1.

4. Discussion

4.1. Methodological challenges in the study of brain oscillations

The study of brain oscillations is a rapidly expanding field. In recent years that it has been boosted by the development of new technologies to perform large-scale recordings and manipulations of brain activity in intact organisms. The increased volume and complexity of data typically obtained in a Systems Neuroscience experiment performed with recent methods poses an important challenge for their analysis and interpretation. From our point of view, the development of novel analytical approaches has been lagging behind the technical development in this field. For this reasons one of the main goals of the present work has been to explore new methodological approaches to the analysis of neural circuit function and in particular brain oscillations.

Brain oscillations appeared well-suited for application of spectral analysis in order to quantify temporal patterns (Fourier analysis and its derivatives; Jenkins and Watts, 1968; Oppenheim and Schafer, 1989). Bioelectrical signals are usually filtered in pre- defined frequency bands of interest, a process that, it must be remembered, leads to the loss of a considerable amount of information. Such a jump from the time to the frequency domain summarizes temporal information and makes it handy to associate and compare with other measurements of a brain activity. Some paradigmatic cases are the identification of phases in the sleep cycle by their spectral content (Dement and Kleitman, 1957), the predictive character of hippocampal theta in terms of behavioral performance (Buzsáki et al., 1983; Whishaw and Varderwolf, 1973), or the processing of visual stimuli contingent with cortical gamma activity (Gray et al., 1989). Importantly, whether oscillatory or irregular, LFPs are complex signals that vary not only in time but also in space, as they are raised by uneven summation of currents originated in different sites, in many cases even with the contribution of different oscillatory generators. All too frequently band-restricted oscillations are thought of and handled as if they were independent from each other, under the reductionist assumption that each constitutes a separate physiological entity. An increasing number of reports are now appearing in the literature challenging, questioning or simply describing inconsistent frequency bands in different or even the same brain areas (Florian et al., 1998; Csicsvari et al., 2003; Schmidt et al., 2009; Ray and

Maunsell, 2011). One notable example is the open dispute regarding the physiological role of gamma activity as a temporal reference frame bringing together different features of a visual stimulus (Singer and Gray, 1995; Fries et al., 2007). Recent results challenge this view, arguing that visual stimuli generate gamma activity at different frequencies in subregions of the visual cortex (Ray and Maunsell, 2010). Others even questioned their very existence, alleging that the spectral properties of the activity recorded are indistinguishable from filtered noise (Burns and Xing, 2011). We are moving away from the old view of frequency bands as behavioral or cognitive flags. We now admit that LFP oscillations are highly variable over time and they have a flexible spectrum (Rivas et al., 1996; Bullock et al., 2003; Ray and Maunsell, 2010). However, it is uncertain what this means in terms of the afferent and target populations. For instance, oscillatory 40–50Hz patterns in the visual cortex (Gray et al., 1989) or the hippocampus (Csicsvari et al., 2003; Bragin et al., 1995; Fernández-Ruiz et al., 2012a) are probably unrelated phenomena with different cellular mechanisms and having distinct computational meaning within their respective networks. On the other hand, the activity of a population of neurons undergoes variable frequency modulation, even during the same behavioral state (Reich et al., 1997; Czurkó et al., 1999; Chang et al., 2012) and hence, the temporal structure of the synaptic currents they originate in target neurons would be expected to change accordingly. Indeed, when changes of spectral power of LFPs are interpreted, it becomes evident that there is insufficient knowledge on the scaling of unitary to macroscopic activities.

The problems described above are harder to solve for recordings obtained with non-invasive techniques due to the inherent difficulties in identifying deep generators (Gloor, 1985; Baillet et al., 2001; Srinivasan et al., 2006). Even when recording at the physical location of the generating sources (e.g. LFP recordings), there is significant uncertainty. We can emphasize the dimension of the problem by considering a non-exhaustive list of possible causes that could lead to increased gamma power: (1) increased gamma-modulated excitation, (2) inhibition (3), or both; (4) the enhanced driving force of an unchanged rhythmic input by sustained changes in another input to the same neurons; (5) variations in phase-locking of presynaptic neurons or (6) in the number of units recruited to firing; (7) reduction of a concomitant antiphase rhythm near the recording electrode; (8) the powering of a different in-phase generator or (9) the addition of new ones; (10) variation in resonant intrinsic currents, and so on. The possibilities are many, some of a cellular origin and others network based.

These issues stress the importance of identifying the population/s contributing to a given field potential oscillation as a necessary step to infer on its physiological and computational meaning.

The problem of identifying the cellular origin of field oscillations, or the inverse problem as it has become known, is a fundamental issue in Systems Neuroscience. In simple terms, given an experimental macroscopic signal the amplitude of which varies at different sites (e.g., LFP, EEG, MEG), how can the location and extension of the generating source be determined? We know from theory that multiple combinations of independent sources (groups of active neurons) may give rise to a recorded signal with the same spatial pattern. There is no unique solution and in most cases, it is extremely difficult to confirm the potential solutions experimentally.

A common feature of electric fields in the brain is that they vary spatially in a complex manner, on account of the shifting activation of neuron generators with irregular morphology and distribution . The problem arises when several synaptic inputs are co-activated, as is usually the case. In such circumstances the electric currents mix unevenly at different sites, and electric potential gradients become complex and variable. Thus, only high-density recordings simultaneously performed at several depths can correctly map for spatial variations in LFP patterns originated by modulations in one or more of the contributing sources. Multisite linear recordings are well-suited to a method that has been employed to find the current generators underlying field potentials, known as current source density (CSD) analysis (Freeman and Nicholson, 1975). This approach has been very useful to determine the contributing cells and the location of synaptic membranes activated by afferent stimuli in laminar structures, such as the hippocampus or neocortex (Leung, 1979; Schroeder et al., 1998). However, while interpreting CSD maps is simple for voltage profiles elicited by stimulating only one afferent pathway their application to ongoing LFPs renders complex spatial maps, and in general it is not feasible to identify the multiple synaptic generators. Partial success has been obtained in a few stereotypic LFP patterns, such as sharp-waves (SPWs: Ylinen et al., 1995), or the theta (Brankack et al., 1993) and gamma rhythms (Csicsvari et al., 2003) in the hippocampus.

4.2. A novel approach to the study of brain oscillations

Amongst the approaches used to address the mixed contribution of inputs to macroscopic patterns, some sought the selective manipulation of parts of a network, such as the activation or the silencing of specific pathways or neuron types through electrical, optogenetic, or pharmacological intervention (Wu et al., 1998; Happel et al., 2010; Kuki et al., 2012). Other approaches pursued the disentanglement of LFPs into their original generators by applying statistical tools and algorithms (Di et al., 1990; Kocsis et al., 1999; Montgomery et al., 2009; Einevoll et al., 2007). Blind source separation techniques, like the independent component analysis (ICA: Comon, 1994; Choi et al., 2005), appear to be the best suited by their capacity to find stable groups of sensors picking up a signal whose origin is stationary in the space, a feature that can be assumed for electrical fields generated by synaptic currents. We have developed an implementation based on the ICA of depth profiles of LFP followed by CSD analysis of the ICs to separate the different synaptic pathways converging on hippocampal principal cells on the evidence that each produces field potentials of stable and distinct spatial distribution (Fernández-Ruiz et al., 2012a; Fernández-Ruiz and Herreras, 2013). Applying this method to two-dimensional LFP recordings in the hippocampus we were able separate their physiologically meaningful sources and match them with known anatomical pathways and its dendritic domains. Due to the parallel arrangement of principal cells bodies and dendrites in the hippocampus and the stratification of the synaptic inputs, the application of ICA and the interpretation of the resulting ICs are particularly simple. However it has some limitations like only those synaptic inputs with enough postsynaptic current, synchrony, and spatial clustering can be detected and separated by ICA; thus, very weak or sparse currents are not easily discernible.

Temporal and spectral characteristics of the wide-band ICs can be analyzed. We thus can detect arbitrary frequency restricted oscillatory patterns without necessary imposing a previous narrow- band filter to the LFP. Another advantage is that the use of pathway-specific ICs reduced the concern of a particular LFP pattern to be a mixture of several inputs, allowing a more accurate interpretation of oscillations in terms of their underlying mechanisms.

We have also employed in this work an innovative methodology to simulate LFPs at a mesoscopic scale. It consists in explicitly modelling the geometry of the tissue, simulating neurons as current sources whose weight and temporal activation was taken from experimental

measures and solving the electromagnetic differential equations to calculate electric fields and potentials with FEM. Despite its simplicity, the model was able to reproduce with high accuracy the characteristics of experimentally recorded hippocampal LFPs. The experimental data necessary to correctly implement the model was only available by the use multielectrode recordings and the ability of ICA to render spatial loadings and temporal activations of LFP sources (that is, to solve the inverse problem of LFPs). Previous approaches used realistic connectivity and/or membrane electrogenesis to explore the intracellular factors and population dynamics that produce significant amount of transmembrane currents (e.g., Pauluis et al., 1999; Linden et al, 2011; Schomburg et al., 2013). The advantage of the FEM approach is that explicit modeling of the population's architecture and the conducting volume allows investigating whether or not these currents build macroscopic LFPs.The FEM approach is widely used in MEG and scalp EEG (Chen and Mogul 2009; Salvador et al., 2011; Thielscher et al. 2011), but to our knowledge this has not been used before in LFP studies. In preliminary work we checked that FEM performs as efficiently as customary compartmental single-cell models scaled up to the population level to reproduce LFPs, while FEM renders important economy of computing resources.

The present results call the attention to the widespread notion that LFPs always refer to highly localized activity elicited by neurons near the electrode. Despite recent reports emphasizing the extremely local reach of LFPs in the cortex (Katzner et al., 2009; Xing et al., 2009) our results show that volume-conducted fields can reach high amplitude far away of their source, in agreement with previous experimental findings (Wang et al., 2005; Kreiman et al., 2006; Berens et al., 2008; Kajikawa and Schroeder 2011). The present work highlights the importance of tissue geometry in the spreading of field potentials. Thus, the question of the spatial reach of LFPs will not have a unique answer; it will depend on the particular architecture of the region where they are recorded as well as the synchrony of the presynaptic neurons. These factors cannot be properly investigated without realistic modelling of spatial factors, which turn to be essential to understand and interpret LFPs.

The conclusion drawn in this work could be potentially applicable to LFPs generated in other structures with similar geometrical characteristics. That is the case of cortical sulcus in humans and other mammals in which cortical layers bend to form giri and sulci. Inside a cortical

sulcus the situation would be similar than in the hilus, with layers of principal cells (the LFP generating elements) facing each other. As a consequence we could extrapolate the present results to this situation and predict that in the case in which both walls of a cortical sulcus are synchronously activated by a common input, or by different ones that elicit opposite polarity dipoles in both walls, LFPs generated inside the sulcus will be of very high amplitude. LFPs in the cortex are in general of lower amplitude than in the hippocampus due to the dispersion of cell bodies in comparison with the densely packed cellular layers in hippocampus, which leads to a partial cancellation of extracellular currents. Despite this difference, which will lead to important quantitative alterations in LFPs magnitude, it seems plausible that the same geometrical and dynamical factors that we have shown, determine the characteristics of hilar LFPs will rule also for potentials inside cortical sulci. These considerations may have special importance for MEG, due to fact that the principal contributors to MEG signals are the neurons located with their main axis perpendicular to the cortical surface, which are mainly those situated in the sulci (Malmivuo and Plonsey, 1995; Nunez and Srinivasan, 2006).

4.3. Geometric and dynamical factors shape extracellular potentials in the Dentate Gyrus

Geometrical factors are usually not considered when modelling LFPs despite that their importance has been repeatedly highlighted by theoretical studies (Gloor, 1985; Nunez and Srinivasan, 2006; Malmivuo and Plonsey, 1995). This assumption seems acceptable in mainly laminar structures, as hippocampal CA1, but we have shown here that is not valid in structures with strong tissue curvatures, as the DG. We mapped LFPs along the dorsoventral and transversal axis of DG, both experimentally in behaving animals and in FEM simulations. We showed that the U-shaped spatial configuration of the GC population favors the spatial clustering of volume-propagated currents away from their physical origin. This projection of synaptic activity to distant sites results in increased activity within highly restricted spatial limits, reaching levels several fold higher than those observed at local sites, albeit with notable heterogeneity. Moreover, the corresponding anatomical pathways must project to both blades of the DG, as even a minimal loss of spatial synchronization leads to a dramatic reduction in LFP power. Our experimental data fulfill several predictions generated by our model, helping to

explain why large LFPs recorded away from the source arise from spatially extended synchronous activation in populations with suitable cytoarchitecture.

Activation of only one blade effectively converted the DG into a planar single-layer structure. Consequently, the LFP power in the hilus dramatically decreased to values similar to those observed in synaptic layers. Coherent activation in mirroring cell layers and/or in a strongly curved single layer is therefore necessary and sufficient to produce the abnormally sized LFPs observed in the hilus. We also demonstrate that the positive polarity of LFPs can only be achieved by somatic inhibition or dendritic excitation. These conditions are only fulfilled by some natural inputs, *e.g.,* the excitatory fibers from the medial and lateral entorhinal cortices and the basket-cell somatic inhibition (Amaral et al., 2007). In the former case, the bifurcation of perforant path axons innervating the GC population in both blades ensures near synchronous activation of extended GC regions. The spatial coherence of inhibitory LFPs is most likely brought about by the merging of individual synaptic territories into larger spatial modules through correlated fluctuations of activity in a homogeneous subpopulation of interneurons (Whittington et al., 1995; Ho et al., 2012). Different classes of interneurons project into the GC soma (basket cell types) and each of dendritic strata associated with either MPP or LPP inputs (hilar interneurons: Han et al., 1995; Houser, 2007). Accordingly, it seems plausible that only the former subpopulation fires with sufficient coherence to notably contribute to hilar LFPs, as implied by the generation of negative hilar LFPs following dendritic inhibition in our model.

The present results shed light on specific parameters that should be considered when interpreting LFPs and their association with concomitant spike activity. For instance, because the spatial coherence of LFPs may be due to macroscopic blending of non-overlapping synaptic territories of functionally coupled neurons (*e.g.*, interneuron networks), it is possible that state-dependent modulation of network coupling disproportionately reduces the visualization of their associated LFPs with respect to individual firing rates, as demonstrated here by reducing the size of the activation strips. These observations are relevant to the study of the cellular mechanisms underlying LFP phenomena including dentate spikes, sharp waves, ripples, and gamma oscillations, which can appear at different hippocampal loci and with varying degrees of spatial coverage (Bragin et al., 1995; Csicsvari et al., 2000; Bibbig et al., 2007; Csicsvari et al., 2003; Ylinen et al., 1995).

4.4. Theta-gamma dynamics reveals network computations during behaviour

The results presented in the third section of the Results demonstrate that low frequency gamma oscillations link together the CA3-CA1 regions and that the strength of this relationship is strongest during memory recall, associated with increased theta coupled $gamma_S$ power and a shift of preferred spike theta phase from the peak to near the trough in a fraction of CA1 pyramidal cells. A distinct and higher frequency gamma pattern ($gamma_M$) is dominant near the peak of the theta cycle, coincident with increased firing of EC3 pyramidal neurons and their excitation of the distal apical dendrites of CA1 pyramidal cells (current sink). Gamma coherence is high within the same dendritic layer but low across layers. During REM sleep CA3 spiking output and the associated $gamma_S$ in CA1 str. radiatum are decreased, accompanied by an increased EC3 spiking and elevated $gamma_M$ power in str. lacunosum-moleculare.

Our findings support previous observations that $gamma_S$ oscillations occur on the descending phase of theta in the CA1 pyramidal layer, brought about by the gamma-timed spiking of CA3 pyramidal cells (Csicsvari et al., 2003; Colgin et al., 2009; Fernández-Ruiz et al., 2012; Lasztoczy and Klausberger, 2014). However, they are at variance with the postulated theta phase assignment of EC3-mediated gamma bursts by Colgin et al. (2009). In the latter study, the authors suggested that the CA3-driven $gamma_S$ is *followed* by an EC input-driven faster gamma burst in the 65-140 Hz range at the trough of the theta cycle (Colgin et al., 2009). One potential source of the conflicting results is the use of single site recordings in the Colgin et al. study, which is not sufficient to decompose the spatial origin of the respective gamma generators (Buzsaki et al., 2012; Einevoll et al., 2013; Fernández-Ruiz and Herreras, 2013; Lasztóczi and Klausberger, 2014). Because the main generators of LFPs are often postsynapic currents, a single oscillating population may generate coherent LFPs in distant areas without necessarily entraining the downstream population. Although the authors showed phase coupling between entorhinal unit firing and the lumped $gamma_M$ and $gamma_F$ band LFPs in the CA1 pyramidal layer, they did not report the theta phase of either spiking or gamma activity in EC3. In contrast to the framework put forward by Colgin et al. (2009), we find that the peak firing of EC3 pyramidal cells and the associated current sink in the CA1 str. lacunosum-moleculare occurs, on average, at the peak of the theta cycle (Buzsaki et al., 1986; Brankack et al., 1993; Kamondi et al., 1998; Montgomery et al., 2009; Mizuseki et al., 2009; Benito et al., 2013), coincident with the $gamma_M$ burst and, thus, *before* the dominant CA3-mediated $gamma_S$ on the descending phase of

theta.

The differential firing rate changes of CA3 and EC3 principal cell can account for the CA1 firing patterns and gamma oscillations, we observed both across brain states and in the T-maze task. These two major inputs can either compete or cooperate depending on the nature of the task (Dvorak-Carbone and Schuman, 1999a, 1999b; Remondes and Schuman, 2002; Jarsky et al., 2005; Leao et al., 2012; Chance, 2012; Basu et al., 2013). The EC3 input may become more effective through theta-rhythmic frequency potentiation by suppressing feed-forward inhibition (Buzsaki 1995; Yeckel and Berger, 1990; Leao et al., 2012) or facilitating mechanisms for overcoming it (Remondes and Schuman, 2002; Jarsky et al., 2005; Takahashi and Magee, 2009). Furthermore, during REM sleep, firing rates of CA3 pyramidal neurons decrease (Montgomery et al, 2008; Mizuseki and Buzsáki, 2013), paralleled with the reduced power of $gamma_S$ in CA1 str. radiatum and decreased spike-field CA3-CA1 coherence (Schomburg, Fernández-Ruiz et al., 2014). This reduced CA3 output coincides with an increased firing of EC3 neurons and elevated $gamma_M$ power in the str. lacunosum-moleculare and the shifting of theta phase preference of a significant fraction of CA1 pyramidal neurons from the trough to the peak (Poe et al., 2000; Mizuseki et al., 2011). Thus, a weakened CA3 output leads to a relatively stronger control of the EC3 input on the discharge of CA1 neurons, as was also observed in the side arms of the T-maze task, where demands on memory retrieval are diminished.

An increased gain control over CA1 neurons by the direct EC3 input can explain why after lesion of the CA3 input, place-related firing of CA1 pyramidal cells can persist (Brun et al., 2008).The shift in gain control can also explain why spatial information encoded by CA1 pyramidal cells varies as a function of their position in the proximodistal axis (Henriksen et al., 2010) and why during recall the CA3 input shows increased control over CA1 activity patterns (Montgomery and Buzsaki, 2007). One potential substrate of the CA3-EC3 competition is the O-LM to bistratified interneuron inhibitory connection. Increased firing of O-LM interneurons near the theta trough (Klausberger et al., 2003; Varga et al., 2012) suppresses inputs to the distal dendrites, whereas itindirectly disinhibits dendritic segments in str. oriens and radiatum (Leao et al., 2012), thereby facilitating the effectiveness of the CA3 input to CA1 pyramidal cells.

During encoding of newly learned information, EC input is expected to boost the efficacy of the CA3-CA1 pathway (Hasselmo and Wyble, 1997; Remondes and Schuman, 2002, 2004).

Indeed, in vitro experiments have demonstrated that pairing temporo-ammonic (EC3 to CA1) and Schaffer collateral excitation to CA1 can multiplicatively induce long-term potentiation and CA1 spiking via dendritic plateau potentials and heterosynaptic effects, depending on the relative frequency and timing of these inputs (Buzsaki 1995; Dudman et al., 2007; Golding et al., 2002; Han and Heinemann, 2013; Levy et al., 1998; Remondes and Schuman, 2002; Takahashi and Magee, 2009; Wohrl et al., 2007; Steffenach et al., 2005; Suh et al., 2011; Basu et al., 2013; but see Ang et al., 2005). The strongest potentiation is observed when the distal dendrites are excited 10-30 msec prior to the arrival of the CA3 input, matching the roughly one quarter theta cycle delay between the occurrence of $gamma_M$ and $gamma_S$ in CA1. The heterosynaptic boosting effect of the entorhinal input can be selectively suppressed by perisomatic inhibition mediated by cholecystokinin (CCK)-expressing interneurons (Basu et al., 2013). Our findings demonstrate that the timing of these spike level interactions can be monitored by the mesoscopic changes of the LFP theta-gamma oscillations. Additional experiments are required to disentangle the roles of the medial and lateral entorhinal cortical inputs (Igarashi et al., 2014) and the thalamic nucleus reuniens (Vertes, 2007) in the expression of gamma in the str. lacunosum-moleculare.

Overall, our experiments demonstrate that layer-specific gamma oscillations in the hippocampus reliably identify the temporal dynamics of the afferent inputs and that temporal coordination in the entorhinal-hippocampal system is mainly supported by theta and low frequency gamma oscillations, but not by high gamma coherence (Schomburg, Fernández-Ruiz et al., 2014).

Conclusions

We have implemented a novel method to the study of LFPs and applied it to hippocampal recordings from behaving rats. The first important conclusion we get from this work is that for a correct analysis and interpretation of LFPs it is necessary an appropriated spatial mapping of the structure of interest. Due to the propagation of electric potentials in the brain tissue, single point recordings, as traditionally performed with tetrodes or wire electrodes, are not able to discern the origin (local, propagated, mixed) of the recorded LFPs. On the contrary, high-density two-dimensional recordings, as those presented here, are optimal because they account for the spatial variations of LFPs in laminated structures such as the hippocampus or neocortex.

We employed ICA to decompose hippocampal LFPs recorded along the dorsoventral and transversal axes of the hippocampus into six main contributing sources (independent components, ICs). Those sources display distinct laminar distribution and their CSD maps reveal main currents restricted to particular sub-layers, allowing us to identify their synaptic nature comparing with known anatomical synaptic domains. The three main CA1 ICs were identified as the ipsilateral CA3 input to the str. radiatum dendrites (*rad* IC), the entorhinal cortex layer 3 input to the str. lacunosum-moleculare dendrites (*lm* IC) and perisomatic currents, likely inhibitory, in the CA1 pyramidal cell bodies (*CA1pyr* IC). In the DG they were identified as the lateral perforant path input to the distal GC dendrites (*LPP* IC), the medial perforant path input to the middle GC dendrites (*MPP* IC), and perisomatic currents in the GC somas, likely inhibitory, (*GCsom*). However, a more rigorous identification of those ICs as strictly pathway-specific or as a mixture of different inputs with shared dendritic domains would require additional tests, like selective optogenetic manipulations in well-defined cellular populations. This is especially relevant for the *CApyr* and *GCsom* components, which likely capture currents elicited by somatic action potentials in addition to postsynaptic currents.

Simulations performed with FEM in the tridimensional model of the hippocampus reproduce with high fidelity the spatial distribution of the different hippocampal current sources. The simultaneous activation of the six sources with time series obtained from experimental recordings allows us to reproduce the laminar characteristics of SWR and theta oscillations.

These results confirm the accuracy of our solution for the inverse problem of hippocampal LFPs and that those six sources are enough to account for most of the variability of the recorded LFPs in the CA1 and DG regions. We have decided not to include here other results pertaining to the CA3 were another prominent IC can be isolated (Benito, Fernández-Ruiz et al., 2014; Schomburg, Fernández-Ruiz et al., 2014).

The above results illustrate the usefulness of our novel method to analyze LFPs. It consists in first extract and identify the current sources contributing to their generation and then implement the obtained solution in a model that allows the forward simulation of LFPs. By comparing the original and simulated LFPs we can refine and better interpret our original solution.

We employed the model and knowledge gained about the spatiotemporal dynamics of LFP sources to study the generation of DG potentials. In particular we were interested in explaining the apparent paradox that the hilus, which mainly lacks cellular elements capable of generating large currents, is where LFPs are larger, plus the fact that they have positive polarity even though the main assumption is that they are elicited by the excitatory perforant pathway inputs. We found that is the particular U-shaped geometry of the DG which favors the spatial clustering of volume propagated currents away from their synaptic origin. We also found that the positive polarity in the hilus can only be produced by either somatic inhibition or dendritic excitation. The simulations make several predictions that match with our and others experimental observations. Only some anatomical inputs (i.e. the MPP and LPP distal dendritic excitations and basket-cell type perisomatic inhibition) but not others (i.e. the mossy cells proximal dendritic excitation and hilar interneurons distal dendritic inhibition) have significant contribution to DG LFP patterns. The type of synaptic activation that best explain the characteristics of recorded LFPs according to our simulations is a synchronous input to extended domains of GC in both blades. Of particular importance is the fact that the activation of mirror modules in both DG blades must be simultaneous in order to elicit large potentials in the hilus due to the activation of dipoles with opposite polarity.

Those results illustrate the often neglected importance of geometrical and spatial factors in the shape of extracellular potentials and highlight the utility of macroscopic models based on experimental data to reach a deeper understanding of the underlying mechanism of LFPs.

In the last section of this thesis, we employed the acquired knowledge about the sources of hippocampal LFPs to address the study of theta-gamma interactions in the hippocampal-entorhinal circuit during behaviour. We found that the three main LFP sources characterized in the first section of the Results display different spectral profiles in the gamma band and theta-phase preference. Slow gamma ($gamma_S$, 30-60 Hz) was elicited by the CA3 input to the CA1 and peaked on the descending theta phase, while mid-frequency gamma ($gamma_M$, 60-120 Hz) brought about by entorhinal layer 3 input dominated on the peak of the theta cycle. A third source of very fast oscillations ($gamma_F$, 100-180 Hz) peaked on the theta trough and was of local origin. The preferred phase of *rad* slow gamma was shared by similar frequency oscillations in the input region, CA3, and was also the theta-phase with higher probability of firing of CA3 pyramidal cells. Correspondingly, the preferred phase of *lm* $gamma_M$ was shared by similar frequency gamma oscillations in the layer 3 of the medial entorhinal cortex and was also the theta phase with higher probability of discharge of EC3 pyramidal cells. Those theta-coupled gamma oscillations were present in both exploration and REM sleep albeit with different strength. Theta-coupled gamma oscillations not only vary as a function of behavioral state but also with the location along the CA1 transversal axis. CA3 $gamma_S$ was stronger during running and dominated at proximal sites, while $gamma_M$ was stronger during REM and dominated at distal CA1 sites. Perisomatic $gamma_F$ oscillations varied in their proximodistal distribution and theta-phase preference as a function of brain state according to which $gamma_S$ or $gamma_M$ was the dominant pattern. This illustrates a competition of CA3 and entorhinal inputs to control CA1 local circuits operation.

We also checked theta-gamma dynamics in CA1 during memory guided navigation (a delayed-alternation T maze task known to relay on the hippocampus). We found that during the recall phase of the task (the central arm running) theta-gamma coupling increased for all the ICs but especially for the *rad* $gamma_S$. In addition, during this phase the firing rate of CA3 pyramidal cells was increased. On the contrary, at the encoding phase of the task (side arms running) CA3 firing rates were lower and a subset of CA1 pyramidal cells shift their theta phase preference to the theta peak, the phase of the EC3 input. Those results demonstrate that CA3 and EC3 inputs can compete or cooperate to control the firing of CA1 cells according to behavioral demands.

Appendix A: Publications list of the author

Schomburg EW*, **Fernández-Ruiz A*,** Berényi A, Mizuseki K, Anastassiou CA, Koch C, Buzsáki G. (2014) *Theta phase segregation of input-specific gamma patterns in entorhinal-hippocampal networks.* Neuron. 84:470-485. (* co-first authors).

Benito N*****, **Fernandez-Ruiz A***, Makarov VA, Makarova J, Korovaichuk A, Herreras O. (2014) *Spatial blocks of coherent pathway-specific LFPs in the hippocampus reflect different modes of presynaptic synchronization*. Cereb Cortex.24:1738-52. (*co-first authors).

Enriquez-Barreto L, Cuesto G, Dominguez-Iturza N, Gavilán E, Ruano D, Sandi C, **Fernández-Ruiz A**, Martín-Vázquez G, Herreras O, Morales M. (2014) *Learning improvement after PI3K activation correlates with de novo formation of functional small spines.* Front Mol Neurosci 2;6:54.

Fernández-Ruiz A*, Schomburg EW*. (2013) *The rules of entrainment: are CA1 gamma oscillations externally imposed or locally governed?* J Neurosci 33:19045-19047, (*co-first authors).

Fernandez-Ruiz A, Muñoz S, Sancho M, Makarov VA, Herreras O. (2013) *Cytoarchitectonic and dynamic origins of giant positive LFPs in the Dentate Gyrus.* J Neurosci 33:15518-15532.

Fernández-Ruiz A, Herreras O. (2013*) Identifying the synaptic origin of ongoing neuronal oscillations through spatial discrimination of electric fields*. Front Comput Neurosci 7:5.

Fernandez-Ruiz A, Makarov VA, Herreras O. (2012) *Sustained increase of spontaneous input and spike transfer in the CA3-CA1 following long-term potentiation in vivo.* Front Neural Circuits 6:71.

Fernandez-Ruiz A, Makarov VA, Benito N, Herreras O. (2012) *Schaffer-specific local field potentials reflect discrete excitatory events at gamma-frequency that may fire postsynaptic hippocampal CA1 units.* J Neurosci 32:5165-5176.

Appendix B: Acronyms

CA1/3	*Cornnus Ammoni* 1/3
CFC	Cross Frequency Coupling
CSD	Current Source Density
CWT	Complex Wavelet Transform
DG	Dentate Gyrus
DNQX	6,7-dinitroquinoxaline-2,3-dione
EC	Entorhinal Cortex
EEG	Electroencephalogram
ESPS	Excitatory post-synaptic potential
FEM	Finite Elements Method
GABA	γ-aminobutyric acid
GC	Granular cell
IC	Independent Component
ICA	Independent Component Analysis
IPSP	Inhibitory post-synaptic potential
LEC	Lateral entorhinal cortex
LFP	Local Field Potential
LPP	Lateral Perforant Path
MEC	Medial entorhinal cortex
MI	Modulation index
MPP	Medial Perforant Path
NMDA	N-Methyl-D-aspartic acid or N-Methyl-D-aspartate
SEM	Standard Error of the Mean

References

Abeles M (1991). Corticonics. Cambridge, Cambridge University Press.

Abraham WC, McNaughton N. (1984). Differences in synaptic transmission between medial and lateral components of the perforant path. Brain Res 15;303(2):251-60.

Ainge JA, van der Meer MAA, Langston RF, Wood ER (2007) Exploring the role of context-dependent hippocampal activity in spatial alternation behavior. Hippocampus 17:988–1002

Akam T, Oren I, Mantoan L, Ferenczi E, Kullmann, DM (2012). Oscillatory dynamics in the hippocampus support dentate gyrus–CA3 coupling. Nat Neurosci, 15(5), 763–8.

Alonso A, García-Austt E (1987) Neuronal sources of theta rhythm in the entorhinal cortex of the rat. I. Laminar distribution of theta field potentials. Exp Brain Res 67:493–501

Amaral DG, Scharfman HE, Lavenex P. (2007). The dentate gyrus: fundamental neuroanatomical organization (dentate gyrus for dummies). Prog Brain Res 163, 3-22.

Amaral DG, Witter MP (1989) The three-dimensional organization of the hippocampal formation: a review of anatomical data. Neuroscience 31:571–591

Andersen P, Morris RG, Amaral D, Bliss T, O'Keefe J (2007) The hippocampus book. Oxford University Press. New York.

Baillet S, Mosher JC, Leahy RM (2001) Electromagnetic brain mapping. IEEE Signal. Procces. Mag. 18:14-30.

Basu J, Srinivas KV, Cheung SK, Taniguchi H, Huang ZJ, Siegelbaum SA (2013) A cortico-hippocampal learning rule shapes inhibitory microcircuit activity to enhance hippocampal information flow. Neuron 79:1208–1221

Bédard C, Destexhe A (2011) Generalized theory for current-source-density analysis in brain tissue. Phys Rev E 84 :041909.

Bell AJ, Sejnowski TJ (1995) An information-maximization approach to blind separation and blind deconvolution. Neural Comput 7:1129–1159

Belluscio MA, Mizuseki K, Schmidt R, Kempter R, Buzsáki G (2012) Cross-frequency phase-phase coupling between θ and γ oscillations in the hippocampus. J Neurosci 32:423–435

Benito N, Fernandez-Ruiz A, Makarov VA, Makarova J, Korovaichuk A, Herreras O (2014) Spatial Modules of Coherent Activity in Pathway-Specific LFPs in the Hippocampus Reflect Topology and Different Modes of Presynaptic Synchronization. Cereb Cortex 24:1738-1752

Berens P (2009) CircStat: a MATLAB toolbox for circular statistics. Journal of Statistical Software 31

Bibbig A, Middleton S, Racca C, Gillies MJ, Garner H, Lebeau FE, Davies CH, Whittington MA. (2007) Beta rhythms (15-20 Hz) generated by nonreciprocal communication in hippocampus. J Neurophysiol.97:2812-23.

Bland BH, Oddie SD (2001) Theta band oscillation and synchrony in the hippocampal formation and associated structures: the case for its role in sensorimotor integration. Behav Brain Res 127:119-136.

Bragin A, Jandó G, Nádasdy Z, Hetke J, Wise K, Buzsáki G (1995a) Gamma (40-100 Hz) oscillation in the hippocampus of the behaving rat. J Neurosci 15:47-60

Bragin A, Jandó G, Nádasdy Z, van Landeghem M, Buzsáki G. (1995b) Dentate EEG spikes and associated interneuronal population bursts in the hippocampal hilar region of the rat. J Neurophysiol 73:1691-705.

Brankack J, Stewart M, Fox SE(1993) Current source density analysis of the hippocampal theta rhythm: associated sustained potentials and candidate synaptic generators. Brain Res615:310–327

Brown GD, Yamada S, Sejnowski TJ (2001) Independent component analysis at the neural cocktail party. Trends Neurosci 24:54–6

Brun VH, Leutgeb S, Wu H-Q, Schwarcz R, Witter MP, Moser EI, Moser M-B (2008) Impaired spatial representation in CA1 after lesion of direct input fromentorhinalcortex. Neuron57:290–302.

Brunel N, Wang X (2003) What determines the frequency of fast network oscillations with irregular neural discharges? I. Synaptic dynamics and excitation-inhibition balance. J Neurophysiol 90:415–430.

Bullmore E, Sporns O (2009) Complex brain networks: graph theoretical analysis of structural and functional systems. Nature Reviews Neuroscience 10 (3), 186-198

Bullock TH, Mcclune MC, Enright JT (2003). Are the electroencephalograms mainly rhythmic? Assessment of periodicity in wide-band time series. Neuroscience. 121, 233-252.

Burke SN, Maurer AP, Nematollahi S, Uprety AR, Wallace JL, Barnes CA. (2011) The influence of objects on place field expression and size in distal hippocampal CA1.Hippocampus. 21:783-801.

Burns SP, Xing D (2011). Is gamma-band activity in the local field potential of V1 cortex a " clock " or filtered noise? J. Neurosci. 31, 9658 -9664.

Burwell RD, Witter MP, Amaral DG (1995) Perirhinal and postrhinal cortices of the rat: a review of the neuroanatomical literature and comparison with findings from the monkey brain. Hippocampus. 5:390-408.

Buzsáki G (1984) Feed-forward inhibition in the hippocampal formation. Prog Neurobiol 22:131–153.

Buzsáki G (2002) Theta oscillations in the hippocampus. Neuron 33:325–340.

Buzsáki G (2010) Neural syntax: cell assemblies, synapsembles, and readers. Neuron 68:362–385

Buzsáki G (2015) Hippocampal sharp wave-ripple: A cognitive biomarker for episodic memory and planning. Hippocampus [Epub ahead of print]

Buzsáki G, Anastassiou CA, Koch C (2012) The origin of extracellular fields and currents - EEG, ECoG, LFP and spikes. Nat Rev Neurosci 13:407–420

Buzsáki G, Czopf J, Kondakor I, Kellenyi L (1986) Laminar distribution of hippocampal rhythmic slow activity (RSA) in the behaving rat: current source density analysis, effects of urethane and atropine. Brain Res 365:125–137.

Buzsáki G, Draguhn A (2004) Neuronal oscillations in cortical networks. Science 304:1926–

1929

Buzsáki G, Leung LS, Vanderwolf CH. (1983) Cellular bases of hippocampal EEG in the behaving rat. Brain Res 287: 139-171,

Buzsáki G, Logothetis N, Singer W (2013) Scaling brain size, keeping timing: evolutionary preservation of brain rhythms. Neuron 80:751–764

Buzsáki G, Mizuseki K (2014) The log-dynamic brain: how skewed distributions affect network operations. Nat Rev Neurosci 15:264–278.

Buzsáki G, Moser EI (2013) Memory, navigation and theta rhythm in the hippocampal-entorhinal system. Nature Publishing Group 16:130–138

Buzsáki G, Penttonen M, Bragin A, Nadasdy Z, Chrobak JJ (1995) Possible physiological role of the perforant path-CA1 projection. Hippocampus5:141–146.

Buzsáki G, Wang X-J (2012) Mechanisms of gamma oscillations. Annu Rev Neurosci 35:203-225.

Cabral HO, Vinck M, Fouquet C, Pennartz CMA, Rondi-Reig L, Battaglia FP (2014) Oscillatory Dynamics and Place Field Maps Reflect Hippocampal Ensemble Processing of Sequence and Place Memory under NMDA Receptor Control. Neuron 81:402–415.

Cajal S (1901) Estudios sobre la corteza cerebral humana. IV estructura de la corteza cerebralolfativa del hombre y mamíferos. Trabajos del Lab. Inv Biol. Univ. Madrid 1:1-140

Cajal S (1911) Histologie du Systemenerveux de l'homme et des vertebres. Vol. II Paris Maloine

Canolty RT, Edwards E, Dalal SS, Soltani M, Nagarajan SS, Kirsch HE, Berger MS, Barbaro NM, Knight RT (2006) High Gamma Power Is Phase-Locked to Theta Oscillations in Human Neocortex. Science 313:1626-1628.

Canolty RT, Knight RT (2010) The functional role of cross-frequency coupling. Trends in Cognitive Sciences 14:506-515.

Carr MF, Karlsson MP, Frank LM (2012) Transient slow gamma synchrony underlies hippocampal memory replay. Neuron 75:700–713.

Chang MH, Armstrong KM, Moore T (2012). Dissociation of response variability from firing rate effects in frontal eye field neurons during visual stimulation, working

memory, and attention. J. Neurosci. 32, 2204-2216.

Chen A (2006) Fast kernel density independent component analysis. Lect Notes Comp Sci, Vol. 3889, pp. 24-31.

Chen M and Mogul DJ. (2009) A structurally detailed finite element human head model for simulation of transcranial magnetic stimulation.J Neurosci Meth 179:11-120.

Chen, A and Bickel, PJ (2005) Consistent independent component analysis and prewhitening. IEEE Trans Sig Proc 53: 3625-3632

Choi S, Cichocki A, Park HM, Lee SY (2005) Blind source separation and independent component analysis: a review. NeurInf Process Let Rev 6:1–57

Chrobak JJ, Buzsáki G (1998) Gamma oscillations in the entorhinal cortex of the freely behaving rat. J Neurosci 18:388–398

Colgin LL, Denninger T, Fyhn M, Hafting T, Bonnevie T, Jensen O, Moser M-B, Moser EI (2009) Frequency of gamma oscillations routes flow of information in the hippocampus. Nature 462:353-357.

Comon P (1994) Independent component analysis, a new concept? Sig Proces 36:287–314.

Csicsvari J, Hirase H, Czurko A, Buzsáki G (1998) Reliability and state dependence of pyramidal cell-interneuron synapses in the hippocampus: an ensemble approach in the behaving rat. Neuron 21:179–189

Csicsvari J, Hirase H, Czurkó A, Mamiya A, Buzsáki G (1999) Oscillatory Coupling of Hippocampal Pyramidal Cells and Interneurons in the Behaving Rat. J Neurosci 19:274 - 287.

Csicsvari J, Jamieson B, Wise KD, Buzsáki G (2003) Mechanisms of gamma oscillations in the hippocampus of the behaving rat. Neuron 37:311-322.

Csicsvari J, Hirase H, Mamiya A, Buzsáki G. (2000) Ensemble patterns of hippocampal CA3-CA1 neurons during sharp wave-associated population events. Neuron 28:585-594.

Czurkó A, Hirase H, Csicsvari J, Buzsáki G. (1999). Sustained activation of hippocampal pyramidal cells by 'space clamping' in a running wheel. Eur. J. Neurosci. 11, 344-352.

Delorme A, Makeig S (2004) EEGLAB: an open source toolbox for analysis of single-trial EEG

dynamics including independent component analysis. J Neurosci Methods 134:9–21.

Dement W, Kleitman N (1957). Cyclic variations in EEG during sleep and their relation to eye movements, body motility and dreaming. Electroenceph. Clin. Neurophysiol. 9,673-690.

Di S, Baumgartner C, Barth DS (1990). Laminar analysis of extracellular field potentials in rat vibrissa/barrel cortex. J. Neurophysiol. 63, 832–840.

Diba K, Buzsáki G (2008) Hippocampal network dynamics constrain the time lag between pyramidal cells across modified environments. J Neurosci 28:13448-13456.

Dragoi G, Buzsáki G (2006) Temporal encoding of place sequences by hippocampal cell assemblies. Neuron 50:145–157

Dudman JT, Tsay D, Siegelbaum SA (2007) A role for synaptic inputs at distal dendrites: instructive signals for hippocampal long-term plasticity. Neuron 56:866–879

Dvorak-Carbone H, Schuman EM (1999a) Long-term depression of temporoammonic-CA1 hippocampal synaptic transmission. J Neurophysiol 81:1036–1044

Eichenbaum H (2004) Hippocampus: cognitive processes and neural representations that underlie declarative memory. Neuron 44:109-120.

Einevoll GT, Kayser C, Logothetis NK, Panzeri S (2013) Modelling and analysis of local field potentials for studying the function of cortical circuits. Nat Rev Neurosci 14:770–785

Einevoll GT, Pettersen KH, Devor A, Ulbert I, Halgren E, Dale AM (2007) Laminar population analysis: estimating firing rates and evoked synaptic activity from multielectrode recordings in rat barrel cortex. J Neurophysiol 97:2174–2190

Enriquez-Barreto L, Cuesto G, Dominguez-Iturza N, Gavilán E, Ruano D, Sandi C, Fernández-Ruiz A, Martín-Vázquez G, Herreras O, Morales M. (2014) Learning improvement after PI3K activation correlates with de novo formation of functional small spines. Front Mol Neurosci 2;6:54.

Fell J, Axmacher N (2011) The role of phase synchronization in memory processes. Nat Rev Neurosci 12:105-118.

Fernández-Ruiz A, Herreras O (2013) Identifying the synaptic origin of ongoing neuronal oscillations through spatial discrimination of electric fields. Front Comput Neurosci 7:5.

Fernández-Ruiz A, Makarov VA, Benito N, Herreras O (2012) Schaffer-Specific Local Field Potentials Reflect Discrete Excitatory Events at Gamma Frequency That May Fire Postsynaptic Hippocampal CA1 Units.J Neurosci 32:5165–5176.

Fernández-Ruiz A, Makarov VA, Herreras O (2012b) Sustained increase of spontaneous input and spike transfer in the CA3-CA1 pathway following long-term potentiation in vivo. Front Neural Circuits 6:71.

Fernández-Ruiz A, Muñoz S, Sancho M, Makarova J, Makarov VA, Herreras O (2013) Cytoarchitectonic and DynamicOrigins of Giant Positive Local Field Potentials in the Dentate Gyrus. J Neurosci 33:15518–15532.

Fernández-Ruiz A, Schomburg EW. (2013) The rules of entrainment: are CA1 gamma oscillations externally imposed or locally governed? J Neurosci 33:19045-19047.

Florian G, Andrew C, Pfurtscheller G (1998) Do changes in coherence always reflect changes in functional coupling? Electroencephalogr. Clin. Neurophysiol. 106(1):87-91.

Freund TF, Buzsáki G (1996) Interneurons of the hippocampus. Hippocampus 6:347-470.

Fries P, Nikolic D, and Singer W. (2007) The gamma cycle. Trends Neurosci. 30, 309-316.

Fujisawa S, Amarasingham A, Harrison MT, Buzsáki G (2008) Behavior-dependent short-term assembly dynamics in the medial prefrontal cortex. Nat Neurosci 11:823-833.

Givens B (1996) Stimulus-evoked resetting of the dentate theta rhythm: relation to working memory.Neuroreport 8:159-63.

Glickfeld LL, Roberts JD, Somogyi P, Scanziani M (2009) Interneurons hyperpolarize pyramidal cells along their entire somatodendritic axis. Nat Neurosci 12:21–23

Gloor P (1985) Neuronal generators and the problem of localization in electroencephalography: Application of volume conductor theory to electroencephalography. J. Clin. Neurophysiol. 2, 327-354.

Golding NL, Mickus TJ, Katz Y, Kath WL, Spruston N (2005) Factors mediating powerful voltage attenuation along CA1 pyramidal neuron dendrites. J Physiol 568:69–82

Goutagny R, Jackson J, Williams S (2009) Self-generated theta oscillations in the hippocampus.

Nat Neurosci 12:1491-1493.

Hájos N, Pálhalmi J, Mann EO, Németh B, Paulsen O, Freund TF (2004) Spike Timing of Distinct Types of GABAergic Interneuron during Hippocampal Gamma Oscillations In Vitro. J Neurosci 24:9127-9137.

Hájos N, Paulsen O. (2009) Network mechanisms of gamma oscillations in the CA3 region of the hippocampus. Neural Netw 22:1113-1119.

Hämämälainen M, Hari R, Ilmoniemi RJ, Knuutila J, Lounasmaa OV. (1993) Magnetoenceohalography: theory, instrumentation ans application to non-invasive studies of the wotking human brain. Rev Mod. Phys. 65, 413-497.

Han ZS, Buhl EH, Lörinczi Z, Somogyi P. (1993) A high degree of spatial selectivity in the axonal and dendritic domains of physiologically identified local-circuit neurons in the dentate gyrus of the rat hippocampus. Eur J Neurosci 5:395-410.

Han EB, Heinemann SF (2013) Distal dendritic inputs control neuronal activity by heterosynaptic potentiation of proximal inputs. J Neurosci 33.1314-1325.

Happel MF, Jeschke M, Ohl FW (2010) Spectral integration in primary auditory cortex attributable to temporally precise convergence of thalamocortical and intracortical input. J. Neurosci. 30, 11114-11127.

Hargreaves EL, Rao G, Lee I, Knierim JJ (2005) Major dissociation between medial and lateral entorhinal input to dorsal hippocampus. Science 308:1792–1794

Harris KD (2005) Neural signatures of cell assembly organization. Nat Rev Neurosci 6:399-407.

Harris KD, Henze DA, Csicsvari J, Hirase H, Buzsáki G (2000) Accuracy of tetrode spike separation as determined by simultaneous intracellular and extracellular measurements. J Neurophysiol 84:401–414

Hasselmo ME, Bodelón C, Wyble BP (2002) A proposed function for hippocampal theta rhythm: separate phases of encoding and retrieval enhance reversal of prior learning. Neural Comput 14:793–817

Hazan L, Zugaro M, Buzsáki G (2006) Klusters, NeuroScope, NDManager: a free software suite

for neurophysiological data processing and visualization. J Neurosci Methods 155:207–216

Heale VR, Vanderwolf CH, Kavaliers M (1994)Components of weasel and fox odors elicit fast wave bursts in the dentate gyrus of rats. Behav Brain Res63:159–165.

Hebb DO (1949) The organization of behaviour. Wiley. New York.

Henriksen EJ, Colgin LL, Barnes CA, Witter MP, Moser M-B, Moser EI (2010) Spatial representation along the proximodistal axis of CA1. Neuron 68:127–137

Hiller-Sturmhöfel S, Swartzwelder HS. Alcohol's Effects on the Adolescent Brain—What Can Be Learned From Animal Models (http://pubs.niaaa.nih.gov/publications/arh284/213-221.htm)

Hjorth-Simonsen A, Jeune B. (1972) Origin and termination of the hippocampal perforant path in the rat studied by silver impregnation. J Comp Neurol. 144:215-232.

Ho ECY, Strüber M, Bartos M, Zhang L, Skinner FK. (2012) Inhibitory networks of fast-spiking interneurons generate slow population activities due to excitatory fluctuations and network multistability. J Neurosci 32:9931-9946.

Houser CR (2007) Interneurons of the dentate gyrus: an overview of cell types, terminal fields and neurochemical identity. Prog Brain Res. 163: 217-232.

Hyvärinen A, Oja E (2000) Independent component analysis: algorithms and applications. Neural Netw 13:411–430

Hyvärinen, A, Karhunen, J and Oja, E (2004) Independent Component Analysis. John Wiley & Sons, New York, NY

Ibarz JM, Foffani G, Cid E, Inostroza M, Menendez de la Prida L. (2010) Emergent dynamics of fast ripples in the epileptic hippocampus. J Neuroscience 30:16249-16261.

Igarashi KM, Lu L, Colgin LL, Moser M-B, Moser EI (2014) Coordination of entorhinal-hippocampal ensemble activity during associative learning. Nature 510:143-147

Ishizuka N, Weber J, Amaral DG. 1990. Organization of intrahippocampal projections originating from CA3 pyramidal cells in the rat. J Comp Neurol. 295:580-623.

Isomura Y, Sirota A, Ozen S, Montgomery S, Mizuseki K, Henze DA, Buzsáki G (2006) Integration and segregation of activity in entorhinal-hippocampal subregions by neocortical slow oscillations. Neuron, 52:871–82.

Jarsky T, Roxin A, Kath WL, Spruston N (2005) Conditional dendritic spike propagation following distal synaptic activation of hippocampal CA1 pyramidal neurons. Nat Neurosci 8:1667–1676

Jenkins GM, Watts DG (1968) Spectral analysis and its applications. Holden-Day, San Francisco.

Kadir SN, Goodman DFM, Harris KD (2014). High-dimensional cluster analysis with the masked EM algorithm. Neural Computation 26:11

Kamondi A, Acsády L, Wang XJ, Buzsáki G (1998) Theta oscillations in somata and dendrites of hippocampal pyramidal cells in vivo: activity-dependent phase-precession of action potentials. Hippocampus 8:244-261.

Katzner S, Nauhaus I, Benucci A, Bonin V, Ringach D L, Carandini M. (2009). Local origin of field potentials in visual cortex. Neuron 61, 35-41.

Klausberger T, Somogyi P (2008) Neuronal diversity and temporal dynamics: the unity of hippocampal circuit operations. Science 321:53-57.

Kocsis B, Bragin A, Buzsáki G (1999). Interdependence of Multiple Theta Generators in the Hippocampus: a Partial Coherence Analysis. J. Neurosci. 19, 6200-6212.

Kuki T, Ohshiro T, Ito S, Ji ZG, Fukazawa Y, Matsuzaka Y, Yawo H, Mushiake H. (2012). Frequency-dependent entrainment of neocortical slow oscillation to repeated optogenetic stimulation in the anesthetized rat. Neurosci Res 75:35-45.

Lachaux JP, Rodriguez E, Martinerie J, Varela FJ (1999) Measuring phase synchrony in brain signals. Hum Brain Mapp 8:194–208

Lasztóczi B, Klausberger T (2014) Layer-Specific GABAergic Control of Distinct Gamma Oscillations in the CA1 Hippocampus. Neuron 81:1126–1139.

Le Van Quyen M, Foucher J, Lachaux J, Rodriguez E, Lutz A, Martinerie J, Varela FJ (2001) Comparison of Hilbert transform and wavelet methods for the analysis of neuronal synchrony. J Neurosci Methods 111:83–98

Leão RN, Mikulovic S, Leão KE, Munguba H, Gezelius H, Enjin A, Patra K, Eriksson A, Loew LM, Tort ABL, Kullander K (2012) OLM interneurons differentially modulate CA3 and entorhinal inputs to hippocampal CA1 neurons. Nat Neurosci15:1524–1530.

Łęski S, Lindén H, Tetzlaff T, Pettersen KH, Einevoll GT (2013) Frequency dependence of signal power and spatial reach of the local field potential. PLoS Comput Biol 9:e1003137

Leung LS (1979) Potentials evoked by alvear tract in hippocampal CA 1 region in rats. II. Spatial field analysis. J Neurophysiol. 42:1571-1589.

Leung LS (1984) Model of gradual phase shift of theta rhythm in the rat. J Neurophysiol 52:1051–1065

Leung LS (1998) Generation of theta and gamma rhythms in the hippocampus. Neuroscience and biobehavioral reviews 22:275–290

Leung LS, L Roth L, Canning KJ (1995) Entorhinal inputs to hippocampal CA1 and dentate gyrus in the rat: a current-source-density study. J Neurophysiol 73:2392-2403

Leung L-WS (1991) Field Potentials in the Central Nervous System. Neuromethods 15:277–312

Lever C, Burton S, Jeewajee A, Wills TJ, Cacucci F, Burgess N, O'Keefe J (2010) Environmental novelty elicits a later theta phase of firing in CA1 but not subiculum. Hippocampus 20:229–234.

Li XG, Somogyi P, Ylinen A, Buzsáki G (1994) The hippocampal CA3 network: an in vivo intracellular labeling study. J Comp Neurol 339:181-208.

Lindén H, Tetzlaff T, Potjans T C, Pettersen K H, Gru S, Diesmann M, Einevoll G. (2011). Modeling the spatial reach of the LFP. Neuron, 859-872.

Lisman JE, Idiart MA (1995) Storage of 7 +/- 2 short-term memories in oscillatory subcycles. Science 267:1512-1515.

Lisman JE, Jensen O (2013) The theta-gamma neural code. Neuron 77:1002–1016.

Logothetis NK, Kayser C, Oeltermann A (2007) In vivo measurement of cortical impedance spectrum in monkeys: implications for signal propagation. Neuron 55:809–823

Lorente de Nó R. 1934. Studies on the structure of the cerebral cortex. II. Continuation of the study of the ammonic system. J Psychol Neurol. 46:113-177.

Lorente de Nó R. 1947. Analysis of the distribution of action currents of nerves in volume conductors. In: A Study of Nerve Physiology, New York: The Rockefeller Institute, part2. vol. 132, p. 384–477.

Malmivuo J, Plonsey R (1995) Bioelectromagnetism: principles and applications of bioelectric and biomagnetic fields. Oxford University Press. New York.

Mann, E.O., Paulsen, O. (2007). Role of GABAergic inhibition in hippocampal network oscillations. Trends Neurosci. 30, 343-349.

Marder E, Bucher D (2007) Understanding circuit dynamics using the stomatogastric nervous system of lobsters and crabs. Annu Rev Physiol 69:291–316

Mitra PP, Pesaran B (1999) Analysis of dynamic brain imaging data. Biophys J. 76:691-708

Mitzdorf U (1985) Current source-density method and application in cat cerebral cortex: investigation of evoked potentials and EEG phenomena. Physiol Rev 65:37–100.

Mizuseki K, Buzsáki G (2013) Preconfigured, skewed distribution of firing rates in the hippocampus and entorhinal cortex. Cell Rep 4:1010–1021

Mizuseki K, Diba K, Pastalkova E, Buzsáki G (2011) Hippocampal CA1 pyramidal cells form functionally distinct sublayers. Nat Neurosci 14:1174–1181.

Mizuseki K, Diba K, Pastalkova E, Teeters J, Sirota A, Buzsáki G (2014) Neurosharing: large-scale data sets (spike, LFP) recorded from the hippocampal-entorhinal system in behaving rats. F1000Research 3

Mizuseki K, Royer S, Diba K, Buzsáki G (2012) Activity dynamics and behavioral correlates of CA3 and CA1 hippocampal pyramidal neurons. Hippocampus 22:1659-1680.

Mizuseki K, Sirota A, Pastalkova E, Buzsáki G (2009) Theta Oscillations Provide Temporal Windows for Local Circuit Computation in the Entorhinal-Hippocampal Loop.Neuron 64:267-280.

Montgomery SM, Buzsàki G (2007) Gamma oscillations dynamically couple hippocampal CA3 and CA1 regions during memory task performance. Proc Natl Acad Sci USA 104:14495–14500.

Montgomery SM, Sirota A, Buzsáki G (2008) Theta and gamma coordination of hippocampal networks during waking and rapid eye movement sleep. J Neurosci 28:6731-6741.

Montgomery SM, Betancur MI, Buzsáki G (2009) Behavior-dependent coordination of multiple theta dipoles in the hippocampus. J Neurosci 29:1381-1394.

Mori M, Abegg MH, Gähwiler BH, Gerber U (2004) A frequency-dependent switch from inhibition to excitation in a hippocampal unitary circuit. Nature431:453–6.

Neunuebel JP, Knierim JJ (2014) CA3 retrieves coherent representations from degraded input: direct evidence for CA3 pattern completion and dentate gyrus pattern separation. Neuron, 81:416–27.

Newman EL, Gillet SN, Climer JR, Hasselmo ME (2013) Cholinergic blockade reduces theta-gamma phase amplitude coupling and speed modulation of theta frequency consistent with behavioral effects on encoding. J Neurosci 33: 19635-19646.

Nicholson C, Freeman JA (1975) Theory of current source-density analysis and determination of conductivity tensor for anuran cerebellum. J Neurophysiol 38:356–368

Nunez PL, Srinivasan R (2006) Electric Fields of the Brain: The Neurophysics of EEG. 2nd edition. New York: Oxford University Press. New York.

O'Keefe J, Recce ML (1993) Phase relationship between hippocampal place units and the EEG theta rhythm. Hippocampus 3:317-330.

O'Keefe J, Nadel L (1978) The Hippocampus as a Cognitive Map. Clarendon Press

Oppenheim AV, Schafer RW (1989) Discrete-time signal processing. Prentice Hall, Englewood Cliffs. New Yersey.

Pastalkova E, Itskov V, Amarasingham A, Buzsáki G (2008) Internally generated cell assembly sequences in the rat hippocampus. Science 321:1322–1327

Patel J, Fujisawa S, Berényi A, Royer S, Buzsáki G (2012) Traveling Theta Waves along the Entire Septotemporal Axis of the Hippocampus. Neuron 75:410–417

Pauluis Q, Baker SN, Olivier E. (1999) Emergent oscillations in a realistic network: the role of inhibition and the effect of the spatiotemporal distribution of the input. J Comput Neurosci. 6:27-48.

Penttonen, M, Buzsáki, G. (2003). Natural logarithmic relationship between brain oscillators. Thalamus Relat. Syst. 2:145–152.

Pernía-Andrade AJ, Jonas P (2014) Theta-gamma-modulated synaptic currents in hippocampal granule cells in vivo define a mechanism for network oscillations. Neuron 81:140–52

Pittman-Polletta BR, Kocsis B, Vijayan S, Whittington MA, Kopell NJ (2015) Brain Rhythms Connect Impaired Inhibition to Altered Cognition in Schizophrenia. Biol Pychiatry 77:997-1116

Plonsey R, Heppner DB (1967) Considerations of quasi-stationarity in electrophysiological systems. Bull Math Biophys 29:657–664

Poe GR, Nitz DA, McNaughton BL, Barnes CA (2000) Experience-dependent phase-reversal of hippocampal neuron firing during REM sleep. Brain Res 855:176–180.

Pouille F, Scanziani M (2001) Enforcement of temporal fidelity in pyramidal cells by somatic feed-forward inhibition. Science 293:1159–1163

Ray S, Maunsell JHR (2011) Different origins of gamma rhythm and high-gamma activity in macaque visual cortex.PLoSBiol 9:e1000610.

Reich DS, Victor JD, Knight BW, Ozaki T, Kaplan E (1997). Response variability and timing precision of neuronal spike trains in vivo. J. Neurophysiol. 77, 2836-2841.

Remondes M, Schuman EM (2002) Direct cortical input modulates plasticity and spiking in CA1 pyramidal neurons. Nature 416:736–740.

Rivas J, Gaztelu JM, García-Austt E (1996). Changes in hippocampal cell discharge patterns and theta rhythm spectral properties as a function of walking velocity in the guinea pig. Exp. Brain Res. 108, 113-118.

Rossant C, Kadir SN, Goodman DFM, Schulman J, Belluscio M, Buzsáki G, Harris KD (2015) Spike sorting for large, dense electrode arrays. bioRxiv doi: http://dx.doi.org/10.1101/015198

Sadiku MNO. (2001). Numerical Techniques in Electromagnetics. CRC Press. New York.

Salvador R, Silva S, Basser, PJ, Miranda PC. (2011) Determining which mechanisms lead to activation in the motor cortex: a modeling study of transcranial magnetic stimulation using realistic stimulus waveforms and sulcal geometry. ClinNeurophysiol 122:748-758.

Scheffer-Teixeira R, Belchior H, Leão RN, Ribeiro S, Tort ABL (2013) On high-frequency field oscillations (>100 Hz) and the spectral leakage of spiking activity. J Neurosci 33:1535–1539

Schmidt R, Diba K, Leibold C, Schmitz D, Buzsáki G, Kempter R (2009). Single-trial phase precession in the hippocampus. J. Neurosci. 29:13232-13241.

Schomburg EW, Anastassiou CA, Buzsáki G, Koch C (2012) The spiking component of oscillatory extracellular potentials in the rat hippocampus. J Neurosci 32:11798–11811.

Schroeder CE, Lakatos P (2009) Low-frequency neuronal oscillations as instruments of sensory selection. TINS. 32:9-18.

Schroeder, C.E., Mehta, A.D., and Givre, S.J. (1998). A spatiotemporal profile of visual system activation revealed by current source density analysis in the awake macaque. Cereb. Cortex.8, 575-592.

Singer, W., and Gray, C.M. (1995) Visual feature integration and the temporal correlation hypothesis. Annu. Rev. Neurosci.18, 555-586.

Sirota A, Montgomery S, Fujisawa S, Isomura Y, Zugaro M, Buzsáki G (2008) Entrainment of Neocortical Neurons and Gamma Oscillations by the Hippocampal Theta Rhythm. Neuron 60:683-697.

Skaggs WE, McNaughton BL, Wilson MA, Barnes CA.(1996) Theta phase precession in hippocampal neuronal populations and the compression of temporal sequences. Hippocampus 6:149-72.

Soltesz I, Deschénes M (1993) Low- and high-frequency membrane potential oscillations during theta activity in CA1 and CA3 pyramidal neurons of the rat hippocampus under ketamine-xylazine anesthesia. J Neurophysiol 70:97-116.

Somogyi P, Klausberger T Neuronal Diversity and Temporal Dynamics: The Unity of Hippocampal Circuit Operations (2008) Science 5885: 53-57

Srinivasan R, Willian RW, Nunez PL (2006). Source analysis of EEG oscillations using high-resolution EEG and MEG. Prog. Brain Res. 159, 29-42.

Stark E, Roux L, Eichler R, Senzai Y, Royer S, Buzsáki G. (2014) Pyramidal cell-interneuron interactions underlie hippocampal ripple oscillations. Neuron. 83:467-8

Steward, O. (1976) Topographic organization of the projections from the entorhinal area to the hippocampal formation of the rat J. Comp. Neurol., 167:285-314.

Stewart M, Quirk GJ, Barry M, Fox SE (1992) Firing relations of medial entorhinal neurons to the hippocampal theta rhythm in urethane anesthetized and walking rats. Exp Brain Res 90:21–28

Stuart G, Spruston N, Sakmann B, Häusser M (1997) Action potential initiation and backpropagation in neurons of the mammalian CNS. Trends Neurosci 20:125–131

Sullivan D, Csicsvari J, Mizuseki K, Montgomery S, Diba K, Buzsáki G (2011). Relationships between Hippocampal Sharp Waves, Ripples, and Fast Gamma Oscillation: Influence of Dentate and Entorhinal Cortical Activity. J Neruosci 31:8605–16.

Takahashi H, Magee JC (2009) Pathway interactions and synaptic plasticity in the dendritic tuft regions of CA1 pyramidal neurons. Neuron 62:102–111.

Thielscher A, Opitz A, Windhoff M (2011) Impact of the gyral geometry on the electric field induced by transcranial magnetic stimulation. Neuroimage 54:234-243.

Thielscher A, Opitz A, Windhoff M (2011) Impact of the gyral geometry on the electric field induced by transcranial magnetic stimulation. Neuroimage 54:234-243.

Tononi, G., Edelman, G.M., and Sporns, O. (1998). Complexity and coherency: integrating information in the brain. Trends Cogn. Sci. 2, 474–484.

Torrence C, Compo G (1998) A practical guide to wavelet analysis. B Am Meteorol Soc 79:61–78.

Tort ABL , Komorowski R, Eichenbaum H, Kopell N. (2010) Measuring Phase-Amplitude Coupling Between Neuronal Oscillations of Different Frequencies. J Neurophysiol 2, 1195-1210

Tort ABL, Komorowski RW, Manns JR, Kopell NJ, Eichenbaum H (2009) Theta-gamma coupling increases during the learning of item-context associations. Proc Natl Acad Sci USA 106:20942–20947

Tort ABL, Kramer MA, Thorn C, Gibson DJ, Kubota Y, Graybiel AM, Kopell NJ (2008) Dynamic cross-frequency couplings of local field potential oscillations in rat striatum and hippocampus during performance of a T-maze task. Proc Natl Acad Sci USA 105:20517–20522

Uhlhaas, P.J., and Singer, W. (2006). Neural synchrony in brain disorders: relevance for cognitive dysfunctions and pathophysiology. Neuron 52, 155–168.

Vaidya SP, Johnston D (2013) Temporal synchrony and gamma-to-theta power conversion in the dendrites of CA1 pyramidal neurons. Nat Neurosci 16:1812-1820.

Vandecasteele M, M S, Royer S, Belluscio M, Berényi A, Diba K, Fujisawa S, Grosmark A, Mao D, Mizuseki K, Patel J, Stark E, Sullivan D, Watson B, Buzsáki G (2012) Large-scale recording of neurons by movable silicon probes in behaving rodents. J Vis Exp:e3568

Vanderwolf CH (1969) Hippocampal electrical activity and voluntary movement in the rat. Electroencephalogr Clin Neurophysiol 26:407–418

Vanderwolf CH (1988) Cerebral activity and behavior: control by central cholinergic and serotonergic systems. Int Rev Neurobiol 30:225-340.

vanStrien NM, Cappaert NLM, Witter MP. (2009) The anatomy of memory an interactive overview of the parahippocampal-hippocampal network. Nat rev Neurosci 10, 272:282.

Varela, F, Lachaux, JP, Rodriguez, E, Martinerie, J. (2001). The brainweb: phase synchronization and large-scale integration. Nat. Rev. Neurosci. 2, 229–239.

Varga C, Golshani P, Soltesz I (2012) Frequency-invariant temporal ordering of interneuronal discharges during hippocampal oscillations in awake mice. Proc Natl Acad Sci USA 109:E2726–34

Vertes RP, Hoover WB, Szigeti-Buck K, Leranth C (2007) Nucleus reuniens of the midline thalamus: link between the medial prefrontal cortex and the hippocampus. Brain Res Bull 71:601–609

Vinogradova OS (2001) Hippocampus as Comparator: Role of the Two Input and Two Output Systems of the Hippocampus in Selection and Registration of Information. Hippocampus 11:278-598.

Whishaw IQ, Vanderwolf CH (1973) Hippocampal EEG and behavior: changes in amplitude and frequency of RSA (theta rhythm) associated with spontaneous and learned movement patterns in rats and cats. Behav Biol 8:461-484.

Whittington MA, Traub RD, Jefferys JGR (1995) Synchronized oscillations in interneuron networks driven by metabotropic glutamate receptor activation. Nature 373:612-615.

Wilson MA, McNaughton BL (1994) Reactivation of hippocampal ensemble memories during sleep. Science 265:676–679

Witter MP, Groenewegen HJ, Lopes da Silva FH, Lohman AH (1989) Functional organization of the extrinsic and intrinsic circuitry of the parahippocampal region. ProgNeurobiol 33:161–253

Wood ER, Dudchenko PA, Robitsek RJ, Eichenbaum H (2000) Hippocampal neurons encode information about different types of memory episodes occurring in the same location. Neuron 27:623–633

Wu K, Canning KJ, Leung LS (1998). Functional interconnections between CA3 and the dentate gyrus revealed by current source density analysis. Hippocampus. 8, 217-230.

Xing D, Yeh CI, Shapley RM (2009) Spatial spread of the local field potential and its laminar variation in visual cortex. J Neurosci 29:11540-11549

Yeckel MF, Berger TW (1990) Feedforward excitation of the hippocampus by afferents from the entorhinal cortex: redefinition of the role of the trisynaptic pathway. Proc Natl Acad Sci USA 87:5832–5836.

Ylinen A, Bragin A, Nádasdy Z, Jando G, Szabó I, Sik A, Buzsáki G (1995) Sharp wave associated high-frequency oscillation (200 Hz) in the intact hippocampus: network and intracellular mechanisms. J Neurosci 15:30–46

Zemankovics R, Veres JM, Oren I, Hájos N (2013) Feedforward inhibition underlies the propagation of cholinergically induced gamma oscillations from hippocampal CA3 to CA1. J Neurosci 33:12337–12351